MICROCOPY RESOLUTION TEST CHART

NATIONAL BUREAU OF STANDARDS 1963-A

REPORT ONR-CR212-223-5F

OFFICE OF · ONR · NAVAL RESEARCH

USN

LEVEL

(13)

SUMMARY OF THEORETICAL AND EXPERIMENTAL

INVESTIGATIONS OF VORTEX LIFT AT HIGH ANGLES OF ATTACK

Satish S. Samant
Richard P. White, Jr.
D. S. JanakiRam

RASA Division of
Systems Research Laboratories, Inc.
1055 J. Clyde Morris Boulevard
Newport News, Virginia   23602

D D C

OCT 1 1979

RECEIVED

A

Final Report for the Period 1 January 1974 - 31 March 1979

Prepared for the

OFFICE OF NAVAL RESEARCH●800 N. QUINCY ST.●ARLINGTON●VA●22217
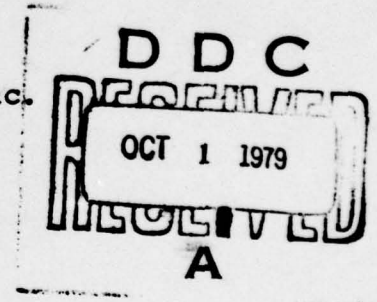
79 10 01 035

SUMMARY OF THEORETICAL AND EXPERIMENTAL

INVESTIGATIONS OF VORTEX LIFT AT HIGH ANGLES OF ATTACK

Satish S. Samant
Richard P. White, Jr.
D. S. JanakiRam

RASA Division of
Systems Research Laboratories, Inc.
1055 J. Clyde Morris Boulevard
Newport News, Virginia   23602

Final Report for the Period 1 January 1974 - 31 March 1979

Approved for public release; distribution unlimited.

Prepared for the

OFFICE OF NAVAL RESEARCH●800 N. QUINCY ST.●ARLINGTON●VA●22217

Change of Address

Organizations receiving reports on the initial distribution list should confirm correct address. This list is located at the end of the report. Any change of address or distribution should be conveyed to the Office of Naval Research, Code 211, Arlington, Virginia 22217.

Disposition

When this report is no longer needed, it may be transmitted to other organizations. Do not return it to the originator or the monitoring office.

Disclaimer

The findings and conclusions contained in this report are not to be construed as an official Department of Defense or Military Department position unless so designated by other official documents.

Reproduction

Reproduction in whole or in part is permitted for any purpose of the United States Government.

REPORT DOCUMENTATION PAGE	READ INSTRUCTIONS BEFORE COMPLETING FORM

1. REPORT NUMBER	2. GOVT ACCESSION NO.	3. RECIPIENT'S CATALOG NUMBER
ONR-CR-212-223-5F		

4. TITLE (and Subtitle)	5. TYPE OF REPORT & PERIOD COVERED
SUMMARY OF THEORETICAL AND EXPERIMENTAL INVESTIGATIONS OF VORTEX LIFT AT HIGH ANGLES OF ATTACK.	Final Report. 1 Jan 74 — 31 Mar 79
	6. PERFORMING ORG. REPORT NUMBER
	RASA/SRL-14-79-03

7. AUTHOR(s)	8. CONTRACT OR GRANT NUMBER(s)
D. S. JanakiRam Satish S. Samant Richard P. White, Jr.	N00014-74-C-0091

9. PERFORMING ORGANIZATION NAME AND ADDRESS	10. PROGRAM ELEMENT, PROJECT, TASK AREA & WORK UNIT NUMBERS
RASA Division of Systems Research Laboratories, Inc. 1055 J. Clyde Morris Boulevard Newport News, Virginia 23602	166p.

11. CONTROLLING OFFICE NAME AND ADDRESS	12. REPORT DATE
Department of the Navy Office of Naval Research Vehicle Technology Program (Code 211) Arlington, Virginia 22217	May 1979
	13. NUMBER OF PAGES
	162

14. MONITORING AGENCY NAME & ADDRESS(If different from Controlling Office)	15. SECURITY CLASS. (of this report)
	Unclassified
	15a. DECLASSIFICATION/DOWNGRADING SCHEDULE -----

16. DISTRIBUTION STATEMENT (of this Report)

Approved for public release; distribution unlimited.

17. DISTRIBUTION STATEMENT (of the abstract entered in Block 20, if different from Report)

18. SUPPLEMENTARY NOTES

19. KEY WORDS (Continue on reverse side if necessary and identify by block number)

vortex lift
vortex flow
stall flow

wing-vortex interactions
leading edge vortex generators

20. ABSTRACT (Continue on reverse side if necessary and identify by block number)

This Summary Report presents the development and verification of a theoretical prediction method for predicting aerodynamic characteristics of low aspect ratio and delta wings at high angles of attack. A summary of the experimental measurements made on low aspect ratio swept wings with leading edge vortex devices is presented as well as a discussion of the final computer program that was developed and correlated with experimental data obtianed on swept and delta wings during the last year of the contract effort.

DD FORM 1473 EDITION OF 1 NOV 65 IS OBSOLETE
1 JAN 73

409 781

SUMMARY

An experimental and theoretical research program
was conducted to evaluate the performance benefits obtained
from the vortex flows generated in the pressure field of a
low aspect ratio wing. Wind tunnel studies were conducted
with an unmodified wing panel and with strakes, snags, sep-
arator plates and combinations thereof attached to the panel.
Additional tests were conducted to determine the effect of
the main wing wake on the effectiveness of a horizontal tail
surface. The results of the test program showed that the
performance characteristics of the unmodified wing panel can
be improved substantially in the post-stall region with the
addition of leading edge devices such as strakes. The re-
sults of the tests with tail surface indicated that while
the vortex flows developed large pitching moments on the
wing, the horizontal tail surface placed properly in the
wake was able to counter the pitching moment and trim the
configuration.

Concurrently, a theoretical analysis was developed
based on a modified potential lifting surface theory and a
self-similar solution of the Navier-Stokes equations to pre-
dict the lift and pressures on the wing surface. The theory
included proper accounting of the potential and separated
flows on the wing and the suction forces of the leading edge
vortices. A good correlation was obtained between the exper-
imental and the predicted results for Navy's F-4 type wing
and a reasonable correlation was obtained for sharp edged
delta wings.

3

FOREWORD

The work described in the technical report was per-
formed by the RASA Division of Systems Research Laboratories,
Inc., for the Department of the Navy, Office of Naval Research,
Arlington, Virginia, under Contract Number N00014-74-C-0091.
The research program was undertaken under the technical cog-
nizance of Dr. Robert E. Whitehead of the Vehicle Technology
Program of ONR.

4

TABLE OF CONTENTS

LIST OF FIGURES

7

9

LIST OF SYMBOLS

a_{ij}	velocity influence coefficient, Eq. 8
A	constant in Eq. 1
b	wing span
b_{ij}	velocity influence coefficient, Eq. 8
c	chord, Fig. 2
c_{ij}	velocity influence coefficient, Eq. 8
C_D	drag coefficient
C_L	lift coefficient
C_M	moment coefficient
C_P	pressure coefficient on the wing
C_R, C_u, C_w	constants in Eqs. 12 and 13
d	distance of a point on the wing from the centerline of the vortex
d'	d/r_c
d_j	the discretized doublet strength on panel j
$\dfrac{dC_m}{d\alpha_t}$	the slope of $C_M - \alpha_t$ curve
$D(\overline{r})$	doublet strength distribution
F	function in Eq. 12
h	distance used in Eq. 1

10

H	distance between the wing and tail Macs in vertical direction
K_1, K_2, K_3, K_4, K_5	constants used in Eq. 12
L	distance between the wing and tail MACs in horizontal direction
M_1, M_2, M_3, M_4, M_5	constants used in Eq. 13
N_A	number of panels on the wing in the attached region
$\bar{q}$	total velocity vector
$\bar{q}_a$	axial velocity vector
$\bar{q}_d, \bar{q}_{d_i}$	induced velocity due to the doublets
$\bar{q}_v, \bar{q}_{v_i}$	induced velocity due to vortices
$\bar{r}, \bar{r}_p, \bar{r}_1$	position vectors
$\bar{R}$	$(\bar{r} - \bar{r}_p)$ where p is the point at which the effect of doublets is computed in Eq. 3
R_n	Reynolds number
r_c	core radius
s	the distance along the core centerline
s_o	the parameter used in Eq. 13
$\bar{U}_o, U_o$	the free stream velocity
$\bar{U}_{max}$	velocity in Eq. 12
V_a	axial velocity in the core of the vortex

11

V_ϕ	tangential velocity in the core of the vortex
$w_n, w_{n_i}, w_{n_{v_i}}$	normal velocity components
W_{max}	velocity in Eq. 12
x, y, z	coordinates in Fig. 42
$\bar{y}, \bar{y}'$	coordinates used in Eq. 1 and Fig. 1
y_o	parameter used in Eq. 13
z_o	parameter used in Eq. 13
α	viscosity parameter, Eq. 12
α_o, α_w	wing angle of attack
α_s	stall angle used in Eq. 10
$\alpha_{t_{trim}}$	tail angle of attack at trim
ΔC_D	incremental drag coefficient
ΔH_i	loss of total pressure
$\Delta C_L, \Delta C_{L_v}$	incremental lift coefficient
ΔC_p	difference of pressure coefficient on upper and lower surface
Γ	circulation strength of the vortex
ν_t	turbulent eddy viscosity
ν	kinematic viscosity
σ_{ij}	normal velocity influence coefficient
θ_i	geometric slope angle

12

1. INTRODUCTION

A four year research program was conducted by RASA
Division of Systems Research Laboratories, Inc., under the
sponsorship of the Office of Naval Research to study the
vortex flow interactions with the lifting surfaces and the
possibility of applying the vortex control techniques to
improve the performance and maneuvering capabilities of
present generation aircraft. The study included both the
experimental measurements of performance and pressure dis-
tributions on the lifting surface and a theoretical analy-
sis of the flow field.

The objective of the research program in the first
year was to explore the feasibility of generating a signifi-
cant incremental lift through wing/vortex interactions. A
review of experimental data previously obtained on the F-4
Phantom wing planform showed that a relatively weak snag
vortex generated within the pressure field of the wing can
produce a large beneficial suction peak and incremental
lift. Because of this noted apparent benefit, the following
investigations were undertaken during the first year of
research.

1. A review of current theoretical capabilities
in the field of vortex control and wing/vortex interactions.

2. Development of a simplified theoretical model
of the wing/vortex interaction.

3. Study of "vortex generator" characteristics.

4. Comparison of representative vortex control
configurations.

13

A detailed discussion of the results of this study were presented in Reference 1.

At the end of the first year's effort, it was concluded that the maximum amount of incremental lift obtainable from attached vortex flows could be achieved when the vortex was close to the lifting surface and when the vortices were formed within the pressure field of the wing. Therefore, in the second year, an experimental program was undertaken, in part to demonstrate and to verify that the beneficial incremental lift and wing vortex interaction mechanisms indicated by the simplified theory utilized in Reference 1 could be achieved.

The studies were conducted using an F-4 type of wing planform with and without leading edge control devices including a strake, a snag, and combinations thereof. The pressures and the total forces and moments on the wing were measured. Flow visualization studies were also carried out using the helium bubble technique. The data obtained was reduced in order to:

1. analyze the results of vortex control devices in terms of improving the total lift and drag performance of the system tested,

2. interrelate the improvements in lift and drag performance with wing/vortex interaction phenomena on the basis of the observed spanwise and chordwise pressure distributions,

3. obtain a more basic understanding of the parameters which control the positive benefits that can be achieved through the interaction of a vortex with a lifting surface,

14

4. determine the capability of the available theoretical model in relation to the observed experimental phenomena, and

5. outline the theoretical and/or experimental research requirements to further develop the understanding of the use of vortex flows to improve the performance characteristics of the aircraft.
The results of the second year's efforts and a detailed discussion of the experimental program can be found in Reference 2.

These results in general demonstrated that the most significant effect was realized by the addition of a strake at the wing root. While the strake vortex by itself did not generate a large suction lift, it strengthened and stabilized the leading edge vortex and effected a significant increase in its suction lift. The addition of an outboard snag resulted in a further beneficial change in performance. It was also concluded that the effectiveness of the root strake had reached its limit and additional vortex control must be sought after by applying devices on the outboard section of the wing. Therefore, an additional experimental program was undertaken in the third year to investigate whether the flow on the outboard section of the wing could be stabilized. In addition to that, it was believed that the beneficial effects of the vortex control techniques could be realized at lower angles of attack by generating the vortices at lower angles of attack by artificial means. It was also concluded from the experimental observations of the second year's efforts that the simplified theory of Reference 1 was totally inadequate to handle the complex flow phenomenon. Therefore,

additional efforts were made to theoretically represent the complex flow field over the lifting surface in a more comprehensive and concise manner. The results of the third year's efforts were reported in Reference 3.

The test results obtained at this stage of the research effort showed that while positive gains in lift and drag characteristics could be achieved, the pitching moments tended to become unstable with increasing angles at higher angles of attack. Therefore, an experimental investigation of the tail effectiveness, under the conditions that actually existed behind a lifting surface developing strong attached vortex flows was undertaken during the fourth year.

The results of a doublet lattice method developed during the third year to predict the nonlinear suction effects showed reasonable comparisons between the predicted and observed performance and pressure loadings. However, due to certain inherent assumptions (such as neglecting the thickness and the curvature effects) made in the analysis, the prediction capabilities of that analysis were thought to be rather limited. Therefore, the theoretical analysis was extended to include the effect of the thickness and the surface slope. Also, a better model of the nonlinear suction effects of the interacting vortices was incorporated into the analysis. The results of the efforts during the fourth year were reported in Reference 4.

In the fifth year, the computer program written for the theoretical analysis was streamlined and documented

16

so that it could be used as a research tool to analyze
certain other planforms. This final report presents a
general summary of the entire research effort and the
documentation of the computer program.

17

2. TECHNICAL DISCUSSION

2.1 PRELIMINARY INVESTIGATION OF THE BASIC MECHANISMS OF WING/VORTEX INTERACTION

It has been known, for several years, that the interaction between the wing and a vortex can produce additional lift as in the case of the vortices generated by strakes, close coupled canards, and snags. The vortices interacting with the wing can be free vortices created by an independent upstream aerodynamic device or may be formed within the pressure field of a wing surface due to loading gradients. The chordwise pressure distributions on the upper surface of a symmetric airfoil in the vicinity of a free vortex are shown in Figure 1 (Ref. 5) to illustrate the incremental suction effect from a free vortex generated by an upstream lifting surface. As shown in Figure 2 (Ref. 6), a similar incremental suction effect is also observed in the case of a snag vortex interacting with the wing surface that generated the vortex.

The wing/vortex interaction basically involves two mechanisms. The induced velocity distribution over the lifting surface produced by the vortex changes the effective angle of attack and the loading in the vicinity of the vortex. The change in the loading thus obtained is such that the loading increases on one side of the vortex axis (upwash side) and decreases on the other side (downwash side) of the vortex axis. The other effect is the nonlinear suction effect caused by the low pressure within the rotational field of the vortex. Figure 3 illustrates the qualitative nature of the vortex suction effect for a pair of counter-rotating vortices

18

on the suction side of a lifting surface. Based on simple physical principles, a theoretical model was developed in Reference 1 to predict the incremental suction peaks produced by the wing/vortex interaction. A general expression for the incremental suction pressure is given by

$$\Delta C_{p_v} = A \left(\frac{\Gamma}{U_o b}\right)^2 \left\{\frac{1}{(\overline{y}-\overline{y}')^2 + (h/b)^2} + 16 \frac{h^2}{r_c^4} e^{-2\left[(y-y')^2 + h^2/r_c^2\right]}\right\} \quad (1)$$

The quantity Γ represents the strength of the vortex and the rest of the terms are illustrated in Figure 3. The first term in Equation 1 represents the contribution of the tangential velocity associated with the vortex, whereas, the second term represents the effects of the axial velocity in the core of the vortex. This simplified expression was used to obtain good correlation with observed experimental results by selecting appropriate values of the parameters A and h/r_c. Qualitatively, the trends predicted were good but the values of A required were somewhat unrealistic.

In Reference 1, expressions were also derived for the incremental lift and drag coefficients due to the effects of line vortices interacting with a lifting surface. Using these expressions, comparisons of experimental and theoretical results were made for configurations with a strake, a close coupled canard, and a leading edge snag. These comparisons are shown in Figures 4 through 6 respectively. As can be seen from the comparisons, the simplified theory generally predicted the overall change caused by the vortex interactions.

Additional comparisons were also made in Reference 1 to assess the effectiveness of the different high lift devices.

These comparisons are presented in Figures 7 through 9. The results indicated that at low angles of attack, the snag was probably the most effective device, whereas, at high angles of attack, the attached strake would probably be the most effective device in improving the high angle of attack maneuvering capabilities.

The general conclusions that were drawn from the preliminary efforts summarized above from Reference 1 were:

a. The interaction of a wing with free vortices, generated by strakes or close coupled canards, gives rise to beneficial lift and generates some drag increase at low lift coefficients but lower drag coefficients at high lift coefficients.

b. The interaction of the wing with the vortex generated within the pressure field of the wing, such as those generated by leading edge vortex generators (e.g., snags and strakes), gives rise to a relatively weak vortex and a beneficial incremental lift through an enhanced suction field much greater than that produced by a free vortex of the same strength interacting with a lifting surface. In addition, the incremental drag generated by the leading edge vortices seems to be favorable throughout the range of angles of attack of interest to a maneuverable operating aircraft. On the basis of these tentative conclusions arrived at through the use of a simplified theory, an experimental program was undertaken to determine if, in fact, the noted benefits could be realized.

20

2.2 EXPERIMENTAL INVESTIGATION

Based on the initial theoretical investigation, a series of experimental investigations were undertaken, to demonstrate and verify that the beneficial incremental lift can be obtained from a controlled vortex generated by and interacting with a lifting surface, to determine the mechanism by which the favorable performance gains were achieved, and to evaluate the effects of the trailed wake on the effectiveness of a horizontal tail plane. Studies were conducted on an F-4 type of wing planform with and without leading edge vortex control devices which included a strake, a snag, a separator plate, and combinations thereof. The total forces, moments, and detailed pressure distribution on the lifting surface were measured and flow visualization was carried out using tufts and the helium bubble technique.

A systematic series of tests on a basic wing planform with and without attached leading edge devices such as the strakes, the snags, and separator plates were undertaken to investigate the effects of attached vortices on the aerodynamic characteristics of the lifting surface. The basic wing model was a 1/4 scaled version of an F-4 type wing with a NACA 0006 airfoil section. The additional leading edge devices were made of flat beveled edge metal plates and could be placed at various locations on the leading edge of the basic wing. The line drawing presented in Figure 10 illustrates the manner in which various configurations were obtained by adding appendages to the basic lifting surface. The basic wing is shown by solid lines and the strake and the snag are shown by dotted lines. Many other configurations were formulated and tested by this procedure but will not be summarized in this report.

21

Complete details on these additional configurations can be found in References 2 and 3.

The instrumentation used to record the data during these tests consisted of a yoke type balance located beneath the floor to measure the three force and the three moment components. The balance measurements were monitored on-line prior to offline computer processing into the appropriate non-dimensional components. The reference axes for these measurements are shown in Figure 11.

Pressure measurements were made at 220 tap locations on the wing surface using five 48 port scanivalves, each scanivalve monitoring the tunnel total, static, and tunnel centerline pressures. The pressure data was directly punched on cards and later converted into pressure coefficients. Pressure and force measurements were obtained at both positive and negative angles of attack.

Flow visualization in the vicinity of the wing was provided by neutrally buoyant helium bubbles. The bubbles were illuminated by a collimated beam of light and were observed and photographed. Flow visualization was also obtained using tufts located at the pressure tap locations over the surface.

The majority of the tests were conducted at tunnel speeds of 100 and 150 ft/sec over an angle of attack range of zero to approximately thirty (30) degrees.

Since the primary purpose of the wind tunnel tests was to determine if the "vortex lift" could have a significant effect on the performance characteristics of a low aspect ratio, swept lifting surface at high angles of attack, the pressure distributions and flow visualization over the wing were the

22

primary tools used to evaluate the manner in which the attached vortex flows had altered the performance characteristics of the lifting surface as measured by the balance system.

Detailed discussion of the results obtained during these tests is presented in References 2 and 3. Only the major results that were obtained will be discussed herein, with the help of representative data. A majority of the characteristics of the interaction of the wing and vortex can be illustrated by the discussion of the results obtained for the following three configurations:

    a. Basic wing

    b. Basic wing with strake

    c. Basic wing with a strake and a snag

The variations of the lift coefficient, the drag coefficient and the pitching moment coefficient with angle of attack for the above configurations are presented in Figures 12, 13 and 14, respectively. These figures indicate that the performance characteristics of all three configurations are approximately the same below an angle of attack of about 13°. Beyond this angle, the basic wing shows a soft stall, with a maximum lift coefficient of about 1. The addition of a strake alters the lift curve considerably above 13° angle of attack. The lift coefficient continues to increase with angle of attack, at approximately the same rate as the one below 13°, up to an angle of attack of 28° and then stalls abruptly. At an angle of attack of 28°, the strake configuration has a lift coefficient 1.45 times the maximum value measured for the basic wing. This increase in lifting capability is due to the strong interaction between the strake and the leading edge vortices.

The addition of the snag to the wing strake combination had a beneficial effect in the high angle of attack range in

23

that it increased the lift at a given angle of attack and yielded a maximum lift coefficient of about 1.6 times that of the basic wing and 1.1 times that for the basic wing with a root strake.

The effect of the strake and snag on the drag characteristics of the lifting surface are shown in Figure 13. The drag for those configurations was greater than for the basic wing, but was not greater to the degree that would be expected based on the quadratic variation of the induced drag with lift.

The pitching moment coefficients about quarter chord station of the mean aerodynamic chord (MAC) are shown in Figure 14. As can be seen, the vortex generating surfaces have a pronounced effect on the pitching moments. For the basic wing, the nose down (negative) pitching moment, increases somewhat linearly with the angle of attack until the angle of attack at which leading edge separation occurs and the attendant leading edge vortex forms. At that point, the pitching moment increases much less rapidly with angle of attack. The rate of increase of the pitching moment, however, becomes larger until it reaches approximately the same value as obtained before the initiation of the leading edge separation. The break in the pitching moment slope is due to the formation of the leading edge vortex. As the angle of attack is increased further, the effect of the vortex diminishes due to separation from the wing surface and completely disappears at an angle of attack of approximately 22°.

With the strake and the strake and snag added to the basic wing, the trend of the pitching moment with angle of attack is approximately the same below an angle of attack of

24

13° as that of the basic wing. Above 13°, however, the trend
of the pitching moment with increasing angle of attack is
opposite to that of the basic wing. The reason for this
change is that when the leading edge vortex is formed, its
interaction with strake vortex causes it to be strengthened
and stabilized and then it continues to grow in strength as
the angle of attack is increased. Since the leading edge vor-
tex is formed over the inner half of the span, ahead of the
quarter chord point of the MAC, it creates a strong nose up
moment and dominates the pitching moment. For example, at 30°
angle of attack, the data indicates that the pitching moment
generated by the leading edge vortex is 1.5 times greater than
that generated by the entire lifting surface. With the snag
added, the leading edge vortex moves slightly aft and the ef-
fect is comparatively less pronounced than that of the strake
wing configuration.

Even though the pitching moment is destabilizing in
the post-leading edge stall regime, its maximum magnitude is
less than one third of that which was measured for the basic
wing and, therefore, was thought to be controllable with a
properly placed horizontal tail surface. The proper placement
of the horizontal tail, however, may be significantly different
for this configuration than it would be for the basic wing be-
cause of the flow field on the horizontal tail induced by the
vortex wake of the wing. It is of interest to note that since
the vortex lift dominates the pitching moment characteristics,
it might be possible to maintain a constant pitching moment at
all angles of attack in the post stall region by proper wing
planform tailoring to obtain an optimum leading edge vortex
placement.

The rolling moment characteristics were not altered sig-
nificantly because of the addition of the leading edge devices.

25

It was found that the center of drag tends to move inboard and remain stationary with angle of attack, which, it is believed, is advantageous in terms of yaw trim.

No significant changes were observed in the lift and drag characteristics when the relative angle between the strake and the basic wing was changed. However, the pitching moment characteristics, as shown in Figure 15, indicate a possibility of obtaining a high degree of pitch control without affecting the lift and drag characteristics.

The above performance characteristics and the manner in which the free vortices control the flow can be explained by the pressure distributions on the surface and flow visualization. Comparisons of pressure distributions at 13° (angle at which the flow is fully attached) and at 27.7° (angle at which maximum lift was obtained) were made.

Figure 16 presents the spanwise pressure distribution along the constant chord lines for the three configurations of interest at an angle of attack 13.1°. While the total lift generated by these configurations is almost the same at this angle of attack (Fig. 12), the pressure distributions are significantly different.

It can be shown that these differences in the pressure distributions are caused by the vortex flows that are generated by the lifting surface and the attached vortex generators.

In analyzing the effect of the attached vortex flows on the pressure distribution over the surface of the wing, both the induced and the suction effect of the vortex flows must be considered. While the induced effect is generally generated at spatial locations greater than the core diameter, the vortex

26

suction effect occurs at spatial locations associated with dimensions on the order of the vortex core diameter.

The spanwise pressure distributions presented in Figure 16 for the basic wing indicate that there is the semblance of a leading edge vortex, which, after its formation as a co-ordinated vortex along the 5% chord line, trails outward and aft and leaves the trailing edge near the wing tip. (The path of the centerline of the vortex can be traced by the peaks in the pressure distribution). The pressure distributions also indicate that a small secondary leading edge vortex is formed at the leading edge at about 75% span location. This secondary vortex, which is probably formed by the induced effect of the primary leading edge vortex as it turns in the chordwise direction, is quickly separated from the surface of the wing by the induced upwash of the primary vortex flow from the broad-ness of the peaks in the pressure distribution and the rather low value of the suction pressure of the main leading edge vortex, it is obvious that the leading edge vortex at this angle of attack is rather weak and diffuse. This conclusion is supported by the external flow visualization pictures that were taken using helium bubbles as only a slight, large diameter swirling flow, that might be associated with a leading edge vortex, was indicated in the pictures. The induced effect of the leading edge vortex, although relatively weak at this angle of attack, tended to reduce the angle of attack over the inboard sections of the lifting surface which in turn reduced the chord-wise gradient of potential lift in this region.

The pressure distribution for the strake configuration shows some overall similarities to that for the basic wing, although, there are differences in detail. The effect of the strake vortex is clearly evident near the root. The path of

27

the strake vortex is basically in the chordwise direction.
Since the magnitude of the pressure peaks associated with
the strake vortex decreases as the vortex moves downstream,
it can be concluded that the strake vortex moves away from
the wing as it moves downstream. Both of these conclusions
seem to be valid from photographs in Figure 17. These photo-
graphs are obtained from the helium bubble flow visualization
and indicate that the strake vortex goes directly across and
away from the wing surface as it moves downstream. The in-
duced effect of the strake vortex, though relatively weak,
creates spanwise loading gradients near the leading edge which
gives rise to the leading edge vortex. The induced effect of
the strengthened leading edge vortex tends to reduce the poten-
tial lift of the inboard section of the lifting surface as in
the case of the basic wing.

In addition, the upwash induced by the leading edge
vortex over the outboard section of the wing seems to separate
the flow as the surface pressures are less than they were for
the basic wing in this region. Due to the induced and suction
effect of the strake vortex and the stabilized flow over the
inboard sections of the lifting surface, the leading edge vor-
tex not only becomes slightly stronger but much more concentrated
and thus the suction peak it creates over the outboard sections
of the lifting surface, while narrower, is larger in magnitude.
It can also be seen by comparing the pressure distributions of
the wing with and without the strake, that once the leading edge
vortex of the wing strake configuration becomes a "semi-free"
vortex it is turned in the free stream direction much more rapidly
than it was for the basic wing configuration thus creating a
rather effective aerodynamic wing fence across the chord at
approximately the 80% span location.

28

The surface flow for this configuration as depicted by tufts is shown in Figure 18. The centerline of the paths of both the strake and leading edge vortices have been indicated on those photographs. As indicated by the tufts the flow in between the streamwise positions of the two vortices is in the clockwise direction indicating that potential flow and lift are being developed in this area. While there is some effect of vortex induced flow inboard of the strake vortex location, the flow is basically potential in nature over that region as well. Outboard of the leading edge vortex as it crosses the chord, however, it is noted that the flow is basically in the spanwise direction. A closer look at the tufts along the leading edge outboard of the leading edge vortex indicated that this area is stalled and the flow is separated. It is believed that the large induced effect of the leading edge vortex, which creates an upwash in this region, is responsible for the flow separation. Once the flow over the surface of the wing has been separated, the induced velocity of the leading edge vortex creates the spanwise flow in the low velocity region of the separated flow. While the pressure distributions presented for the wing with both the strake and outboard snag added is considerably different than those of the other configurations, the same total lift is obtained. The pressure peaks associated with the strake, leading edge, and snag vortex are clearly evident in the distributions that are presented in Figure 16. As can be seen, the characteristics of the strake vortex remains about the same as they were for the previous configuration and the leading edge vortex has been weakened and moved inboard due to its interaction with the rather strong snag vortex. Since the strake vortex is rather far removed from either the leading edge or snag vortex, there is little

29

evidence of interacting effects of the strake vortex with the outboard vortices. In fact, the pressure distributions for this configuration, except for the independent effects of the strake vortex are almost identical to those of the basic wing with just the snag added. On the basis of the pressure distributions obtained for the various configurations at a relatively low angle of attack, it is concluded that while the influence of the rather weak vortex flows did not alter the total lift that was generated, they did alter significantly the loading distributions.

At angles of attack much greater than the angle at which the basic wing stalls, the influence of the vortex flows on the total lift that is generated is much more significant as is shown by the pressure distributions presented in Figure 19. The pressure distributions shown for the basic wing indicate that except for a weak pressure peak due to the leading edge vortex near the wing root, the entire lifting surface is completely stalled as indicated by pressure coefficients of near unity. In contrast, the pressure distributions obtained for the wing with the strake added indicate that large pressure peaks are obtained. It can also be seen that not only the peak pressure associated with the leading edge vortex increased but the position of the vortex has moved inward. It is believed that both of these effects are due to the interaction of the two vortices and the strengthening of the leading edge vortex by the loading gradients generated by the strake vortex.

As indicated by the pressure distribution, the strake vortex has an entirely different path over the surface of the wing at 27.7 degrees than it did at 13.1 degrees angle of attack. This difference in the paths of the strake vortex can

30

be seen by comparing the visualized strake vortices in Figure 20 with those in Figure 17. While the initial rate of movement away from the surface of the strake vortex is greater at 27.7 degrees than it was at 13.1 degrees, the strong induced effect of the leading vortex moves the strake vortex back towards the surface of the wing as well as outward along the 75% chordline. As shown in Figure 21, the leading edge vortex moves out along the leading edge as well as away from the lifting surface due to the induced effect of the strake vortex until it bursts. After bursting the leading edge vortex becomes turbulent and turns in the streamwise direction. Although not shown in these pictures the strake and burst leading edge vortex could be seen to mix near the trailing edge of the lifting surface near the 70% span location as they both moved in the downstream direction.

The tuft picture visualizing the surface flow for this configuration at an angle of attack at 27.7 degrees is shown in Figure 22. The small areas of potential flow generated by the induced effect of the leading edge and strake vortex can be seen in the picture. It can also be seen that the strong induced effect of the leading edge vortex as it moves over the chord of the wing has completely stalled the tip region and generates a strong spanwise flow in the separated flow region over the mid span portion of the lifting surface between the two vortices.

The pressure distributions presented for the wing with the strake and snag added indicate that at this high angle of attack the primary effects of the snag vortex have disappeared but the effects of the strake and leading edge vortices have remained about the same as they were for the wing-strake configuration.

31

It is believed that the pressure distribution presented for the various configurations at 27.7 degrees clearly indicates the strong influence of the vortex flows on the lift that is generated by the wing. The majority of additional lift obtained from the vortices is due to the low pressures within the core of the vortices and not due to their induced effects on the lifting surface.

The above discussion essentially states that a single vortex formed within the pressure field (as for the basic wing alone) is rather unstable and ineffective in the post stall region. In the presence of another vortex (such as a strake vortex created by the root strake) there is a mutual strengthening and stabilizing that leads to large increments of lift well into the post stall region.

It was thought that the addition of an outboard strake could provide stabilization of the flow on the outboard section of the wing. A typical multi-strake configuration is shown in Figure 23.

When compared with the performance obtained for a single strake configuration, the performance of such a multi-strake configuration indicated little improvement because the two free edges of the outboard strake generated two vortices of opposite strength which essentially nullified the effects of each other. The induced effects of the outboard strake vortices tended to weaken the main leading edge vortex which is inboard of that strake. The addition of the outboard strake, however, did alter the pressure distribution though the integrated effect on the performance is small.

Since the beneficial effect of the vortices were realized at high angles of attack and could be traced to the

32

presence of the leading edge vortex, it was thought that similar benefits could be achieved at lower angles of attack by generating the leading edge vortex by premature separation using a sharp edged separator plate. A configuration using a strake and a full separator plate is shown in Figure 24. The measured performance indicated that at lower angles of attack, additional lift was obtained for the configuration shown in Figure 24, as compared to the configuration with only one strake. The additional lift, however, was accompanied by a significant increase in drag. The reason for this was that the leading edge vortex forms much further inboard and affects much larger areas of the wing and, thus, a large portion of the wing outboard was stalled due to the induced effects of the vortices.

A final configuration was tested that tended to eliminate the disadvantages of the last two configurations. This configuration is shown in Figure 25. The basic feature of this configuration is that it does not have the additional inboard free edge that characterized the single outboard strake. It did have a swept edge at the outboard end of the partial separator plate that provided the free edge that is desirable in order to form a vortex at that location. The strake vortex and the leading edge vortex formed over the partial separator plate combined together very quickly and traversed the wing as a single vortex and an additional free vortex was formed over the outboard region. With this configuration, larger lift could be achieved at higher angles of attack but with an attendant increase in drag.

The experimental research conducted so far had been concerned primarily with a 1/4-scale model similar to the F4E wing planform and with retrofit leading edge vortex control

devices attached to it. While the test results on the configuration have shown that positive performance gains can be obtained by the interaction of the wing with the vortices generated by leading edge surfaces, it was found, however, that the pitching moment tended to become unstable (nose up) at higher angles of attack. This is particularly true for configurations that utilized leading edge vortex generators. This unstable pitching moment characteristic is realized as the large incremental lift forward of the MAC obtained on the inboard sections of the swept wing is not balanced by the lift generated by the outboard sections of the wing which are aft of the pitching moment axis and only carry small amounts of vortex lift. It was believed, however, that the magnitude of the overall pitching moment was well within the control capability of a conventional tail plane operating in undisturbed air. Since the possible interaction of the vortex flow generated by the wing with the tail plane could significantly reduce the effectiveness of the horizontal tail, it was concluded that the effectiveness of the horizontal tail operating in the wake of the wing should be investigated. Because of the large effect that the vortices had on the performance characteristics of the primary lifting surface, their effect on the aerodynamic characteristics of the tail plane was investigated experimentally. A detailed discussion of the results obtained in these tests is presented in Reference 4.

A brief description of the test results and a summary of the conclusions is presented below.

The model for this experimental investigation consisted of two lifting surfaces, a basic wing panel with suitable leading edge attachments and a tail plane. Both the lifting surfaces were semi-span models similar in geometry to and approximately 1/4-scale versions of the F-4 phantom wing planform and

34

its horizontal tail. A picture of the model in the wind tunnel is shown in Figure 26.

The instrumentation used in these tests was essentially the same as used in earlier tests except that additional pressure taps were used on the tail surface to monitor the pressure.

The model incorporated provisions for mounting the tail plane at various lateral and longitudinal distances from the wing panel as well as means of remotely controlling the angle of attack of the tail surface relative to the wing about a vertical axis passing through its mean aerodynamic center.

Each configuration of the wing-tail system tested differed from the other in two parameters: (1) The longitudinal separation between the wing MAC and tail MAC (L); (2) The horizontal separation (H) between the wing mean aerodynamic chord and that of the tail. The distances, L and H, were set using the turntable mechanism on the floor of the test section. The model arrangement on the turntable for a typical configuration is shown in Figure 27. In addition, the wing itself had two basic configurations: (1) wing plus conventional snag, and (2) the wing plus snag with the root strake added.

Each configuration was represented by a five digit number followed by a letter A or B. The first digit can be either 1 or 2 where 1 refers to the basic wing with an outboard snag and 2 refers to the basic wing plus snag and a root strake. The second and third digits together give the longitudinal separation (L) in inches. The fourth and fifth digits together give the offset (H) in tenths of root chord of the tail. The letter A denotes the wing alone configuration and the letter B denotes the wing-tail configuration. A typical representation could be 1-75-06-B, which means a wing-tail configuration with an outboard snag, L = 75 inches, and H = .06 C_{R_T}.

Because of the lateral and longitudinal offset of the horizontal tail (Fig. 27), the wing would be in different locations in the wind tunnel as compared to the earlier tests. The basic aerodynamic characteristics of the various wing configurations were measured prior to conducting the tests of the wing-tail configurations.

On the basis of these preliminary tests, it was concluded that while there were some effects on the aerodynamic characteristics of the lifting surfaces due to its location in the tunnel, they were not of a magnitude to sufficiently affect the results of the test program.

The Figures 28 and 29 present the pitching moment variation with the wing angle of attack for the models without the tail. These results serve as a reference for comparison with the results obtained for the models with the tail.

To determine the effect of the wing wake on the tail effectiveness, tests were conducted for the various configurations to determine for various wing angles of attack, the pitch angle of the tail and trim, at which the pitching moment of the wing-tail configuration went to zero. In addition, the effectiveness of the tail surface in generating pitching moment about the wing MAC was also determined by varying the tail angle of attack about its trim value.

Figure 30 presents the results of the tests conducted with configuration 1-75-06B which is the basic wing configuration (without strake).

The pitching moment generated about the wing MAC by the tail surface, as its angle of attack was altered, was surprisingly linear regardless of the angle of attack of the

36

main wing. The slope of the pitching moment curve with tail angle of attack, $dC_M/d\alpha_T$, provides a measure of the effectiveness of the tail and the results presented in Figure 30 indicate that while there is some loss in tail effectiveness as the wing angle of attack is increased from 15 to 30 degrees, it is only of the order of 25%, which is much less than might be expected.

The variation of the tail angle of attack for trim (relative to the wing mean chord) with increasing wing angle of attack, shown in Figure 30, indicates that above a wing angle of attack of 20 degrees very large changes in the tail geometric angle of attack are required to maintain aircraft trim. This is explained below.

Since at lower angles of attack of the wing, the tail drag moment and the wing pitching moment tend to oppose each other, the lift developed by the tail would tend to be small. The pressure distributions presented in Figure 31 for the tail when the configuration is in trim for a wing angle of attack of 8.7 degrees, indicate that indeed the tail lift force is small.

As the angle of attack of the wing is increased, the MAC of the tail surface will, with respect to the free stream direction, be located such that its drag force will create a nose down instead of a nose up pitching moment about the wing MAC. For configuration 1-75-06B this shift occurs at a wing angle of attack of 11.3 degrees. For wing angles of attack of between 12 and 20 degrees, the pitching moment of the wing does not increase very much due to the formation of the leading edge vortex in this angle of attack range (Fig. 28). It would be anticipated therefore that the tail angle of attack to

37

maintain pitching moment trim in this angle of attack range would not have to be changed significantly.

As the wing angle of attack is increased above 20 degrees, the wing nose down pitching moment increases and the pitching moment of the tail drag force increases the pitching moment about the wing MAC further. Thus, as the angle of attack of the wing increases, the drag moment arm of the tail increases negatively and the moments generated about the wing MAC by the tail lift and drag force tend to offset each other. Since the lift force increases more rapidly than the drag force with increasing angle of attack, trim balances can be obtained but the angle of attack of the tail surface must undergo a larger change to maintain trim than when the wing angle of attack is lower.

Comparison of the tail pressure distribution presented in Figure 32 with those presented in Figure 31 shows that the tail surface is indeed, developing more lift at the higher wing angles of attack.

When the strake was added to the leading edge, configuration 2-75-06B, the pitching moment characteristics were different than the basic wing (Fig. 28) but the average tail effectiveness as a function of wing angle of attack did not change to any great degree (Fig. 33). It is noted, however, that the data presented in Figure 33 indicates that there is a noticeable variation in the tail effectiveness as a function of angle of attack. This variation seems to correlate with the radical changes in the tail geometric trim angle α_t with respect to the chordplane of the main wing. Inspection of the pressure distribution for the wing strake - tail configuration shows why there is a sufficient difference in the

38

behavior of the tail trim angle variation between the two
configurations. Figure 34 presents the pressure distribution
on the tail surface when the wing tail configuration is in
trim at 13.1 degrees. As can be noted from the pressure dis-
tribution, there is an obvious vortex interaction in the tail
surface at approximately the 70% span. It is believed that
this reversal of the pressure distribution in the tip region
is caused by the induced effect of the strake vortex crossing
the tail around 65% of its semispan.

At a wing angle of attack of 21.7 degrees, no evidence
of induced effects from a concentrated vortex could be found
in the pressure distributions over the tail. This can be
explained as follows. The strake vortex, under the influence
of the strong leading edge vortex generated by the wing, moves
farther outboard and is located outboard of the tail tip.
Therefore, the reversal of the pressure distribution near the
tip, as was found at lower angles of attack, was not present.
This is also true for wing angle of attack of 30.3 degrees
where the strake vortex is swept further outboard into the
leading edge vortex due to its strong induced effect. As the
wing angle of attack is increased above 21.7 degrees, a tail
trim angle of attack trend similar to that obtained with the
basic wing is obtained except that the maximum change in trim
angle is only 5 degrees instead of 16 degrees as it was for
configuration 1-75-06B. This much smaller tail trim angle
variation is attributed to the fact, that for the wing strake
configuration at high angles of attack, the pitching moment
developed by the tail drag and lift are working together to
counter the wing pitching moment instead of working against
each other as they were for the basic wing tail configuration.

39

The tail effectiveness data obtained for configuration 1-75-12B is presented in Figure 35. These results when compared to the data presented in Figure 30 show the effect of moving the tail chordplane higher up from the wing chordplane. It can be seen that the results are very similar for the two configurations except that for configuration 1-75-12B, there is a sharp drop in the tail effectiveness as the wing angle is increased from 25.6 degrees to 29.6 degrees. It is also noted that the accompanying change in the tail trim angle is not as large as it was for configuration 1-75-06B. It is believed that the reason the tail trim angle does not vary as much as it did for configuration 1-75-06B in this angle of attack range, is that the angle of attack at which the moment generated by the tail drag force about the wing MAC opposes the moment due to tail lift is approximately 23 degrees instead of approximately 11 degrees as it was for configuration 1-75-06B. Therefore, the tail lift force is much more effective for configuration 1-75-12B to obtain trim than it was for configuration 1-75-06B.

It is reasoned that the sharp drop in the tail effectiveness as the wing angle is increased from 26 to approximately 30 degrees is due to the induced effects of the diffused leading edge vortex that separated from the wing.

Comparison of the tail effectiveness data presented in Figure 36 for configuration 2-75-12B with that presented in Figure 33 shows the effect of doubling the distance of the tail surface from the wing chordplane for the wing-strake configuration. It can be seen that while the tail effectiveness has a slightly different trend, the trend of the tail geometric trim angle with wing angle of attack is significantly different. It is believed that this significantly different

40

trend is due to the different orientation of the wing wake with respect to the tail plane. At 21.5 degrees wing angle of attack, the small positive pitching moment generated by the wing (Fig. 29) is countered by the lift moment generated by the tail surface and therefore the lift required to be generated by the tail surface would be small. As the wing angle of attack is increased, the sudden jump in the positive pitching moment generated by the separation of the leading edge vortex makes a demand for a much greater lift from the tail surface.

The effect of moving the tail surface closer to the wing trailing edge on the tail effectiveness for the wing and wing strake configurations is shown in Figures 37 and 38, respectively. When this data is compared to that obtained for configurations 1-75-06B, it can be seen that the results and the trend of the results with the wing angle of attack are very similar.

Figures 39 and 40 present the effect of the tail on the lift of the wing strake and the basic wing configurations. It can be seen from the data presented that the effect of adding the tail did not significantly effect the total system lift of the wing strake configuration. However, since the tail lift required to obtain pitching moment trim was in a direction opposite to the wing lift for the basic wing configuration, a significant reduction in the configuration lift was obtained when the tail was added.

On the basis of the experimental research, it is generally concluded that the test data demonstrated that an aircraft configuration can be stabilized with a nominal size tail surface operating in the vortex wake of the main lifting surface.

41

In addition to the above general conclusion, the following specific conclusions were also formulated.

(1) The trim angle of the tail surface relative to the chord plane of wing varied differently with wing angle of attack for the basic wing and the basic wing with the root leading edge strake.

(2) When the concentrated strake vortex from the main wing intersected the tail plane, large angle changes of the tail were required to maintain system trim.

(3) Even though the characteristics of the wing wake were changing significantly as its angle of attack was changed in the range of $0 \leq \alpha_w \leq 30$ degrees, the tail effectiveness, $(dC_m/d\alpha_t)$, remained relatively constant.

(4) Even though the tail surface could have a geometric angle with respect to the free stream of 24 degrees, it is estimated, on the basis of the tail pressure distributions, that because of the strong induced effect of the wing wake that the aerodynamic angle of attack of the tail surface never exceeded 10 degrees at trim.

(5) On the basis of conclusions (3) and (4) it is believed that the total dynamic pressure at the leading edge of the tail surface remained relatively constant over the entire angle of attack range of the wing.

(6) Depending on the longitudinal and vertical location of the tail surface relative to the wing MAC, the drag of the tail surface can have a significant effect on the pitching moment about the wing MAC.

(7) For the basic wing configuration having a nose down pitching moment, the tail lift required for system trim tended to reduce the lift from the value developed by the wing alone. This reduction became more significant as the longitudinal distance between the wing and tail MACs was reduced.

2.3. THEORETICAL ANALYSIS

After the experimental results obtained in the second year (Ref. 2) were analyzed, it was concluded that the simplified theory formulated in Reference 1 was inadequate to describe the effect of vortex flows on the low aspect ratio lifting surfaces. It was also apparent that there was more than one free vortex above the wing and at higher angles of attack (21.6°, for example), the flow was partially stalled. The method developed in Reference 1 was based on a lifting line theory and could not account for the complex flow phenomena or the interactive effects of one vortex on another. Therefore, development of a theoretical prediction technique which could be applied to reasonably complex planforms, treat the multiple vortices and their interaction with the wing and each other adequately, treat the separated flow, and have the capability of obtaining a solution from easily obtainable input data, was undertaken.

Initially, a lifting surface theory was developed. The wing was modelled as a surface of discontinuity. The overall prediction from this analysis was found to be good, however, certain problems were encountered in the treatment of the separated flow. The details of the analysis were given in Reference 3. It was apparent that the flow on the upper surface was sometimes partially stalled, although, the flow on entire lower surface always remained attached. A surface theory based on satisfying the boundary conditions at the mean surface of the type developed in Reference 3 could not account for the attached flow on one side and separated flow on the other adequately. It was believed, therefore, that the total wetted surface of the wing (including upper and lower surfaces) must be included in the analysis if adequate prediction of the

43

aerodynamic characteristics of low aspect ratio wings with attached vortex flows was to be obtained. This three dimensional analysis of low aspect ratio, highly swept, highly tapered wing with partial separation, interacting with the free vortices will be briefly described and the program details are presented in the appendix.

Basic features of such a flow situation are schematically illustrated in Figure 41. At high angles of attack, the flow separates near the leading edge and rolls into a core of rotating fluid, thus forming a free vortex called the leading edge vortex. The flow is usually attached inboard of this vortex. Other free vortices such as a strake vortex (due to a strake upstream of the wing) and a tip vortex (due to flow around the wing tips) are also present for most configurations in addition to the leading edge vortex. The effect of these vortices on the flow over the wing can be considerable, especially on the upper surface; depending on various configuration parameters and the angle of attack. Generally, the vortices specified above induce downwash on the inboard section of the wing and upwash on the outboard section which can result in a region of separated or stalled flow over the outer wing panels. The region where separated flow may be encountered is indicated in Figure 41.

These free vortices, as was found in References 1, 2 and 3 can produce a strong negative pressure region in the upper surface of the wing. It has been assumed in the analysis that this vortex suction effect can be determined separately from the other effects on the pressure at the wing surface. The pressure at any point on the wing is, therefore, considered to be the sum of the suction pressure due to free vortices and the pressure due to other effects such as angle of attack, thickness, camber, separation, etc.

44

In the attached and separated region, therefore, following relations were taken to be valid

$$C_{P_{total}} = C_{P_{att}} + \Delta C_{P_v} \text{ for attached region}$$

and

$$C_{P_{total}} = C_{P_{sep}} + \Delta C_{P_v} \text{ for separated region}$$

(2)

where, $C_{P_{total}}$ is the total pressure coefficient,

$C_{P_{att}}$ is the pressure coefficient in the attached flow region due to all the effects except suction

ΔC_{P_v} is the incremental suction pressure coefficient, and,

$C_{P_{sep}}$ is the pressure coefficient in the separated region due to all the other effects except suction.

The task of the theoretical analysis was to predict $C_{P_{att}}$, $C_{P_{sep}}$ and ΔC_{P_v}.

Once the previously noted assumption regarding the vortex suction effect is made, the theoretical representation can be divided in a similar manner. The suction effect, ΔC_{P_v} can be calculated at points on the wing by applying the self-similar solution of the Navier-Stokes Equations. The potential pressure, $C_{P_{att}}$, is computed by solving the potential flow over the attached region. An empirical method is used to determine the separated region on the wing surface and the pressure there, $C_{P_{sep}}$, is calculated using a modified form of

45

Bernoulli's equations. The flow representations will be
discussed individually in the following sections.

2.3.1. Representation of the Attached Flow Region

The flow over the attached region is considered to
be potential. The Laplace equation, in terms of the velocity
potential, is solved with flow tangency condition at the wing
surface and zero disturbance condition at infinity. A solu-
tion to this problem can be written in terms of a doublet
density distribution over the wing surface with the doublet
axes pointing in the outward normal direction on the wing
surface. The doublets automatically satisfy the Laplace
equation and the infinity boundary condition. The strength
distribution, D, is obtained by satisfying the tangency con-
dition on the wing surface. The flow tangency condition at
the wing surface can be written as follows:

$$\nabla \left(\frac{1}{4\pi} \int_S D(\bar{r}) \frac{\hat{n}(\bar{r}) \cdot \bar{R}}{|\bar{R}|^3} dS \right) \cdot \hat{n}(\bar{r}_p) + (\bar{U}_o + \bar{q}_v) \cdot n(\bar{r}_p) = 0 \quad (3)$$

where $\bar{r}$ is the position vector of a point on the surface

$\quad\quad$ $D(\bar{r})$ is the doublet distribution density at a point
$\quad\quad\quad$ on the surface

$\quad\quad$ $\hat{n}(\bar{r})$ is the outward unit normal vector at point $\bar{r}$ on
$\quad\quad\quad$ the surface

$\quad\quad$ $\bar{r}_p$ is the position vector of the point on the surface
$\quad\quad\quad$ where the boundary condition is applied

$\quad\quad$ $\bar{R} = (\bar{r} - \bar{r}_p)$

$\quad\quad$ $\hat{n}(\bar{r}_p)$ is the normal unit vector in the outward direc-
$\quad\quad\quad$ tion at the point given by $\bar{r}_p$

$\quad\quad$ $\bar{U}_o$ is the free stream velocity vector, and

$\overline{q}_v(\overline{r}_p)$ is the externally induced velocity at the point
$\overline{r}_p$ on tne surface

The quantities used in this equation are referred to a body
fixed coordinate system as shown in Figure 42. Analytical
solutions of Equation 3 for the geometry of the wing under
consideration are impossible, therefore Equation 3 is solved
numerically. The wing is divided into a specified number of
panels over which the doublet density is assumed to be constant.
Equation 3 then can be written as

$$\sum_{j=1}^{NA} \sigma_{ij} d_j = w_{n_i} \qquad i = 1,2 \cdots N_A \qquad (4)$$

where N_A is the number of panels in the attached region of
the wing

σ_{ij} is the inward normal velocity induced by a doublet
panel j of unit density at a control point on
panel i

d_j is the value of doublet density on panel j, and

w_{n_i} is the outward normal velocity due to vortices
and free stream at the control point on panel i

Figure 42 indicates a typical semiwing and geometric
panel arrangement on the wing surface (note that these panels
lie on the wetted surface of the wing and not on the mean
surface). The centroid of a typical panel is selected as
its control point.

The computation of σ_{ij} is carried out by using the
following formula:

47

$$\sigma_{ij} = \left[- \nabla \int_{S_j} \frac{1}{4\pi} \frac{n(\bar{r}) \cdot \bar{R}}{|\bar{R}|^3} \, dS \right] \cdot n(r_i) \qquad (5)$$

where, $\bar{R} = (\bar{r} - \bar{r}_i)$, and

S_j refers to the area of the element

Computation of σ_{ij} is facilitated by replacing the uniform density doublet panel with its exact potential equivalent, a vortex ring of the same strength along the boundary curve enclosing the doublet area. The velocity influence coefficients are computed using the Biot-Savart law for each segment of the boundary vortex ring. It should be noted that due to symmetry, an exactly similar panel (box) exists on the other half of the wing with same strength d_j. The σ_{ij}, therefore, must include the effect of this box as well as the one shown in Figure 30.

For a wing, there exists a wake vortex sheet behind the trailing edge. The wake vortex sheet can also be represented by a distribution of uniform density doublets. The geometry of the wake sheet is prescribed in this analysis. Since the wake sheet is iniated along the bisector of the trailing edge angle, the trailing edge Kutta condition is satisfied.

The strength of the doublet panels in the wake can be related to the strength of the doublets at the trailing edge of the wing via the condition that there be no pressure discontinuity across the wake surface. For a steady flow, this dynamic condition can be represented by specifying that the doublet strength discontinuity is constant along the wake in the downstream direction. Quantitatively, the strength of a wake panel can be related to the difference of doublet strengths at the trailing edge of the wing.

48

$$(d)_{wake} = (d_u - d_e)_{t.e.} \tag{6}$$

where d is the density of doublets, and the subscripts refer to the locations of the doublet panels.

The influence coefficients, σ_{ij}, for the doublet boxes at the trailing edge can be adjusted to include the appropriate contribution from the wake element adjacent to such a trailing edge box. A typical wake panel used in the analysis is indicated in Figure 42 along with its vortex equivalent. This wake panel also has its image on the other half of the wing and the effect of the image is included in the computation of the velocity influence coefficient. Presently, the wake elements are assumed to extend to infinity downstream.

The righthand side of Equation 4, w_{n_i}, is the outward normal velocity at a control point on box i, and it includes the component of the free stream as well as the induced contribution from the free vortices. It is given by Equation 7 below

$$w_{n_i} = U_o \sin(\alpha_o - \theta_i) - (w_{n_v})_i \tag{7}$$

The extent of the wing surface over which Equation 3 is applicable (the attached region) is determined in an empirical manner (to be described later). The unknown d_j are assigned to the boxes in the attached region only and Equation 4 is applied at the control points of those boxes only. The resulting set of equations has as many unknown d_j as the number of equations and can be solved for the unknown d_js.

Once these doublets strengths are known, the induced velocity due to the doublets at any point on the surface can

be calculated. The vortex ring equivalents used in the calculation of the normal velocity are used in the calculation of the total velocity also. However, in the computation of the tangential velocity on the wing surface, care must be taken to account for the singularity in the computation of effects of the doublets. This is accomplished by calculating local velocity at a control point on the surface using the following formula

$$(\bar{q}_d)_i = \nabla d_i/2 + \sum_{\substack{j=1 \\ i \neq j}}^{N_A} (a_{ij} \, \hat{i} + b_{ij} \, \hat{j} + c_{ij} \, \hat{k}) \, d_j \qquad (8)$$

where ∇d_i is the gradient of the doublet density strength at a control point on the box i

a_{ij}, b_{ij}, c_{ij} are the velocity influence coefficients due to doublets of unit density on box j at a control point on the box i in x,y,z coordinate directions respectively

q_{d_i} is the velocity due to the doublets

This formula is obtained by taking the limit of the integral such as the one in Equation 5 when i = j. The velocity components such as a_{ij} etc. are obtained by using the vortex equivalents of the doublet panels.

The total velocity, $\bar{q}_i$, is obtained by adding the free stream velocity to $(\bar{q}_d)_i$. The pressure coefficient at a control point on the box i is given by the Bernoulli's equation as

$$(C_{P_{att}})_i = 1 - \frac{|\bar{q}_i|^2}{U_o^2} \qquad (9)$$

where U_o is the free stream speed

50

2.3.2. Pressure Coefficient in the Separated Region

The determination of the separated region is made based on a comparison of the aerodynamic angle of attack (the geometric angle of attack minus the induced angle of attack) and an empirical stall angle, α_s. Actual comparison in the computer program is made between w_{n_i}, the outward normal velocity, and a quantity $U_o \sin \alpha_s$. The box is considered separated if

$$w_{n_i} \bigg|_{outward} > U_o \sin \alpha_s \tag{10}$$

It is recognized that the computation of the pressure coefficient in the separated region is difficult because of the complex nature of the flow. An expression based on the Bernoulli equation is used to determine the pressure coefficient in the separated region. The expression for $C_{P_{sep}}$ is given below

$$\left(C_{P_{sep}} \right)_i = 1 - \frac{|\bar{q}_i|^2}{U_o^2} - \Delta Hi \tag{11}$$

where $\bar{q}_i$ is total velocity at the control point of the separated box, and

ΔH_i is the loss in the total pressure due to viscosity

The loss in the total pressure (ΔH) is usually small and hence is neglected in the computation of $C_{P_{sep_i}}$.

51

2.3.3. Pressure Coefficient Due to Vortex Suction

As mentioned before, the effects of the free vortices, such as the leading edge vortex, the strake vortex, or the tip vortex, are computed separately. The interaction of the free vortex with the wing is separated into the two basic mechanisms:

(1) the influence of the vortex induced velocity field, and
(2) the suction effect of the viscous core on the near field pressure distribution.

The induced effect is included in the potential solution via the term $\left(w_{n_v} \right)_i$. The manner in which the suction effect is considered will be outlined in the following section.

The near field pressure effects of the viscous cores of the free vortices are obtained by using a set of self-similar solutions of the Navier-Stokes equations. The coordinate system and the typical models used are shown in Figure 43. The details of the self-similar solutions and their applications to the free vortices in this problem are given in Reference 4. A brief outline of the analysis is presented here.

Basically, two viscous core models are used for each of the free vortices. In the region near the point of generation ($o < s < z_o$) in Figure 43, the core radius of the vortex is assumed to vary linearly with distance along the centerline, s. (The parameter, z_o, is given as an input).

In this region, the axial velocity in the core is much larger than the outside velocity. The self-similar solutions developed by T.R. Goodman in Reference 7 are used to obtain the incremental suction pressures due to the vortex in terms of the core radius, vortex strength and other local parameters.

52

The formulas obtained in Goodman's model are given below

$$r_c = C_r \, \alpha s$$

$$U_{max} = C_u \, \frac{\Gamma^2}{\nu_t s}$$

$$W_{max} = C_w \, \frac{\Gamma}{\alpha s}$$

and

$$\Delta C_{P_v} = -4 \left(\frac{W_{max}}{U_o} \right)^2 F \, (d/r_c) \tag{12}$$

with

$$F(d') = K_4 e^{-2K_5 d'} + \frac{K_1^2}{d'} \left(1 - K_2 e^{-K_3 d'^2} \right)^2$$

where r_c is the core radius

α is the turbulent eddy viscosity parameter

s is the distance along the centerline of the core

U_{max}, are the axial and tangential velocities at the
W_{max} center of the core and periphery respectively

Γ is the circulation strength around the vortex

ν_t is turbulent eddy viscosity

ΔC_{P_v} is the incremental suction pressure coefficient
due to free vortices

d is the distance of a point from the center of
the core in radial direction

53

U_o is the free stream speed, and

$C_u, C_w, C_r, K_1, K_2, K_3, K_4, K_5$ are constants which are
    obtained from the numerical solution.

The turbulent eddy viscosity parameter is given by

$$\alpha = \frac{.197}{\sqrt{R_n}} + .6 \text{ for } 10^3 < R_n < 5 \times 10^5$$

where R_n is the Reynolds number and is given by

$$R_n = \frac{\Gamma}{\nu} .$$

The actual contribution due to different vortices are appro-
priately added to get the total suction effect.

The axial velocity in the core of the vortex decreases
with distance s and at a point downstream becomes roughly
equal to the free stream speed. (This point is provided
through the parameter z_o as an input). Beyond this point,
Batchelor's vortex core model is used. The radius in this
region ($s > z_o$) is assumed to be proportional to the square
root of distance from a virtual origin. Self-similar solutions
developed by Batchelor are used in this region. The formulas
obtained from this model are given below

$$r_c = C_r \alpha (s_o + z_o) \sqrt{\frac{y_o + (s - z_o)}{y_o}}$$

$$V_\phi = \frac{\Gamma}{2\pi (d/r_c)} \frac{1}{r_c} x \left(1 - e^{-M_1 d'^2} \right)$$

$$V_a = \left(\frac{M_2 \Gamma}{2x} \frac{\alpha (s_o + z_o)}{r_c^2} \right) M_3 \cdot e^{-M_4 d'}$$

54

and

$$\Delta C_{p_v} = -4 \frac{V_\phi{}^2 + V_a{}^2}{U_o{}^2} \tag{13}$$

where $\quad S_o = \dfrac{r_{c_o}}{C_r \alpha}$

$$y_o = \frac{M_5 \, \alpha \, U_o \, (s_o + z_o)^2}{\Gamma} \, 2\pi$$

V_ϕ, V_a are the tangential and axial velocities at a point "d" distance away from the core center in the radial direction

M_1, M_2, M_3, M_4, M_5 are constants

The numerical values of the constants used in the above equations are given in the documentation in the appendix.

In general the strength and the geometry of the vortex is not known apriori. The estimates of the strength are made from the leading edge bound vorticity strength obtained in the totally potential solution (no vortices, no separation). The geometry of the free vortices is obtained by making it force free under the prevailing velocity field, that is, the tangent to the centerline of the vortex is made parallel to the velocity vector at that point on the vortex. The velocity vector under consideration here is given by

$$\overline{q} = \overline{q}_d + \overline{q}_v + \overline{q}_a + U_o \tag{14}$$

where $\overline{q}$ is the total velocity vector

$\overline{q}_d$ is the velocity induced by wing doublets

55

$\bar{q}_v$ is the velocity induced by the vortices including the self-induced velocity

$\bar{q}_a$ is the axial velocity present in the core of the vortex

U_o is the free stream velocity.

It is obvious at this point that velocity $\bar{q}$ in Equation 14 depends on the wing doublet solution and velocity $\bar{q}_v$ in Equation 3 depends on the strength and the geometry of the free vortices. The combined problem of obtaining the doublet strength on the wing and the geometry and the strength of the free vortices is a nonlinear one. Therefore, an iterative procedure is used, wherein, first, a geometry and strength for the vortices is prescribed as an initial guess. The doublet strength on the wing is computed based on this input geometry. The vortex geometry is then displaced to satisfy the force free condition. If the displaced geometry is significantly different from the initial geometry, the process of obtaining the doublet solution and new vortex geometry is repeated. The final solution is obtained when there is no significant difference between the two consecutive geometries of the free vortices.

The pressure calculations are done only after the iterative process discussed above is completed.

2.3.4 Theoretical and Experimental Correlation

A computer program based on the analysis presented earlier was developed and used to compute the loads and pressure distribution on the Navy F-4 type wings. Several applications of the program to the basic wing and basic wing and strake configurations were presented in Reference 4.

56

The program used in the above computations was stream-
lined to facilitate its use by outside users. Some of the
changes involved making the coordinate system consistent with
that used by others in this field. Certain input-output for-
mats were changed to clarify the usage. Also, certain repe-
titious calculations were eliminated resulting in a somewhat
more efficient execution of the program. A documentation of
the program was prepared and is included in this report as an
appendix.

The validity of the potential flow model used in the
program was demonstrated in Reference 4. The program was used
to compute the pressures and the loads on the wing at 13.1°
angle of attack with the assumptions that there are no free
vortices in the flow field and the flow over the entire wing
is fully attached.

The pressure distribution along a chord located at
approximately 15% semi-span is compared with experimental
values in Figure 44. This spanwise station was selected
because it was thought that the influence of a relatively weak
leading edge vortex is negligible at this station. These
results indicate a fairly good correlation except near the
trailing edge where some numerical problems could be expected
because of the relative closeness of the upper and lower sur-
faces. The value of the total integrated lift coefficient cal-
culated was .65 which agreed well with the experimental value
of .68.

The program was then used to compute pressures and
loads on the Navy wing-strake combination at higher angles of
attack of 21.6° and 27.7°. The wing planform and the geometry
of the free vortices is shown in Figure 45 for the angle of

57

attack of 21.6°. The geometry of the free vortices was obtained from the flow visualization results and pressure distributions obtained experimentally. The vortices were made to follow the paths of the pressure peaks observed on the wing.

Certain changes were made in the input to the program as compared to the input used in the runs made to obtain results presented in Reference 4. The box structure was made identical on both the upper and lower surface with 96 boxes representing each surface. Also, the initial portion of the leading edge vortex was modeled to include elements with variable vortex strengths. This change was made to better represent the growth in the vortex strength in the region where vortex is being fed from the wing. The vortex elements following this variable strength region are assumed to have a constant strength.

The formation and the growth of the leading edge vortex takes place in the leading edge region of the wing and, therefore, its strength is derived from the doublet strength solution at the control points on the leading edge boxes. The variation of the difference in the doublet strengths on the upper and lower surface at control points on the leading edge boxes is used to obtain the strength of the variable strength elements of the vortex. The vortex is assumed to be fed from the wing until the point where the above doublet strength difference variation at the leading edge reaches a maximum. Thereafter the vortex is assumed to have a constant strength equal to the maximum of the difference in doublet strength at the leading edge.

The comparison of the predicted pressure coefficients with the experimental values is shown in Figures 46a through 46f. These plots compare the pressure coefficients at several

58

spanwise locations on certain constant x/c lines. It is seen
that the agreement between the calculated and experimental
results is fairly good. Some discrepancy exists near the tip
region and in the aft region of the wing (for x/c = .6 and .8).

Examination of the predicted results indicates that
this discrepancy is due to the pressure computation in the
separated boxes and in the attached boxes immediately next
to the separated region. Since the doublet strength in the
separated boxes is forced to be zero, the velocities computed
at the control points on the attached boxes are unduly large
making the pressure coefficients there unrealistic. Also, the
actual doublet distribution in the attached region gets con-
siderably altered when separated region exists on the wing.
This distribution is particularly affected near the separated
region which acts as a"hole" in the potential body since no
no-flow boundary conditions are satisfied at the boxes in the
separated region.

It is believed that inclusion of the separated boxes
in such a manner is probably not accurate and yields unrealis-
tic results. An alternative approach to this problem can be
suggested in which the flow situation is initially considered
to be entirely potential (no separation) so that no-flow bound-
ary condition is satisfied over the entire wing. The resulting
solution is then used to yield the pressure distribution which
is used to determine the separation region and the pressure in
that region. Certain criteria based on the impressed potential
pressure distribution and the boundary layer theory will have
to be developed for this purpose.

59

The program is also seen to overpredict the pressure on the lower surface at $x/c = 0.05$. It is thought that the leading edge separation occurs on the lower side of the wing considering the high angle of attack whereas the analysis considers the whole lower side of the wing to be attached. Also, a certain amount of numerical inaccuracies exist in this region since the chordwise size of the boxes in this region is very small.

In terms of the suction peaks and their location, the agreement seems to be reasonably good. The peaks are still (as compared with the results shown in Reference 4) slightly too narrow and too large, however, the error can be considered to be small. This agreement can be improved by further adjusting the vortex parameters such as the core radius of the vortex.

The wing planform and the final geometry of the vortices used in the computation for the angle of attack of 27.7° is shown in Figure 47. The vortex geometry in this case is also obtained from the flow visualization pictures and experimental pressure distributions. The comparison of the calculated and observed results is shown in Figures 48a through 48d. It can be seen that the agreement between the computed and observed results is fairly good near the forward portion, whereas, the agreement deteriorates in the aft portions. The reasons for these discrepancies, as suggested earlier, may be due to the inaccurate modeling of the separated flow. The separated flow effects are probably stronger at this angle of attack than at 21.6°.

The integrated lift performance of the wing at angles of attack at 13.1°, 21.6° and 27.7° is shown in Figure 49. It is seen that the total lift coefficient in all three cases agrees very well with the observed values.

It is noted that these results are based on certain empirical parameters such as the initial core radius, the vortex strengths of the strake and tip vortices, and the stall angle used in the determination of the separated region. With a good choice of these parameters the results obtained in the above cases appear to be quite good.

The present program was also used to compute the pressure distribution for a delta wing. The delta wing configuration for which the calculations were made is shown in Figure 50 with the vortex geometry superimposed. The geometric data used here was obtained from Reference 8. The delta wing under consideration is a flat delta wing with aspect ratio 1.15 and beveled sharp edges. The flow on this wing separates at the leading edge almost immediately as the angle of attack is increased from zero and forms a vortex sheet that eventually rolls up into the leading edge vortex. An estimate of the vortex geometry of the rolled up vortex core was done based on Smith's conical theory. The strength of the vortex based on the doublet solution in the leading edge region, however, yielded rather low values. A probable reason for this may be that the development of the vortex in this case is a much slower process as compared to that in the Navy wing and should in fact include a roll-up sheet which is presently not included in the program. A somewhat empirical approach was, therefore, taken to obtain results for the delta wing. Using geometry obtained from Smith's conical theory and by adjusting the vortex strength, a good agreement was obtained between the predicted total lift and the experimental value. The computed pressures for this case are presented in Figures 51a through 51c. The figures show the plots of the pressure coefficients along the constant x lines. These comparisons indicate that the program underpredicts the pressure in the root section near the apex (e.g. $x/c_R = .4$) and it also predicts large pressure

61

peaks very near the leading edge of the wing. The under-prediction of pressure near the root is probably because the value of the core radius used in this case is smaller than the one that should be used since the vortex over a delta type wing is less tightly rolled compared to that over a low aspect ratio swept wing. The peaks near the leading edge are the result of the leading edge singularity which results from not satisfying the leading edge separation (the Kutta condition) condition and also from the lack of the presence of a roll-up vortex sheet. It is noted here that the entire flow on the delta wing was forced to be attached.

It is noted that in all the computations presented above, a good knowledge of the vortex location to be inputted to the program is necessary. It is very difficult, under the framework of present theory, to obtain a stable force-free geometry starting from an arbitrary starting geometry. The procedure used to obtain the force-free geometry aligns the geometry of the present vortex with the calculated total velocity and the calculated total velocity tends to pull the vortex to the free stream direction. This results from the fact that the induced velocity at the control points on the vortex is not sufficient to keep the vortex from moving in the free stream direction. As a matter of fact, the spanwise velocity at certain control points appear to aggravate the situation further instead of alleviating it.

The movement of the vortex in the vertical direction is somewhat more orderly except in the region near the leading edge and the apex where the vortex is very close to the wing surface and where the induced velocities may be expected to be inaccurate because of the numerical problems.

In the case of the low aspect ratio swept wing certain guesses about the path of the leading edge vortex can be made based on the doublet distribution on the wing as described in Section 4.7 of Reference 4. However, a better estimate of the geometry can be obtained based on the flow visualization studies and experimental pressure data.

In the case of delta type wings with very low aspect ratios, the geometry can be derived from Smith's conical theory or experimental data if available. However, further investigations into the vortex motion and development of different criteria to obtain a stable final geometry starting from an arbitrary initial location is necessary.

Finally, it is noted that execution of the program is extremely efficient. For example, the run time for a low aspect ratio swept wing case with three free vortices, 192 boxes on the wing is approximately 24 seconds on CDC7600 Cyber 74 system. A similar case on the NASA Langley Research Center cluster requires 44 seconds on Cyber 175 series machine.

Based on the results presented above, the following conclusions can be made:

1. The program provides a good correlation between the predicted and observed total lift and pressure distributions on the F-4 type wings when certain empirical parameters are known.

2. The program also provides reasonably good results for delta type wings, but, certain refinements in the program such as inclusion of a leading edge sheet may be necessary to improve the correlation.

3. The separated flow arising from the turbulent transition poses a formidable problem in the analysis within the framework of the potential theory. It is believed that

63

certain problems introduced by the separated flow as treated in the analysis can be removed if the determination of the separated region and the pressure there is made after the full potential flow solution is obtained. Such a treatment of the separated flow will include the use of the boundary layer theory and impressed pressure distribution calculated during the fully potential flow analysis.

4. The problem of the theoretical prediction of the geometry of the leading edge vortex needs further investigation.

5. The program execution is very efficient and therefore it can be used as a good tool to obtain reasonably good results rather inexpensively.

3. CONCLUSIONS

Experimental

On the basis of the experimental investigations that were conducted using wind tunnel models, the following general conclusions can be made:

- Through the use of the controlled vortex flows interacting with a low aspect ratio swept lifting surface, a very large increase in $C_{L_{max}}$ can be achieved.

- The increase in C_L is accompanied by a destabilizing moment which, it was shown, can be controlled with a nominal size tail surface properly located in the wake.

In addition to the above general conclusions, more specific conclusions can also be made. They are listed below.

1. With an appropriate combination of leading edge devices such as strakes, snags, etc., the maximum lift coefficient of a lifting surface could be increased by about 60% as compared to the basic wing without these devices.

2. The lift curve slope for the configuration with the leading edge devices was linear with angle of attack up to an angle of about 29° whereas the lift curve slope for the basic wing started reducing at about 15° reaching a minimum at about 25° where $C_{L_{max}}$ occurs.

3. Lift to drag ratios of the wing with most advantageous vortex control devices did not change substantially from that of the basic wing with no vortex control devices.

4. The most beneficial vortex-control configurations were those which involved at least two interacting vortices which provided mutual stabilization and strengthening as the angle of attack was increased above the stall angle of the basic wing.

65

5. The surface pressure distributions measured for the various configurations indicated that the additional lift obtained by the vortices interacting with the lifting surface was primarily due to the low pressure region in the vortex cores acting on the lifting surface.

6. The paths of the vortices over the surface of the wing were controlled primarily by the mutually induced effects of the vortices and the induced effects of the lifting surface.

7. The lift curve slope in the lower angle of attack range (5° to 15°) could be increased significantly by inducing leading edge separation by means of a sharp edge separator plate along the leading edge.

8. External appendages having two free edges which generated vortices of opposite sense outside of the pressure field of the lifting surface were not effective in enhancing the wing vortex field and thus the lift at high angles of attack.

9. Planform tailoring in the leading edge region such that only a single free vortex is formed within the wing pressure field had the greatest potential for increasing the lift capabilities of a wing at high angles of attack due to favorable interacting vortex flows.

10. Over a wide range of wing angle of attack $0° < \alpha_\omega < 30°$, the tail effectiveness, $\frac{dCm}{d\alpha_t}$, remained relatively constant.

11. The aerodynamic angle of attack at the tail surface never exceeded 10° even though geometric angle with respect to the free stream was as high as 24°. This is mainly due to the induced effects of the wing surface and vortices at the tail surface.

12. Depending on the longitudinal and vertical location of the tail surface relative to the wing, the tail drag can have a significant effect on the trim of the total configuration.

66

Theoretical

On the basis of the results obtained using the theoretical prediction technique that was developed, the following conclusions were drawn:

1. In terms of the theoretical analysis, it was concluded early in the program that existing theories and predictive techniques were inadequate in predicting the performance characteristics of the lifting surfaces with leading edge vortex control devices.

2. Interaction of a vortex on the suction side produced beneficial increments in the suction lift; the vortices formed within the pressure field of the vortex had a more beneficial effect as compared to the free vortices generated by devices upstream.

3. Theoretical analyses to be used in the prediction of the loads and pressures on low aspect ratio swept or delta wings should include the treatment of the nonlinear suction effects and turbulent transition separation of the flow within the framework of a lifting surface theory.

4. The application of the prediction technique to a low aspect ratio wing (F-4 Phantom wing planform) has shown that fairly good correlation can be obtained between the predicted and experimental pressure distribution over the wing planform.

5. The application of the theoretical prediction technique to low aspect ratio delta wings has shown that only a fair correlation was obtained between predicted and experimental results. The lack of good correlation is believed due to the absence of a connecting vortex sheet between the core of the vortex and the leading edge in the lifting surface.

6. The application of the prediction technique has also shown the existence of slow divergence of the predicted leading edge vortex geometry. This may be due to the inaccurate modeling of the induced effects of the mixed flow (potential

67

and separated flows) over the wing planform, the empirical
treatment of the separated flow over the wing or the absence
of a roll-up vortex sheet between the vortex core and the
leading edge.

   7.   In spite of some limitations in the prediction tech-
nique, it can be used to generate realistic pressure distribu-
tions over low aspect ratio wings quickly and inexpensively
and thus is useful for design studies of advanced wing
configurations.

4. RECOMMENDATIONS

Based on the research investigations that were conducted, the following recommendations are made:

1. The theoretical analysis be modified to account for yawed flight.

2. The theoretical analysis be expanded to include control surfaces, such as the horizontal and/or vertical tail, and the fuselage in order to study the effect of the strong vortex flows on the static stability characteristics of aircraft configurations.

3. The basic potential flow theory be modified to include the effects of the leading edge vortex sheet which rolls up into the leading edge vortex.

4. An improved model of the vortex core breakdown be developed and incorporated in order to make the analysis less empirical.

5. The vortex position iteration be altered in order to provide convergence of the vortex geometry starting from an arbitrary position.

6. The treatment of the separated flow be improved by applying more realistic boundary layer separation criteria. This should remove some of the numerical problems associated with the calculation of the separated flow regions.

REFERENCES

1. White, Richard P. Jr. and Zalay, Andrew D., "High Lift Generation by the Use of Vortices", RASA/SRL Report No. 74-12, December 1974.

2. White, Richard P. Jr. and Balcerak, John C., "An Experimental Investigation of Vortex Flow Control for High Lift Generation", ONR CR212-223-2, December 1975.

3. White, Richard P. Jr., Gangwani, Santu T. and Balcerak, John C., "A Theoretical and Experimental Investigation of Vortex Flow Control for High Lift Generation", ONR CR212-223-3, December 1976.

4. White, Richard P. Jr., Gangwani, Santu T. and JanakiRam, D.S., "A Theoretical and Experimental Investigation of Vortex Flow Control for High Lift Generation", ONR CR212-223-4, December 1977.

5. Sheath, D.D., "Vortex Airfoil Interaction Tests", Proceedings of the AIAA 2nd Atmospheric Flight Mechanics Conference, September 1972, Palo Alto, California.

6. Mullans, R.E. and Lemley, C.C., "Buffet Dynamic Loads During Transonic Maneuvers", AFDL-TR-72-46, September 1972.

7. Goodman, T.R., "The Vortex Core Jet Near the Point of Generation", AFOSR TR-72-1158, Oceanics, Inc., Report No. 72-91, April 1972.

8. Wentz, W.H., "Effects of Leading Edge Camber on Low Speed Characteristics of Slender Delta Wings", NASA CR112016, 1972.
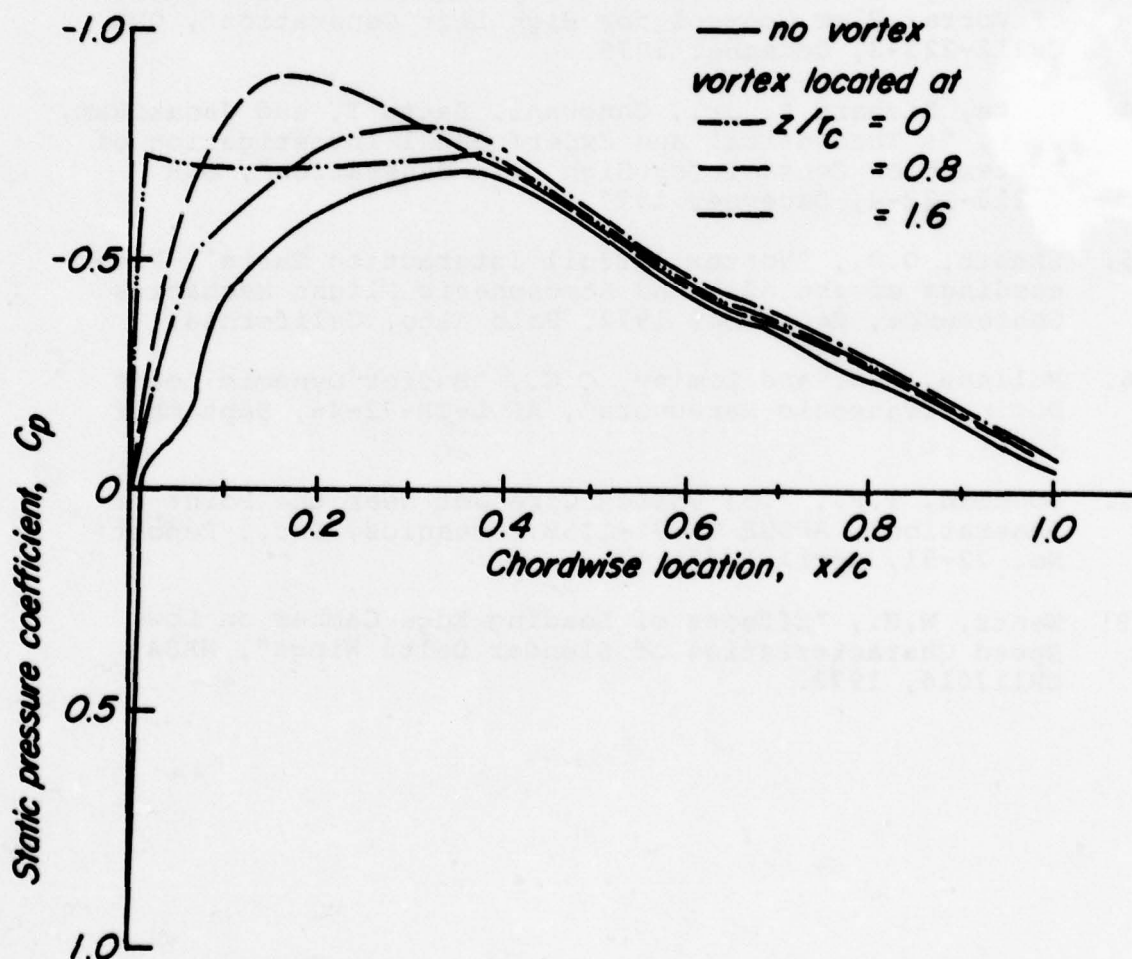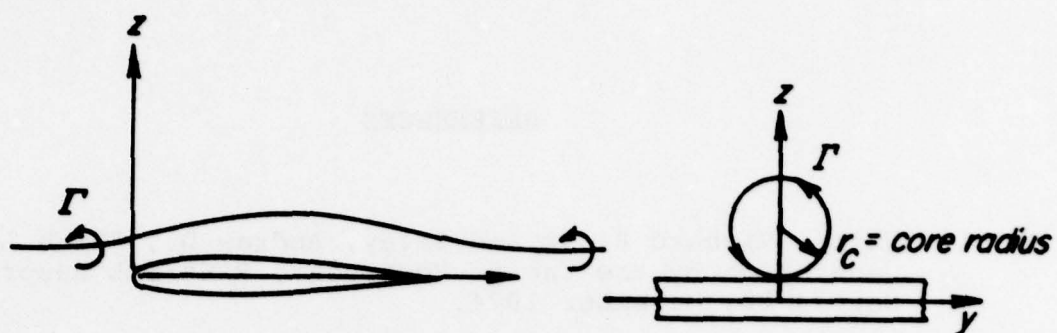
FIG. 1   Chordwise pressure distribution on the upper surface
of a symmetric airfoil due to a free vortex interaction
at $\alpha=0°$, $M_\infty=0.09$ (from ref. 5.).
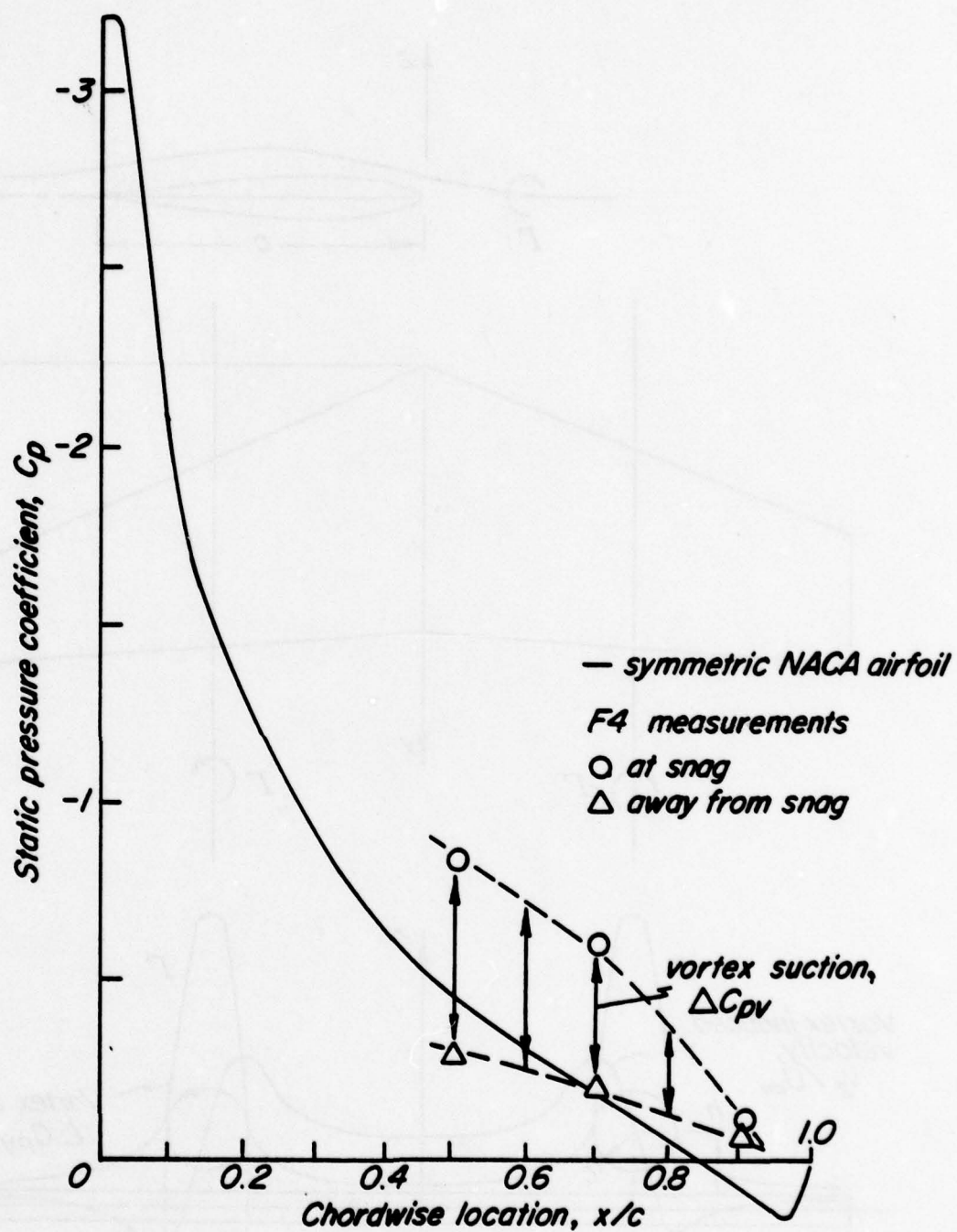
FIG 2.   Chordwise pressure distribution on the upper surface
of the F-4 wing at $\alpha=8^{\circ}$, $M_{\infty}=0.7$ due to a snag vortex
wing interaction (from ref. 6.).
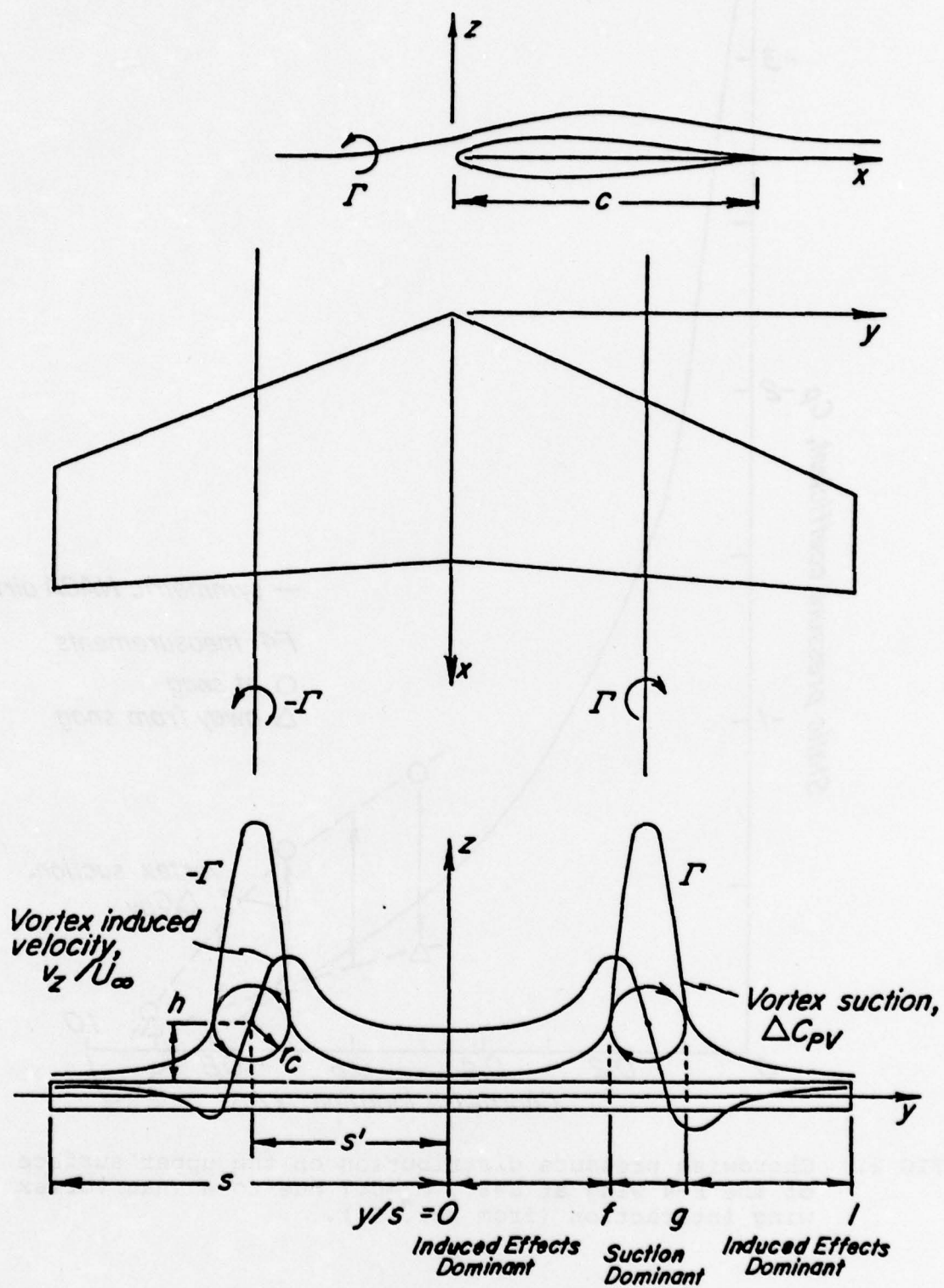
FIG. 3. Simplified wing vortex interaction model.

73
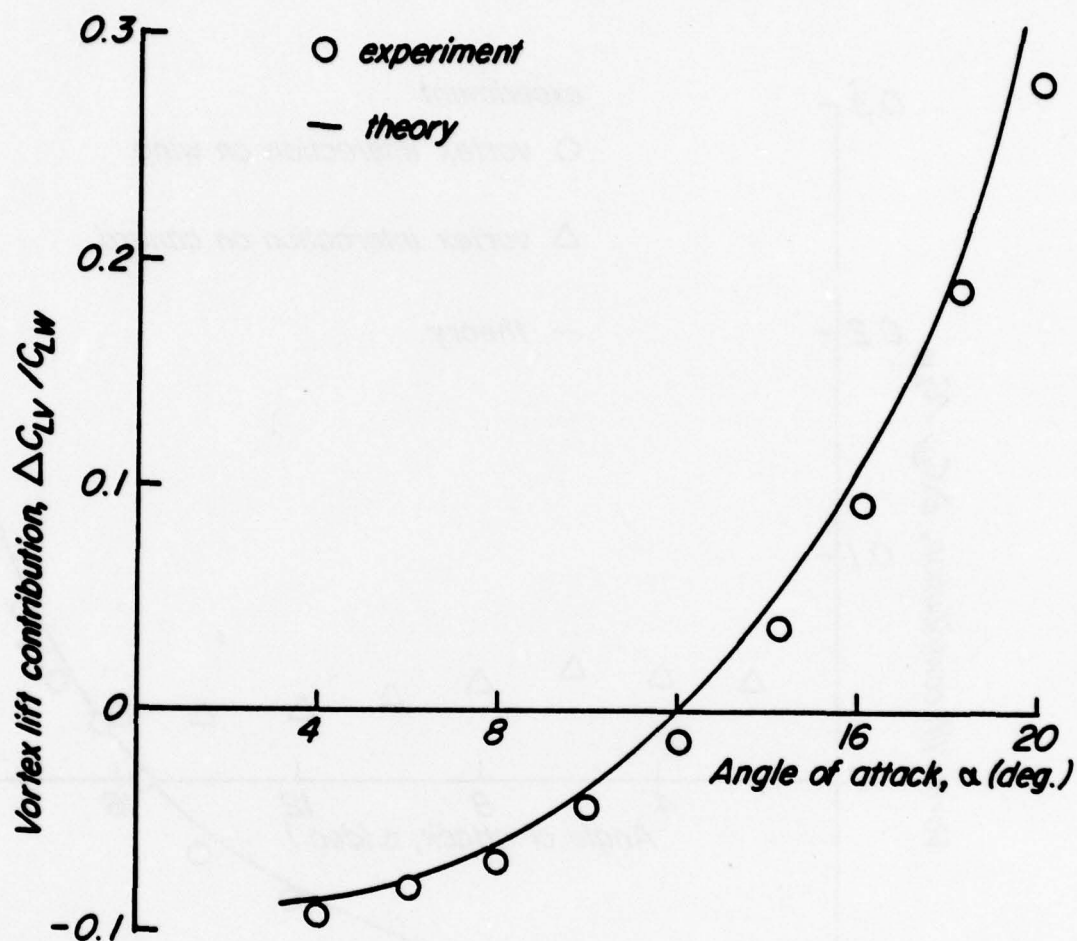
FIG. 4. Vortex lift as a function of angle of attack for the strake wing configuration.
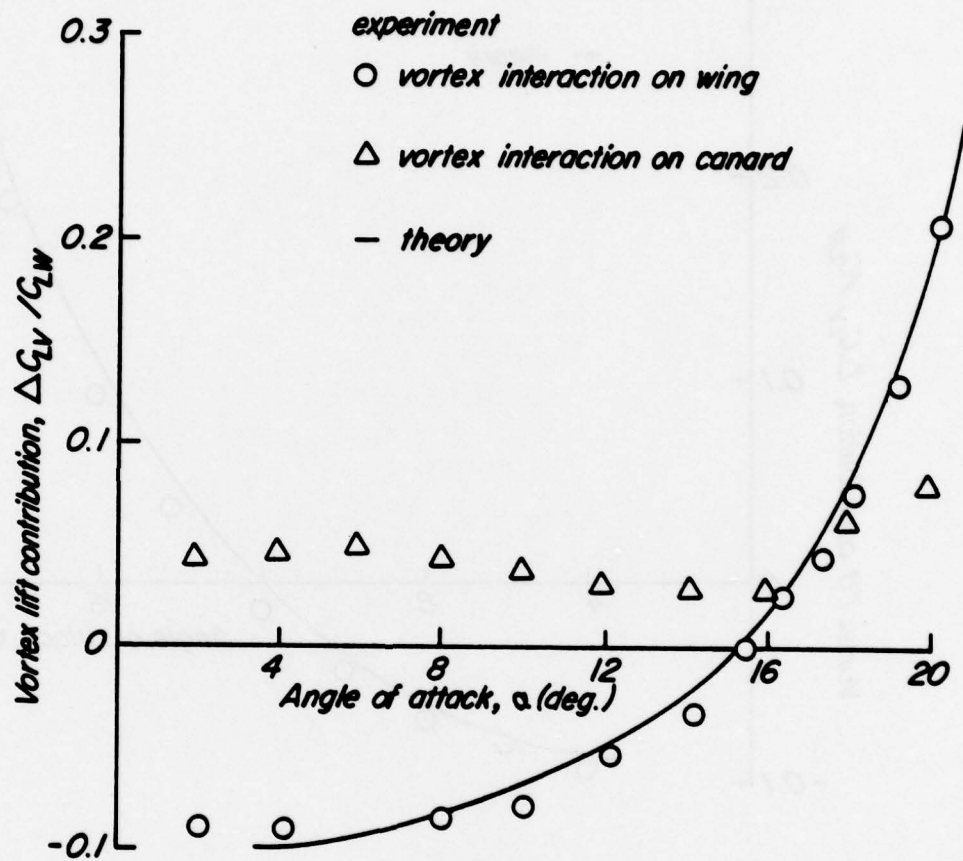
FIG. 5. Vortex lift as a function of angle of attack for the
close coupled canard configuration.
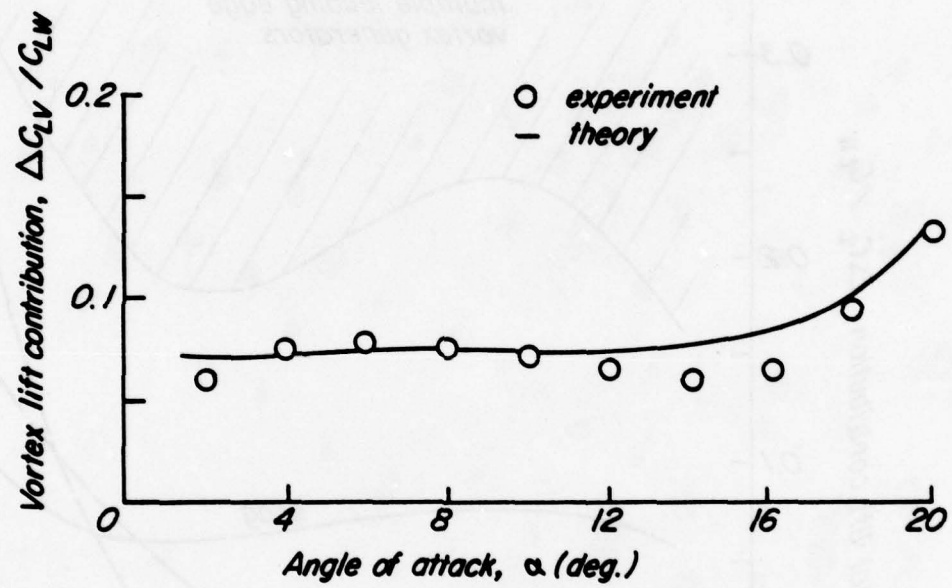
FIG. 6 Vortex lift as a function of angle of attack for the snag wing configuration.

the framework of the potential theory. It is believed
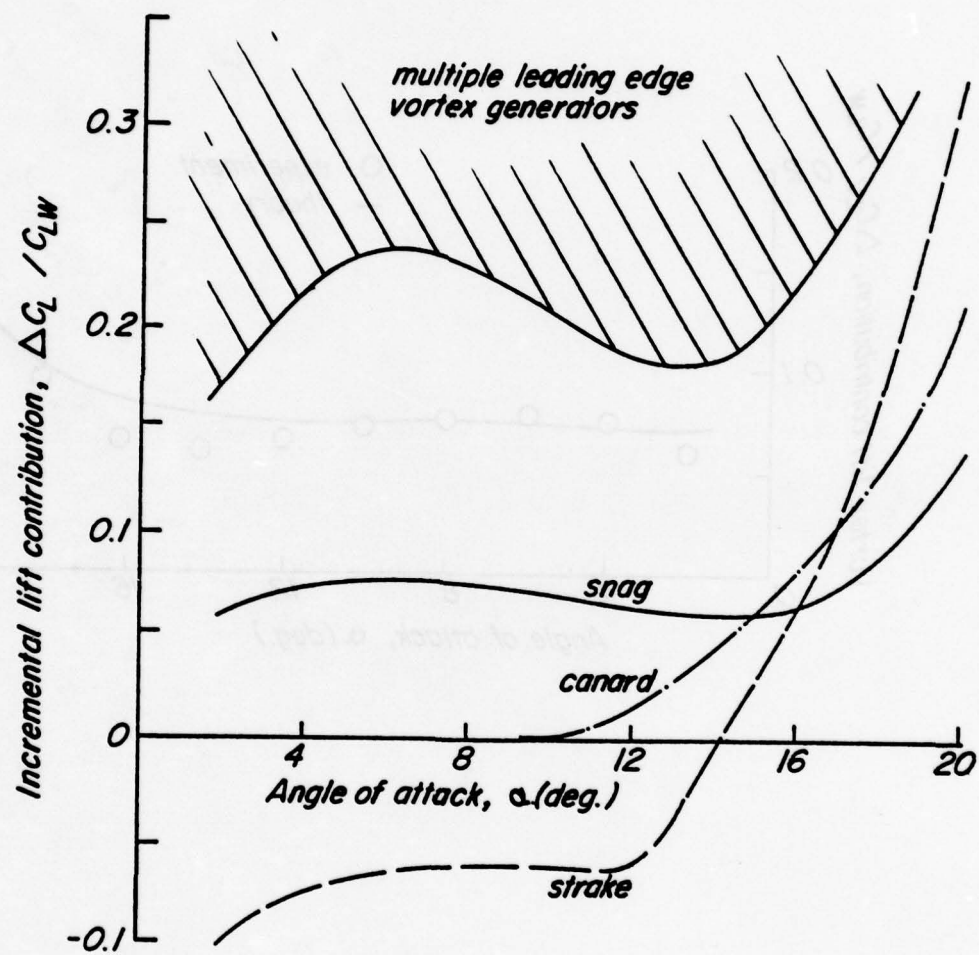
FIG. 7. Comparison of the incremental lift contribution of
different high lift devices.
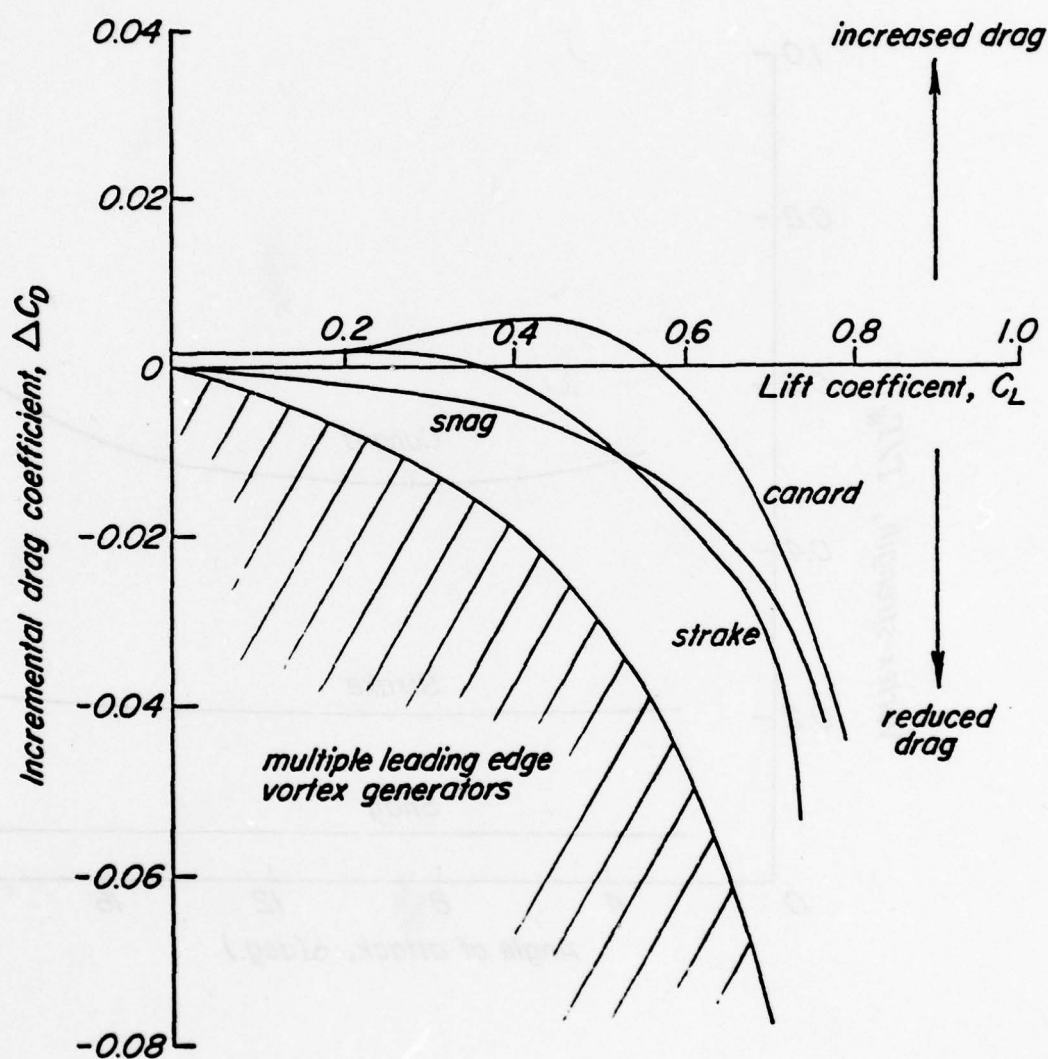
FIG. 8. Comparison of the incremental drag performance of different high lift devices.
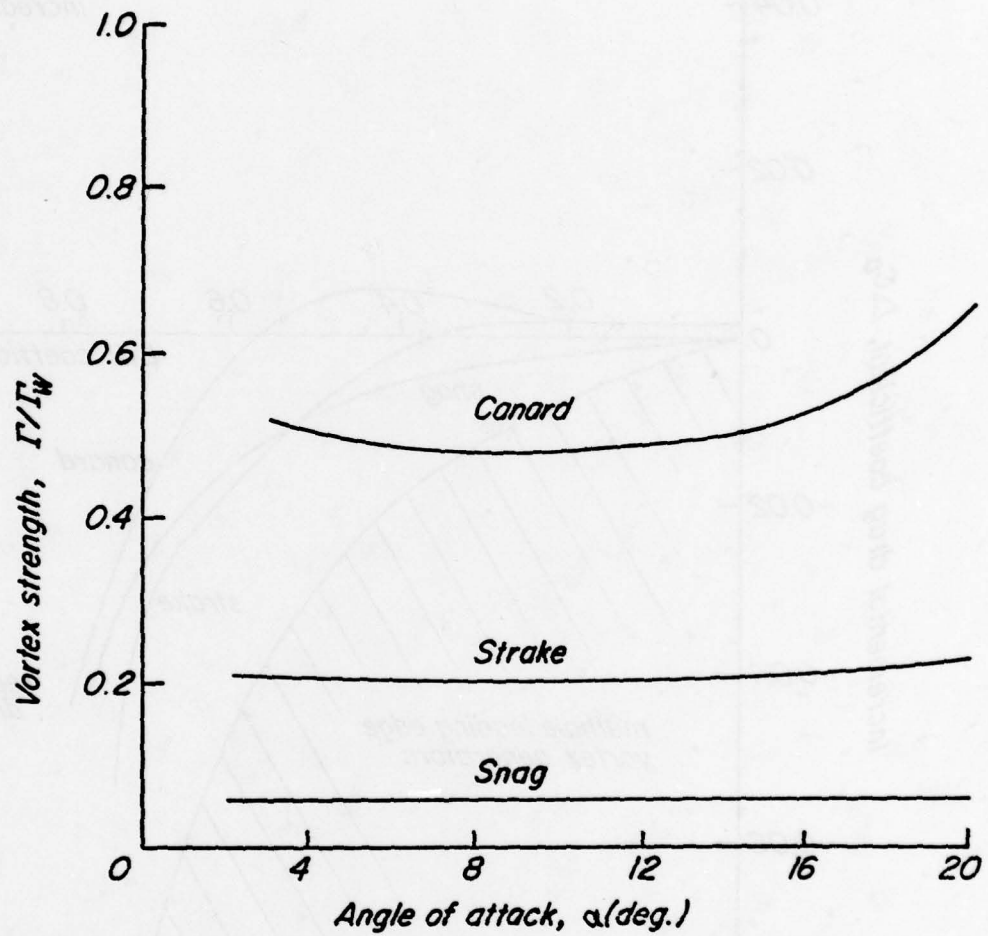
FIG. 9. Circulation strength as a function of angle of attack
for the snag, canard, and strake vortex.
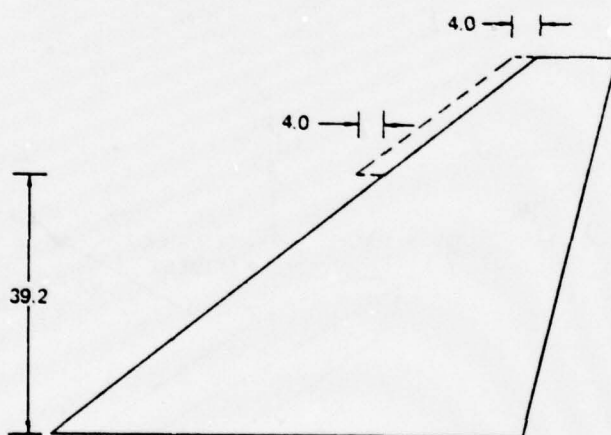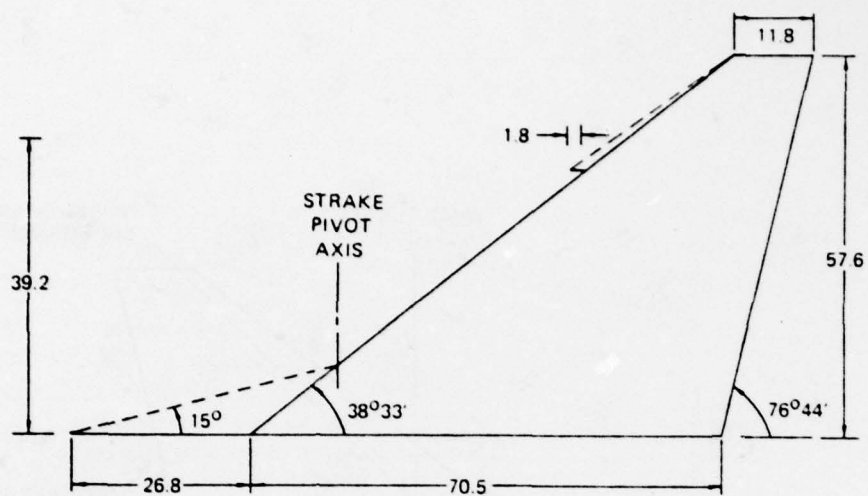
ALL DIMENSIONS ARE IN INCHES

FIG. 10.   Model Planform

80

WIND TUNNEL
$\mathbb{C}_L$

MODEL QUARTER
CHORD LINE

MEAN AERODYNAMIC
CHORD = 48.12″

21.96″

AIRFLOW

SIDE
FORCE

PITCHING
MOMENT

LIFT

YAWING
MOMENT

WING ROOT CHORD

ROLLING
MOMENT

DRAG

FORCES AND MOMENTS ARE POSITIVE
AS SHOWN
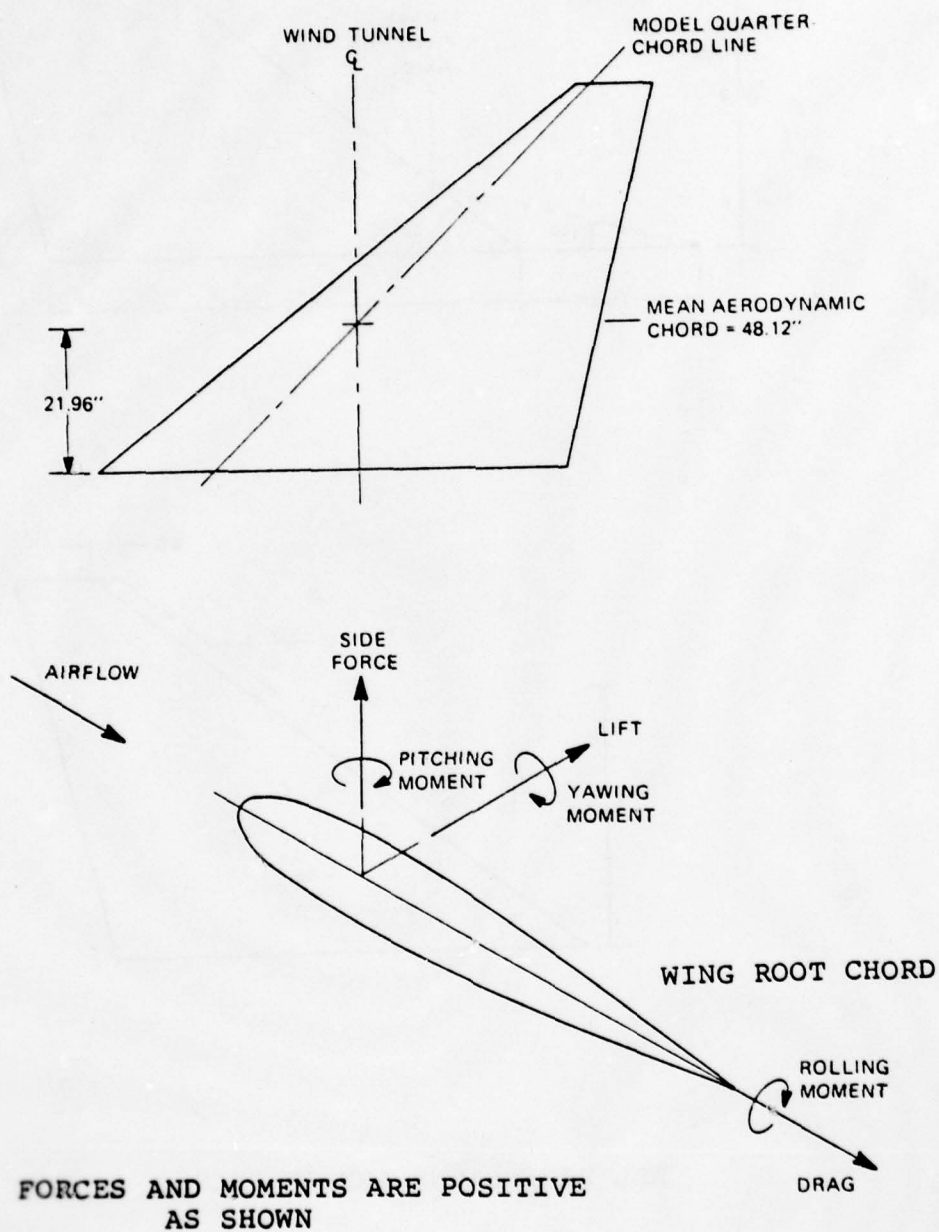
FIG. 11. COORDINATE SYSTEM FOR BALANCE
MEASUREMENTS

81
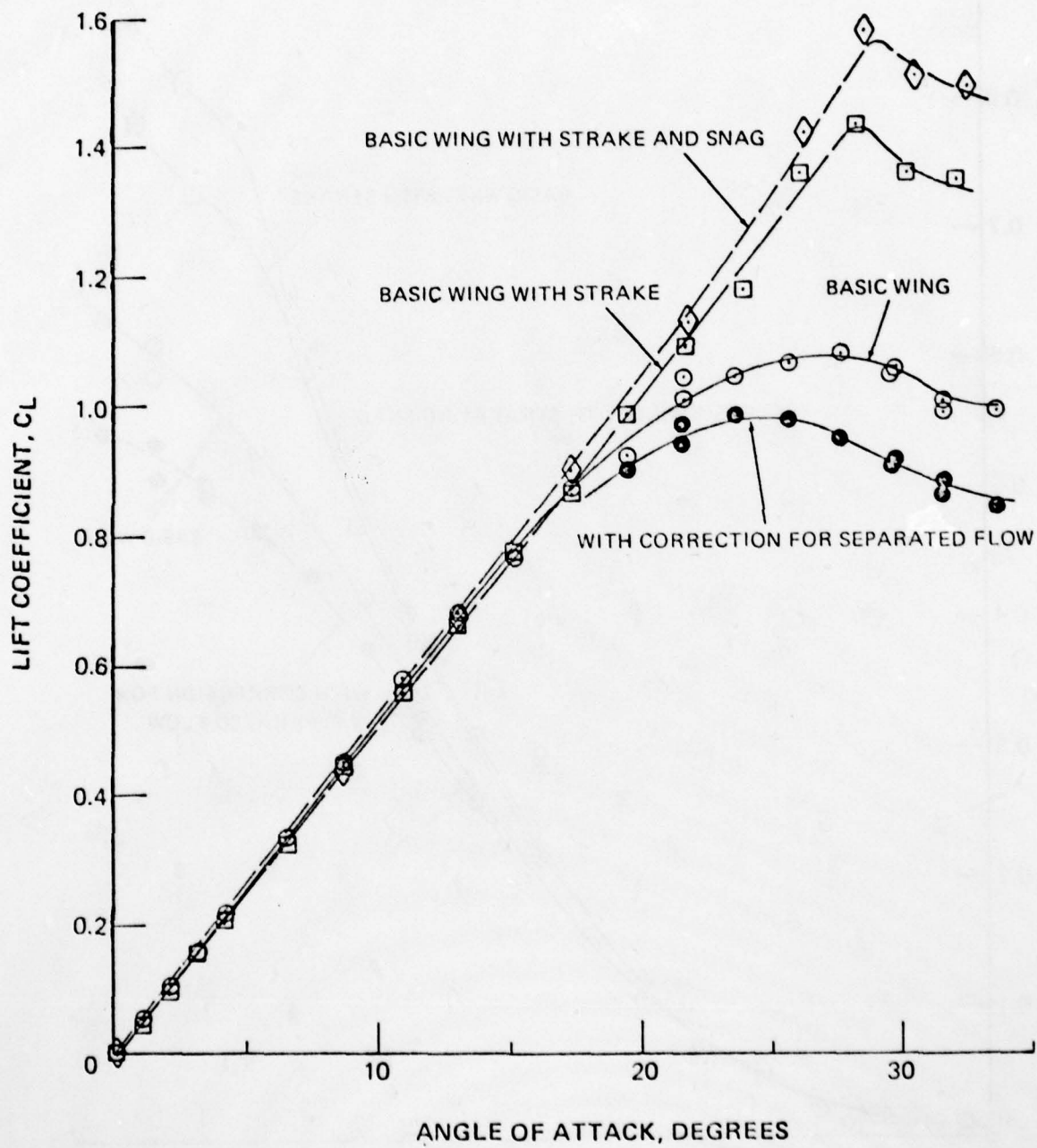
FIG. 12.   LIFT COEFFICIENT VS
          ANGLE OF ATTACK

82
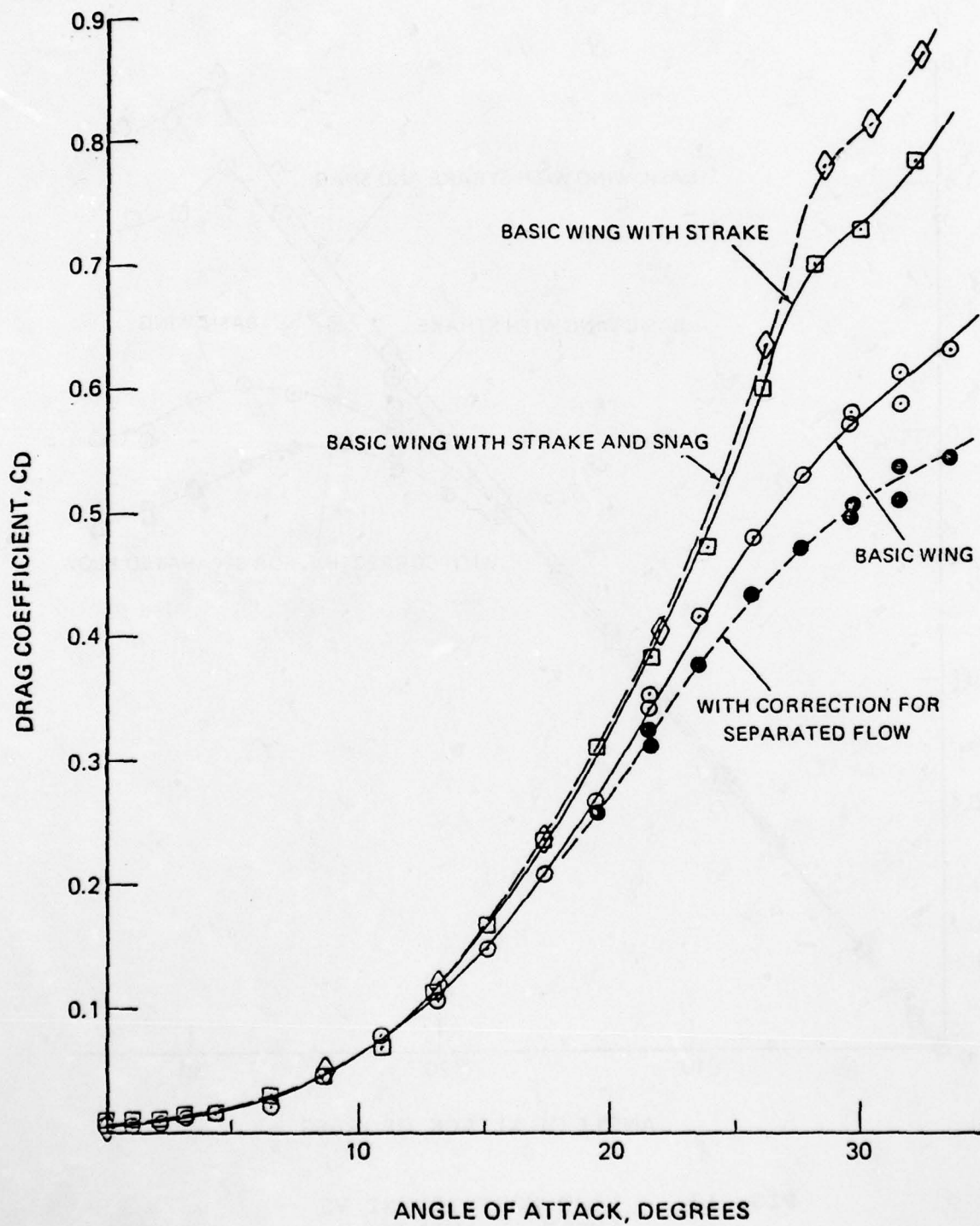
FIG. 13. DRAG COEFFICIENT VS
ANGLE OF ATTACK

83
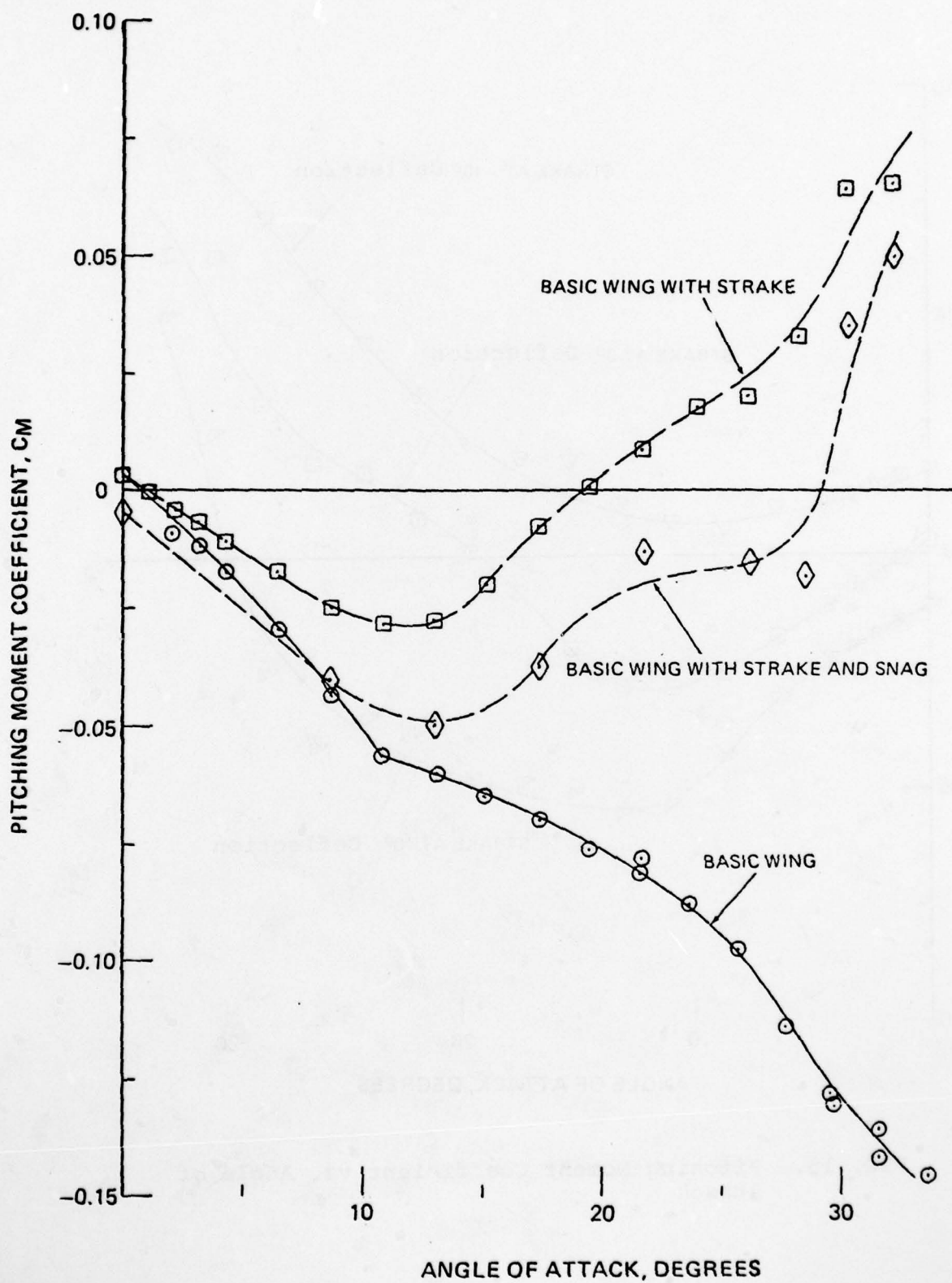
FIG. 14. PITCHING MOMENT VS
ANGLE OF ATTACK

84
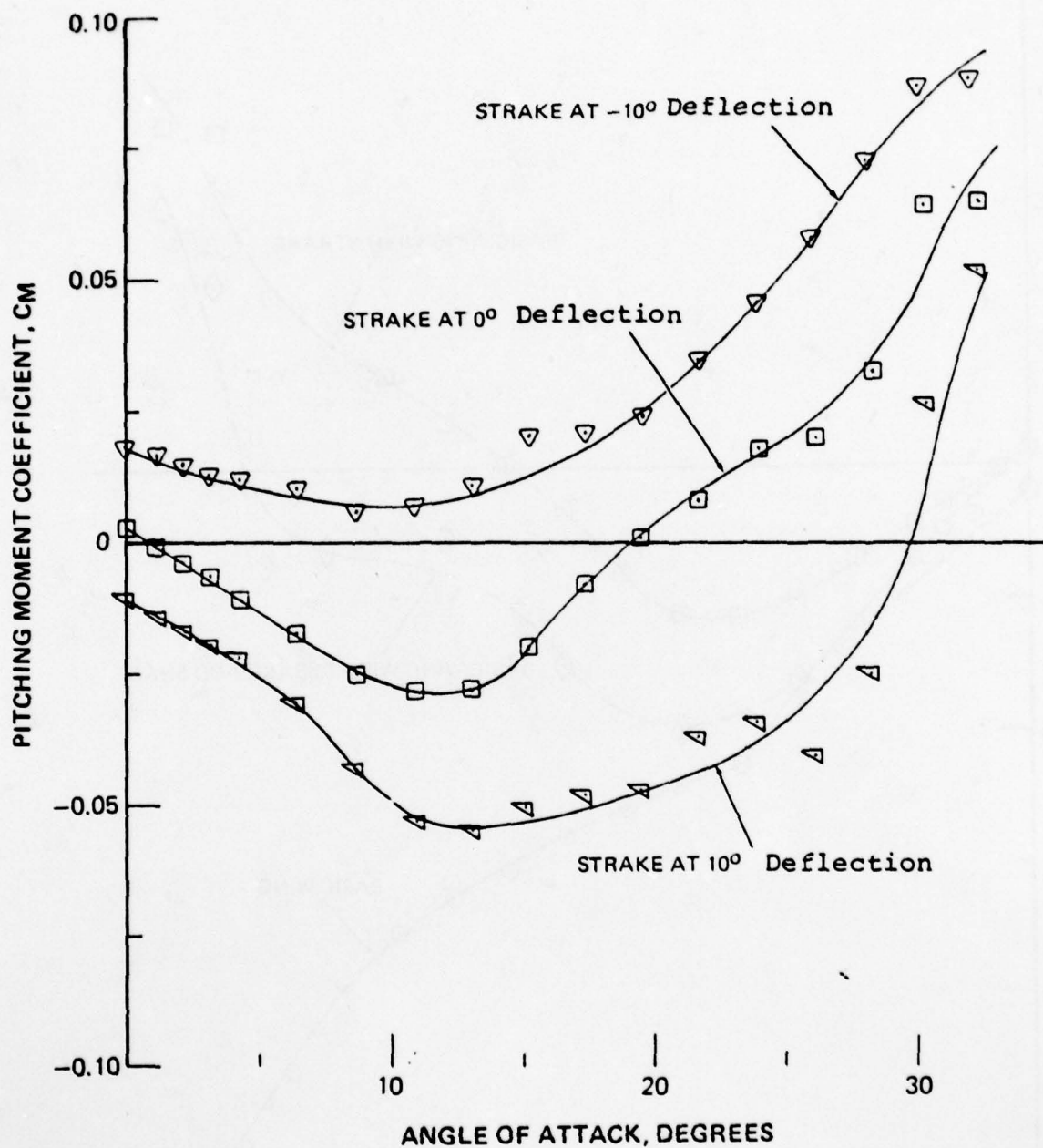
FIG. 15.   Pitching Moment Coefficient vs. Angle of
Attack
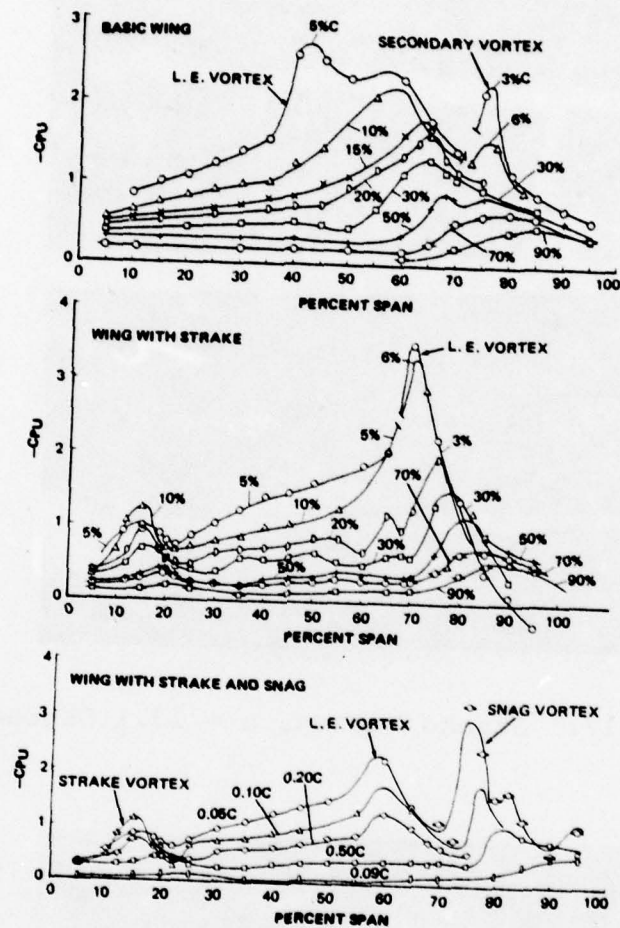
FIG. 16.   Upper Surface Pressure Distributions
           α = 13.1 Degrees.

SEMI-PLAN VIEW

LOOKING TOWARD ROOT

FIG. 17.   Strake Vortex, α = 13.1 Degrees.

PARTIAL STALL

PATH OF THE
LEADING EDGE VORTEX

POTENTIAL FLOW

PATH OF THE
STRAKE VORTEX
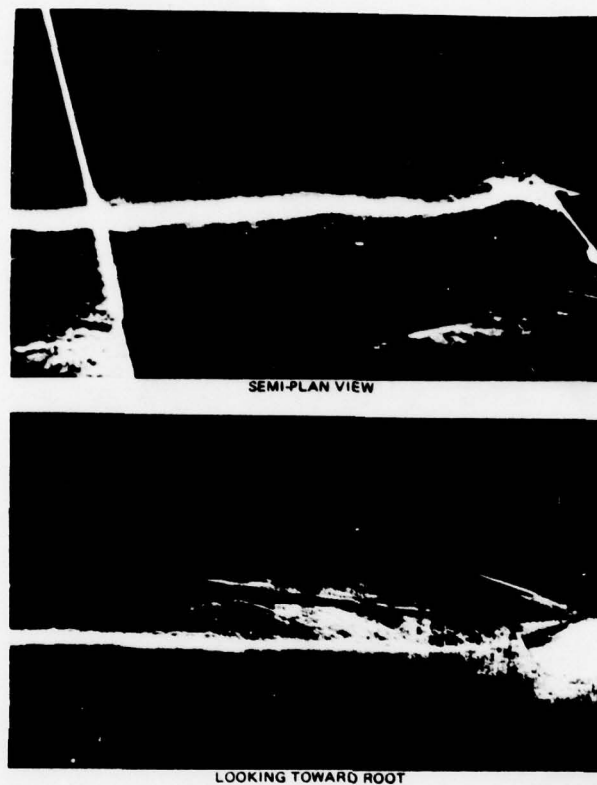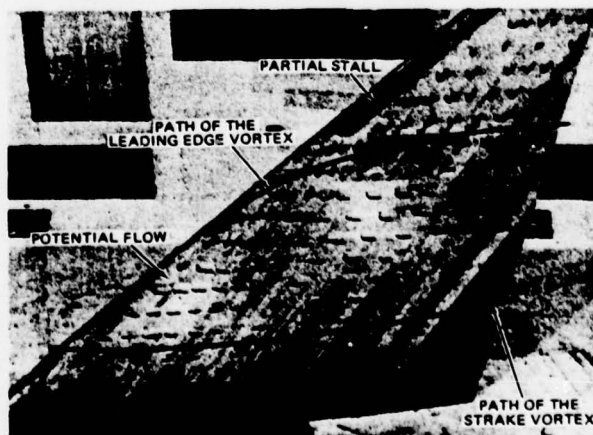
FIG. 18.   Surface Flow for Wing-Strake Configuration,
            α = 13.1 Degrees.

87
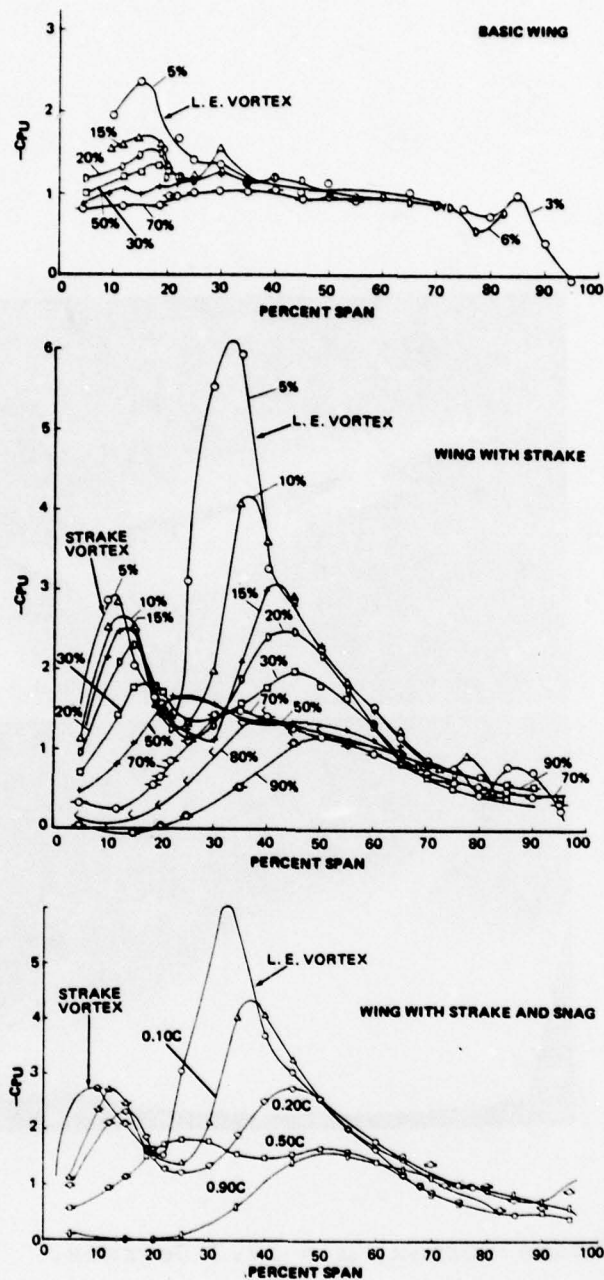
FIG. 19. Upper Surface Pressure Distributions,
α = 27.7 Degrees.

88
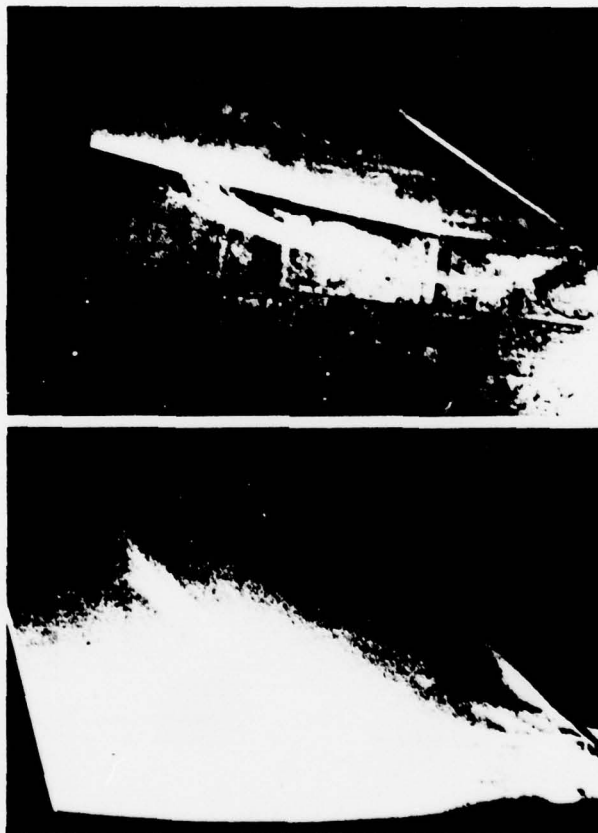
FIG. 20.   Strake Vortex, α = 27.7 Degrees.

89
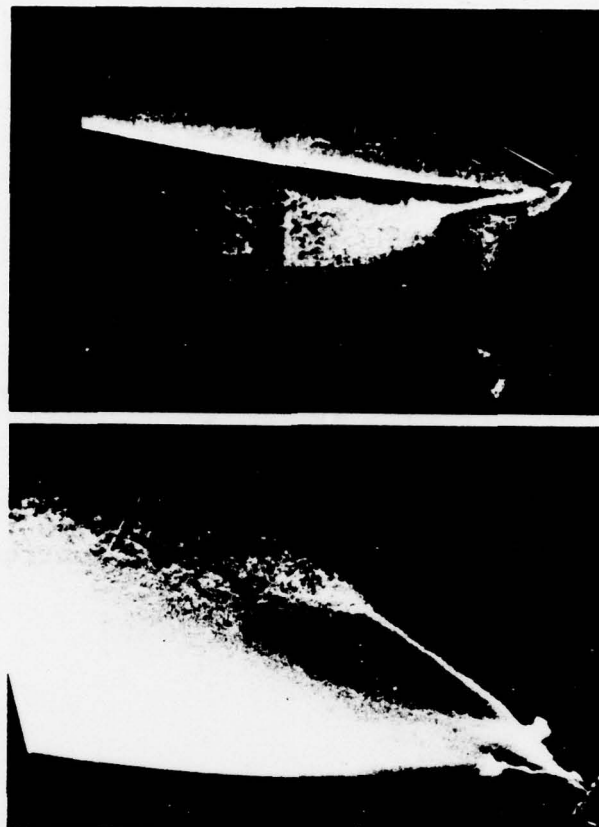
FIG. 21.   Leading Edge Vortex, α = 27.7 Degrees

FIG. 22.   Surface Flow for Wing-Strake Configuration,
α = 27.7 Degrees

90
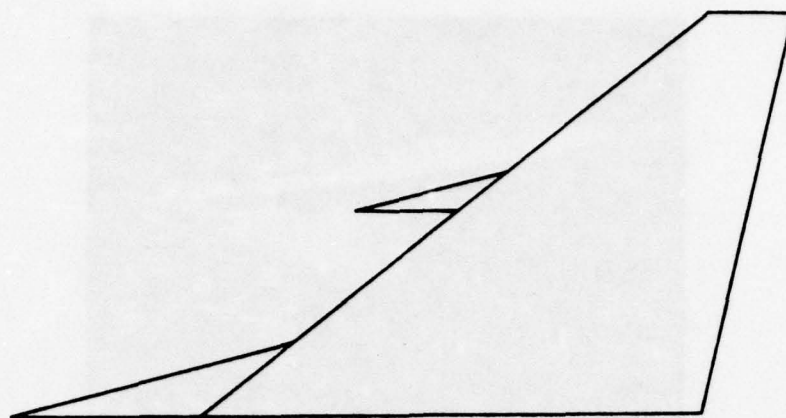
DOUBLE STRAKE (CONF 5A)

FIG. 23.   A Typical Multi-strake Configuration.
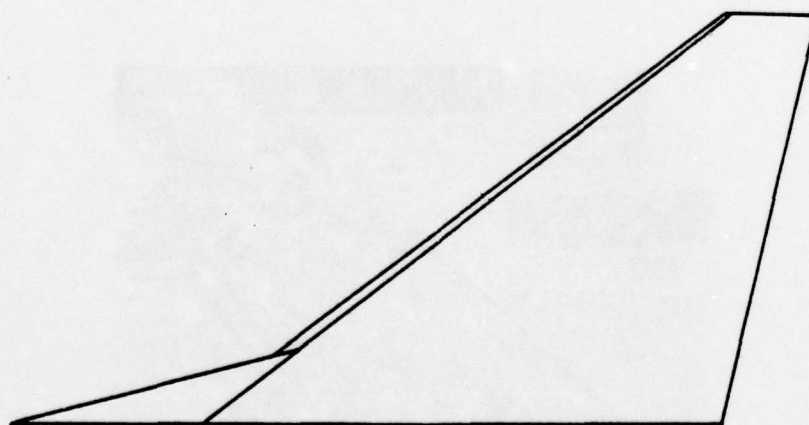
FIG. 24.   A Configuration with a Single Strake and a
Separator Plate.
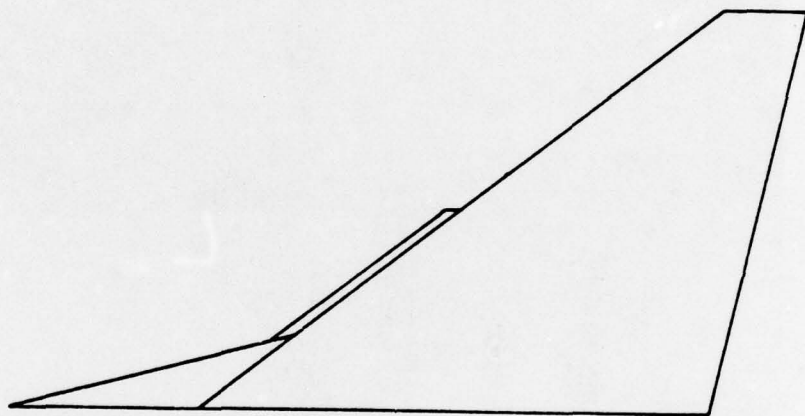
FIG. 25. Combination of the Basic Wing with a Root
Strake and a Partial Separator Plate with
Swept Outboard Edge.
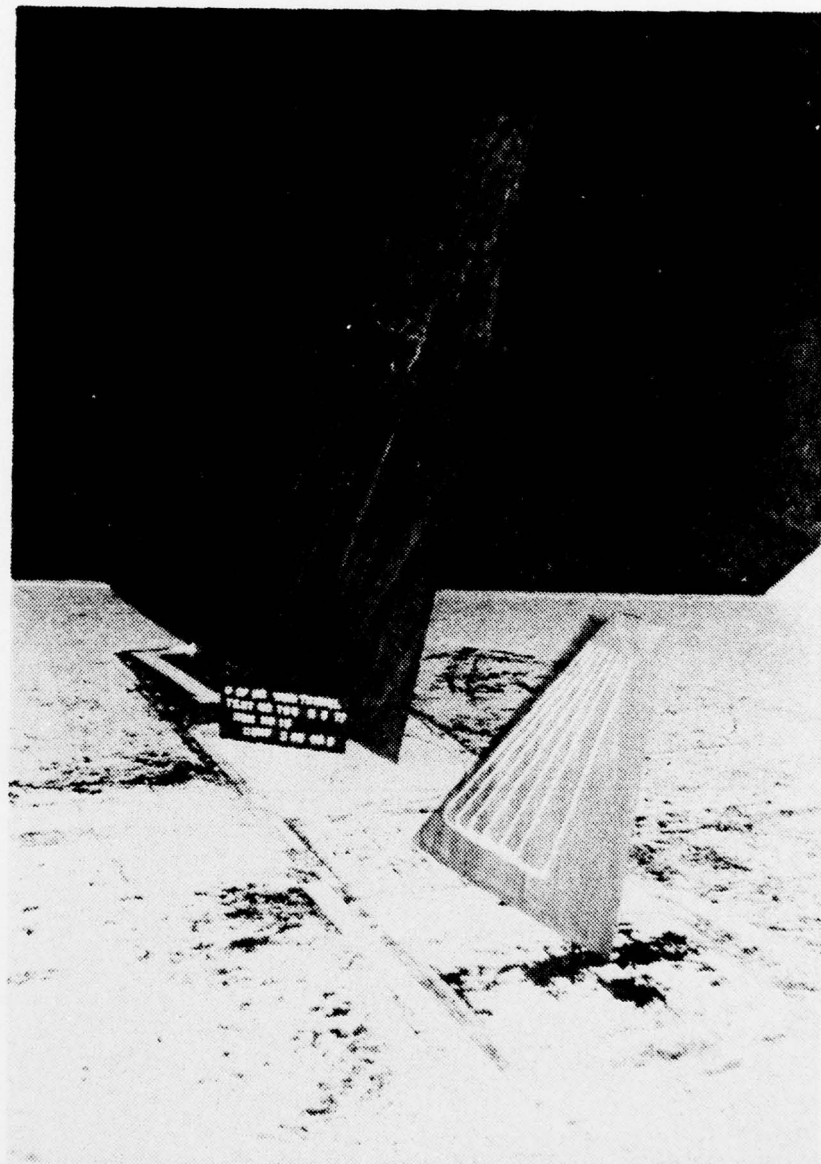
FIG. 26. Picture of Wing Tail Model in the Wind Tunnel.
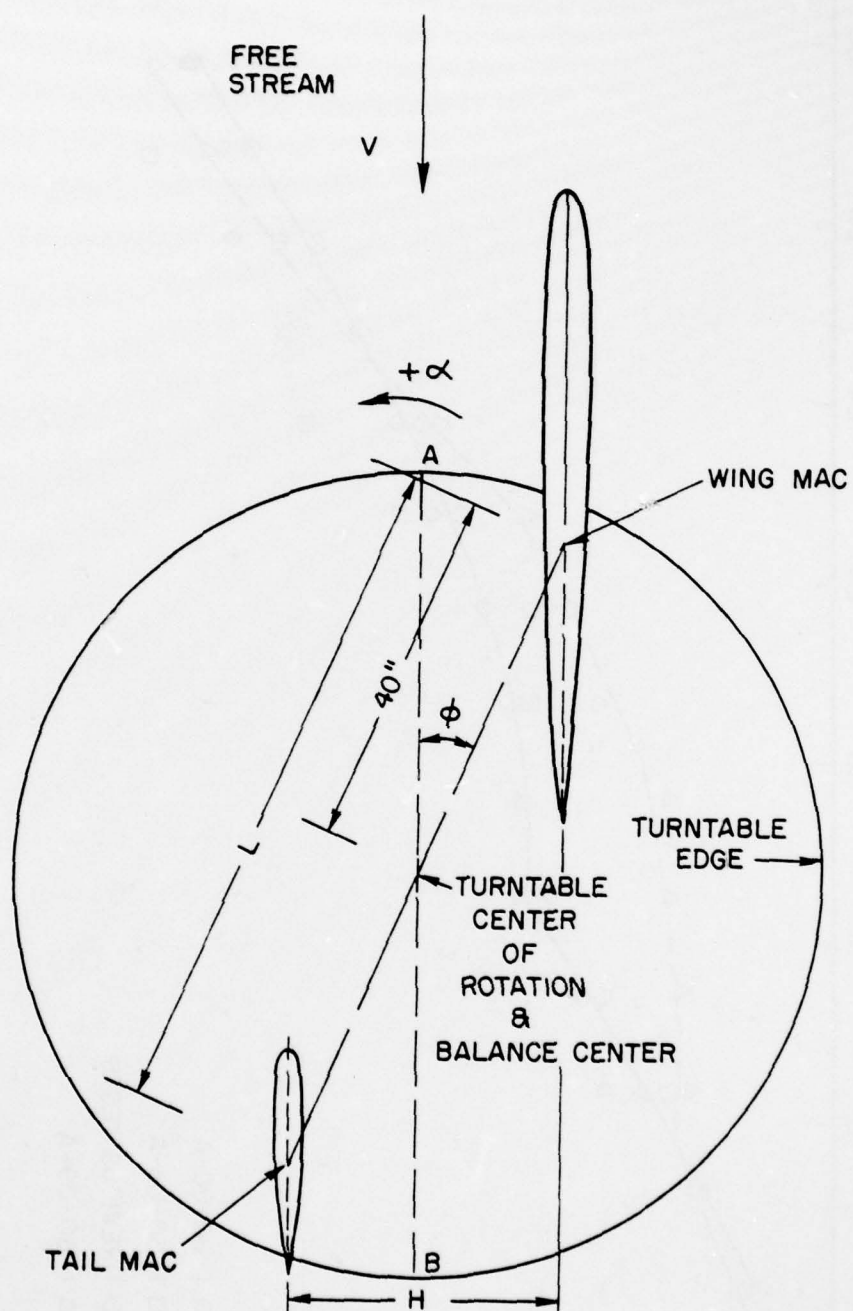
FIG. 27.   Model Arrangement on the Wind Tunnel Turntable.

94
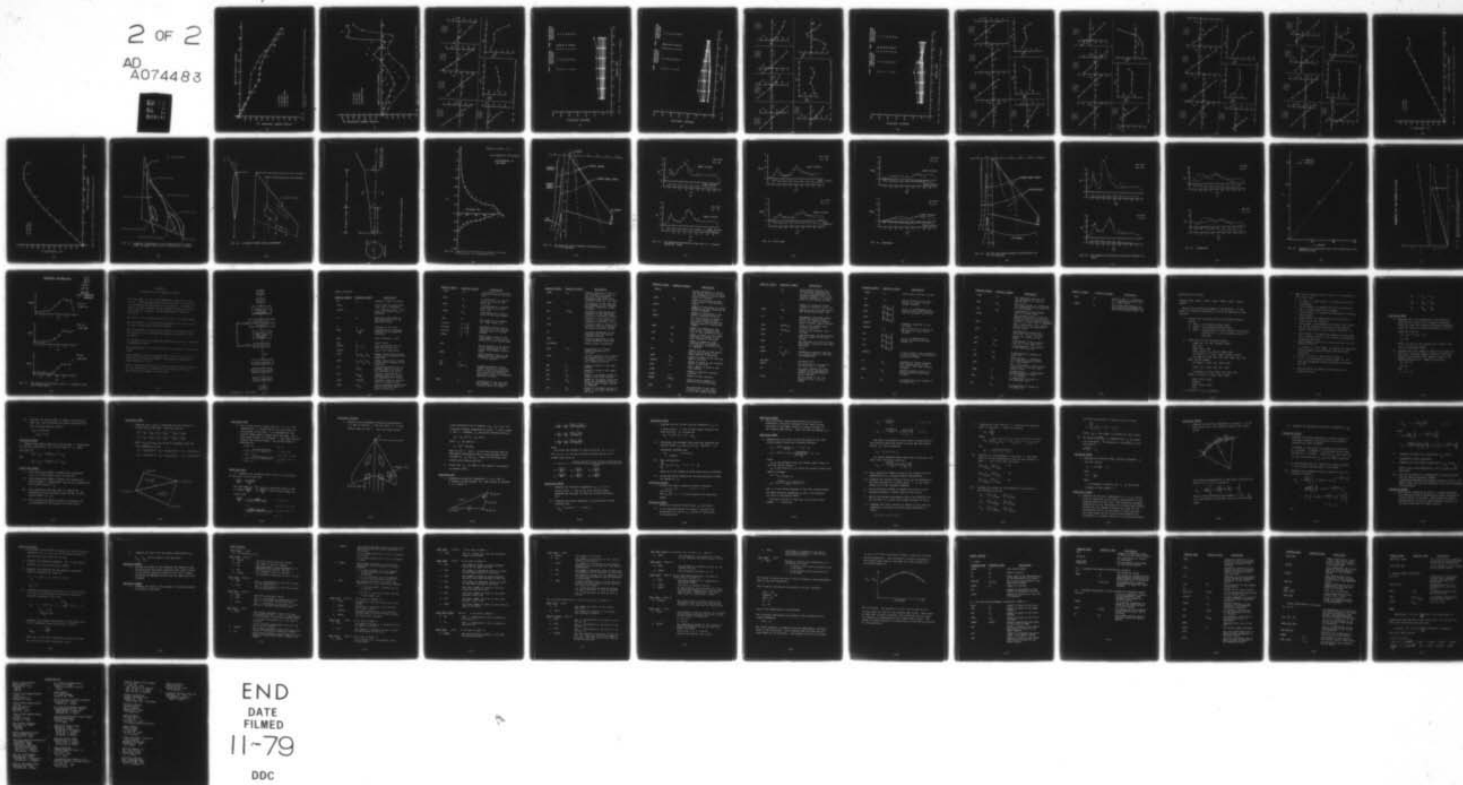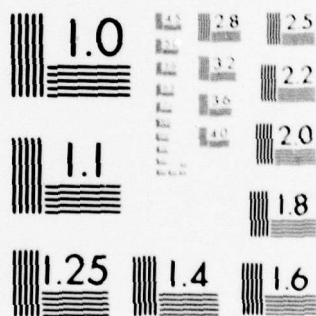
MICROCOPY RESOLUTION TEST CHART
NATIONAL BUREAU OF STANDARDS-1963-A
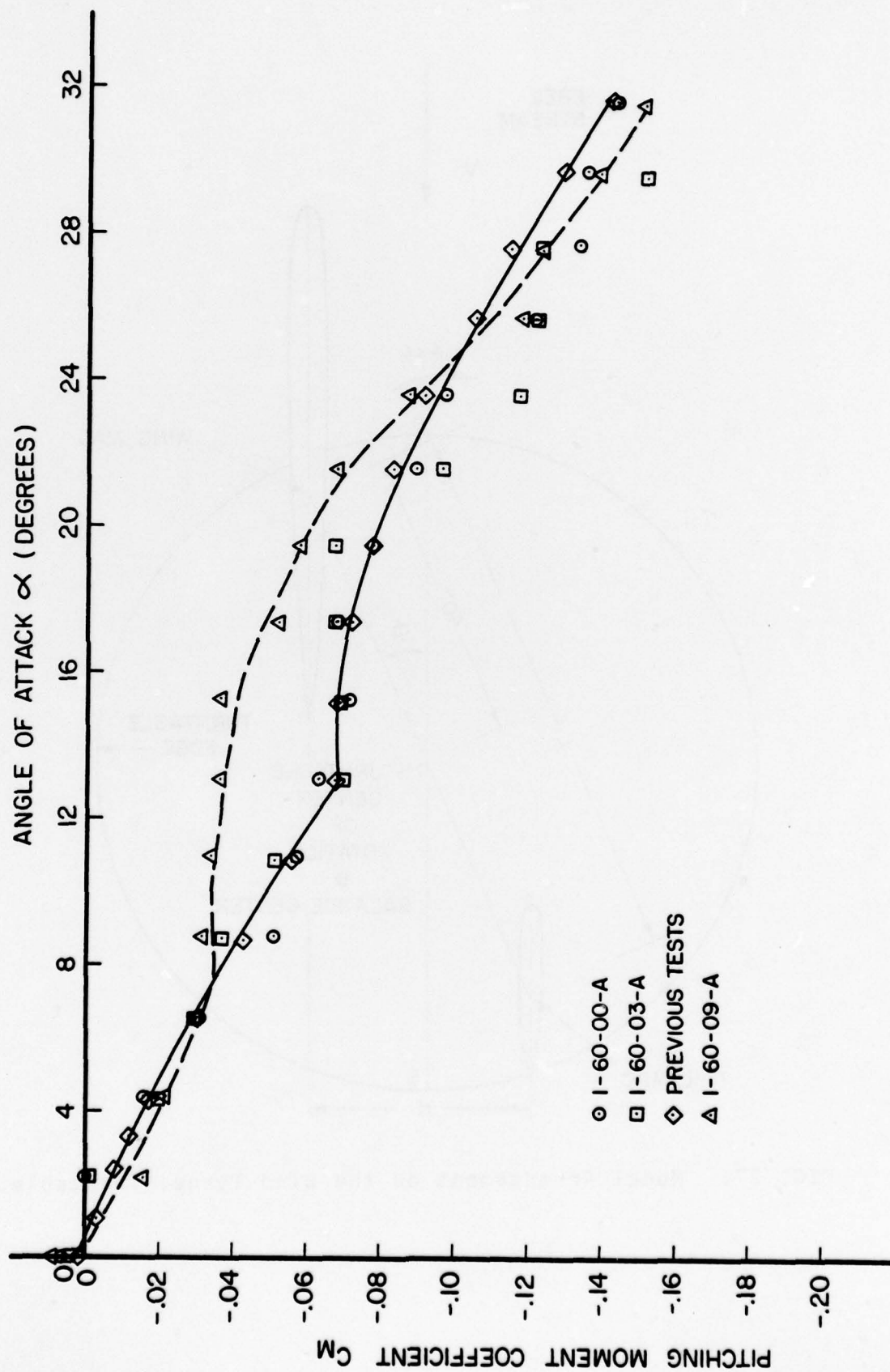
FIG. 28. Effect of Basic Wing Location in the Wind Tunnel on the Pitching Moment Coefficient.
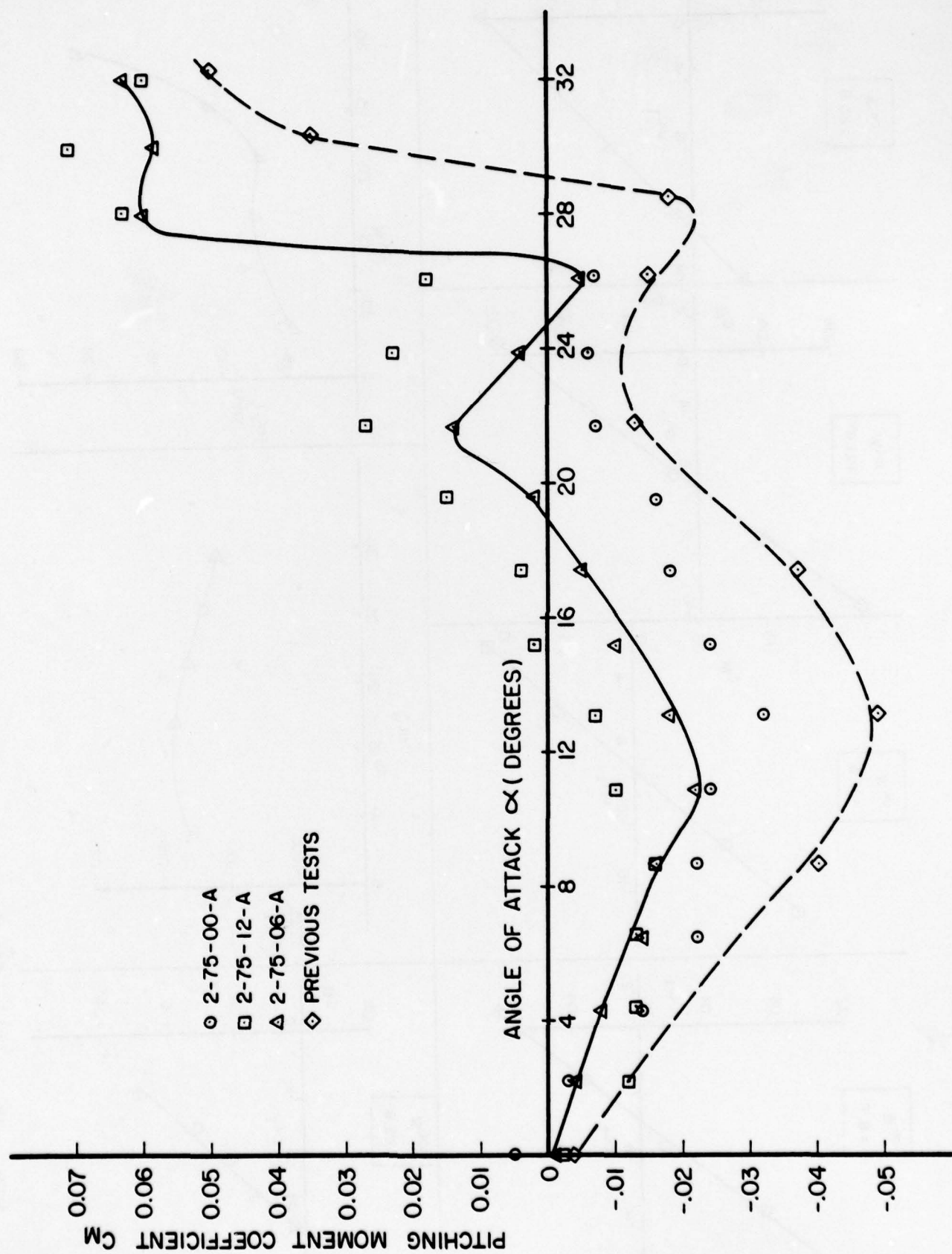
FIG. 29. Effect of Wing-Strake Model Location in the Wind Tunnel on the Pitching Moment Coefficient.
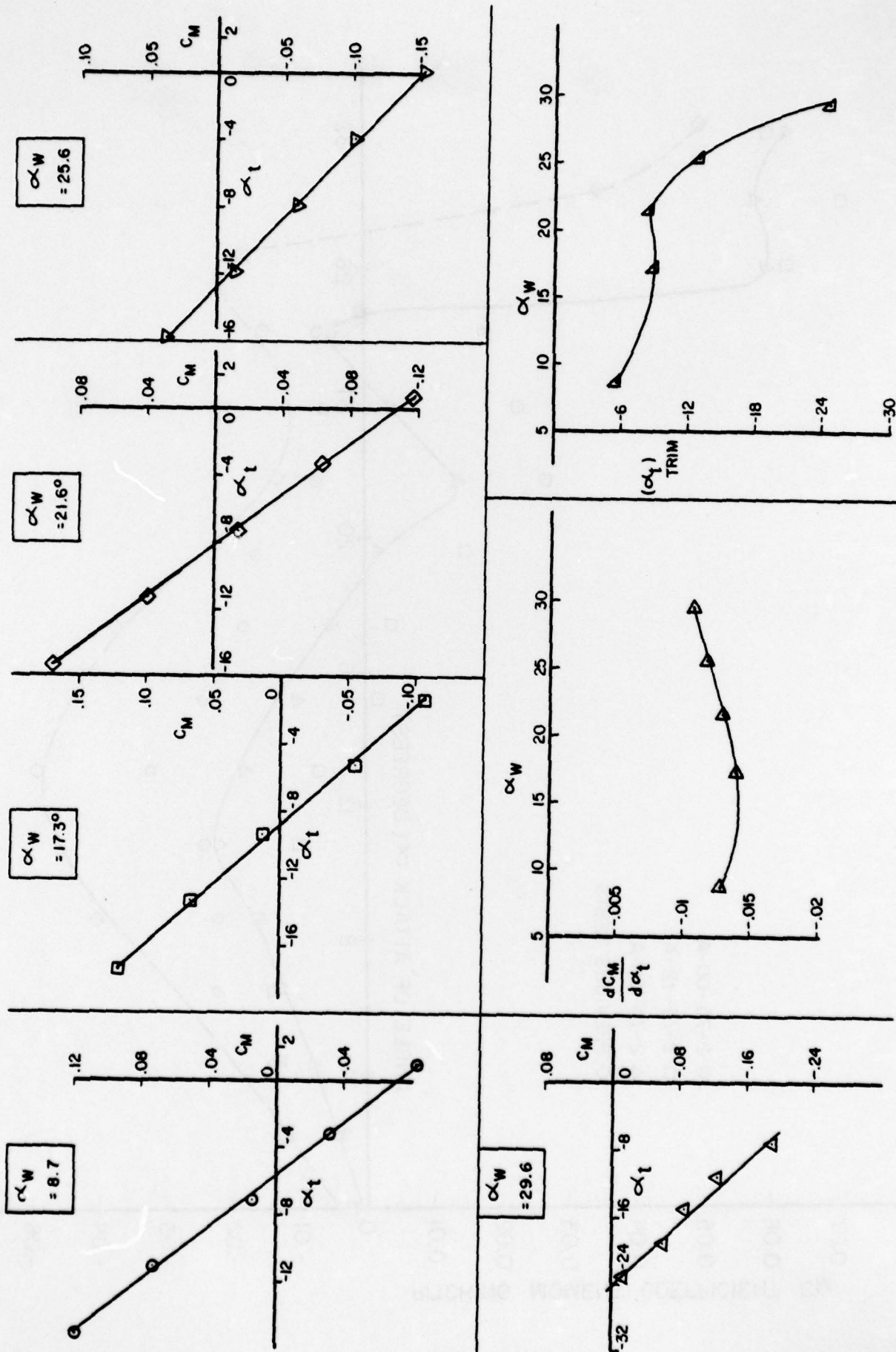
96

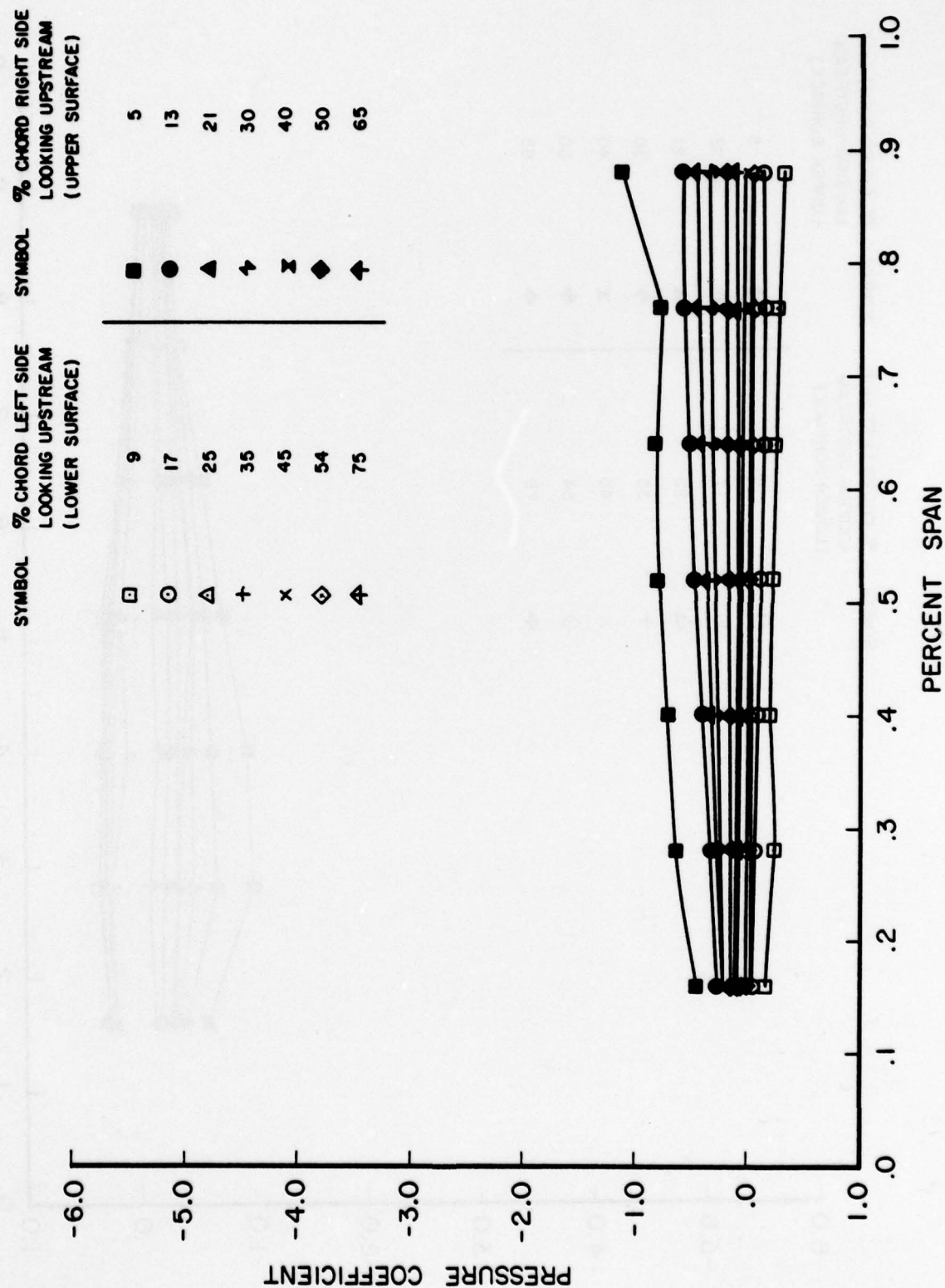FIG. 30. Tail Effectiveness of Configuration 1-75-06B.

97

FIG. 31. Tail Pressure Distributions at Trim for α_w = 8.7 Degrees.
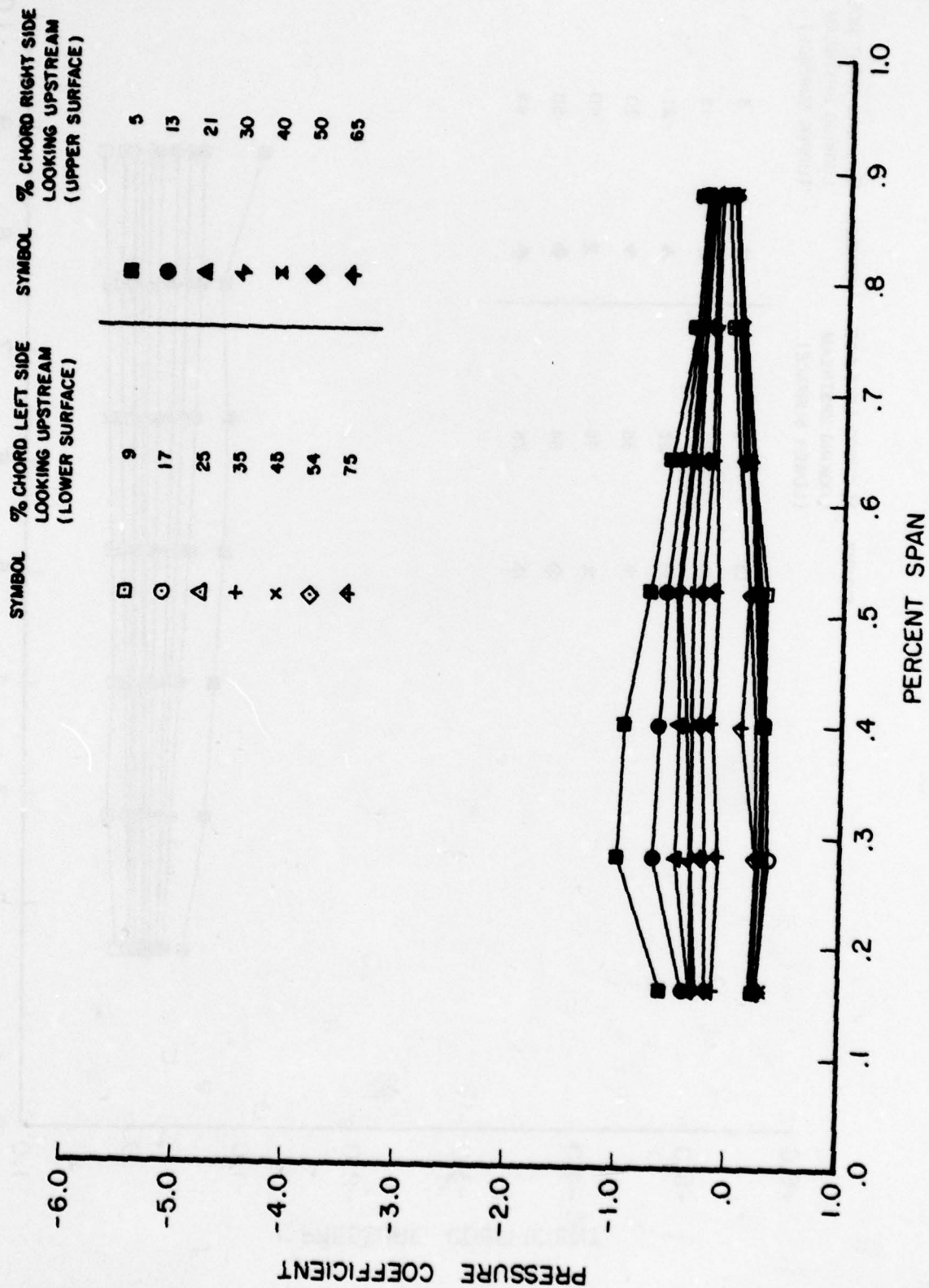
98

FIG. 32. Tail Pressure Distributions at Trim for α_w = 29.7 Degrees.
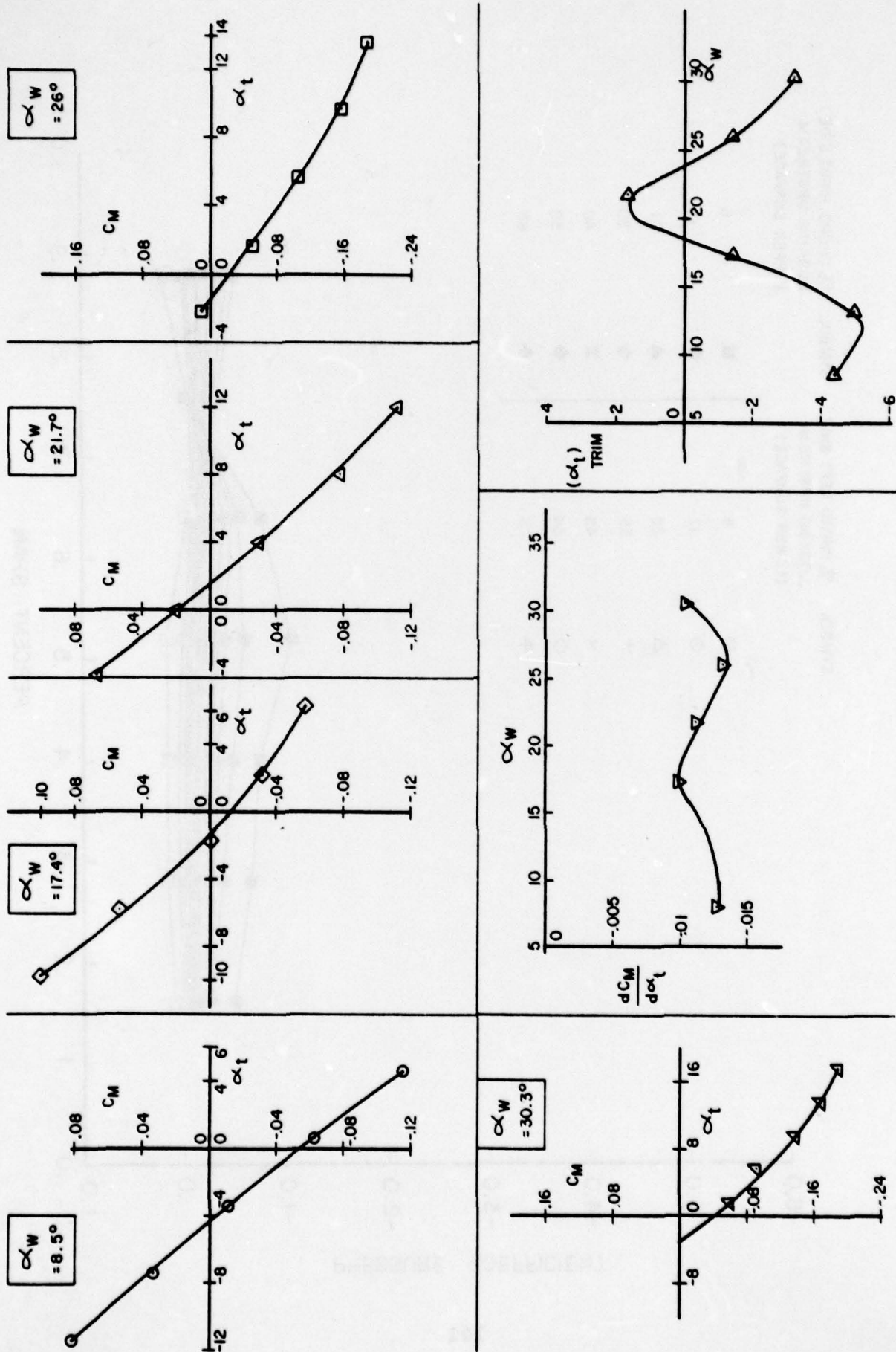
99

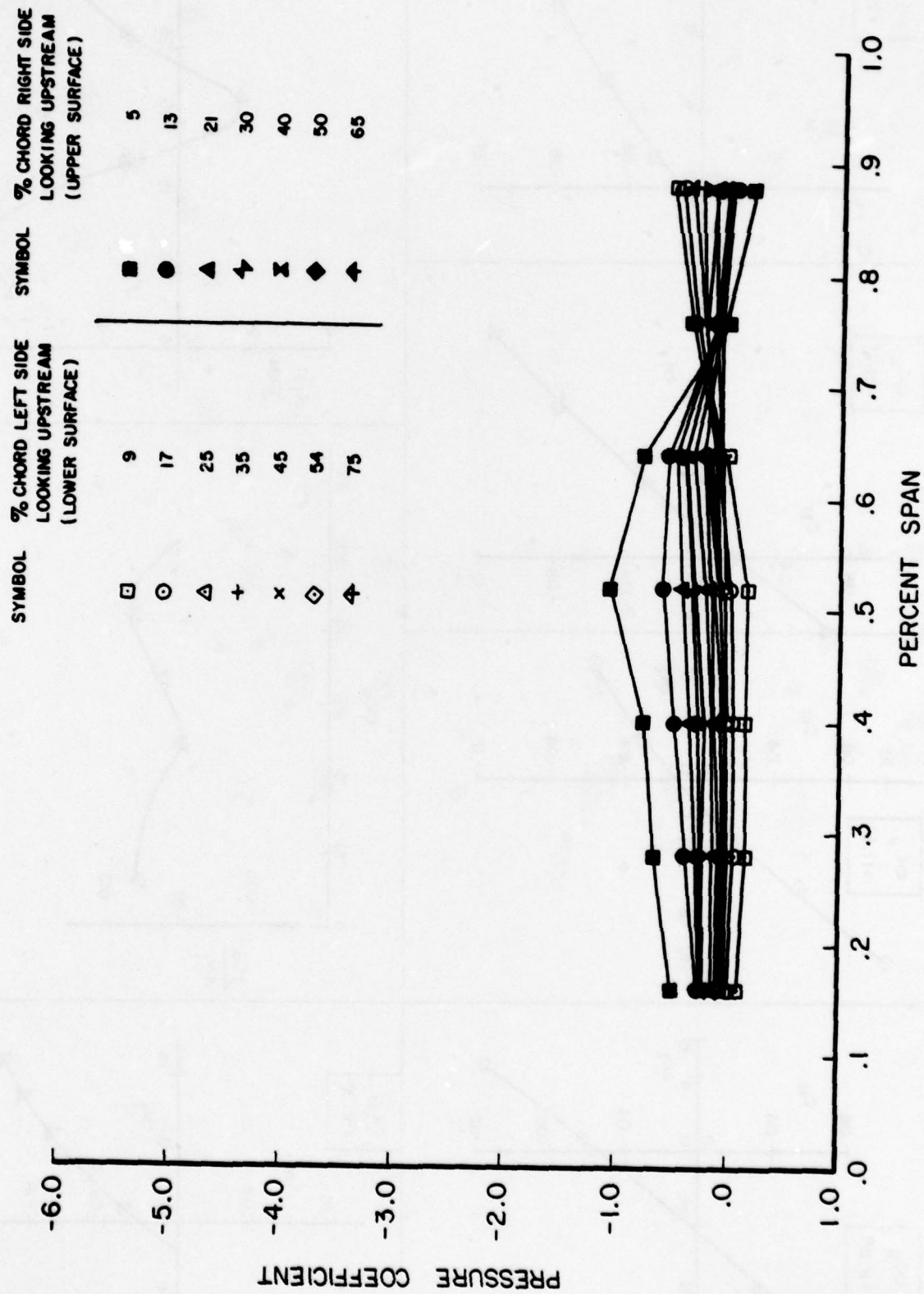FIG. 33. Tail Effectiveness of Configuration 2-75-06B.

FIG. 34. Tail Pressure Distributions at Trim for α_w = 13.1 Degrees.
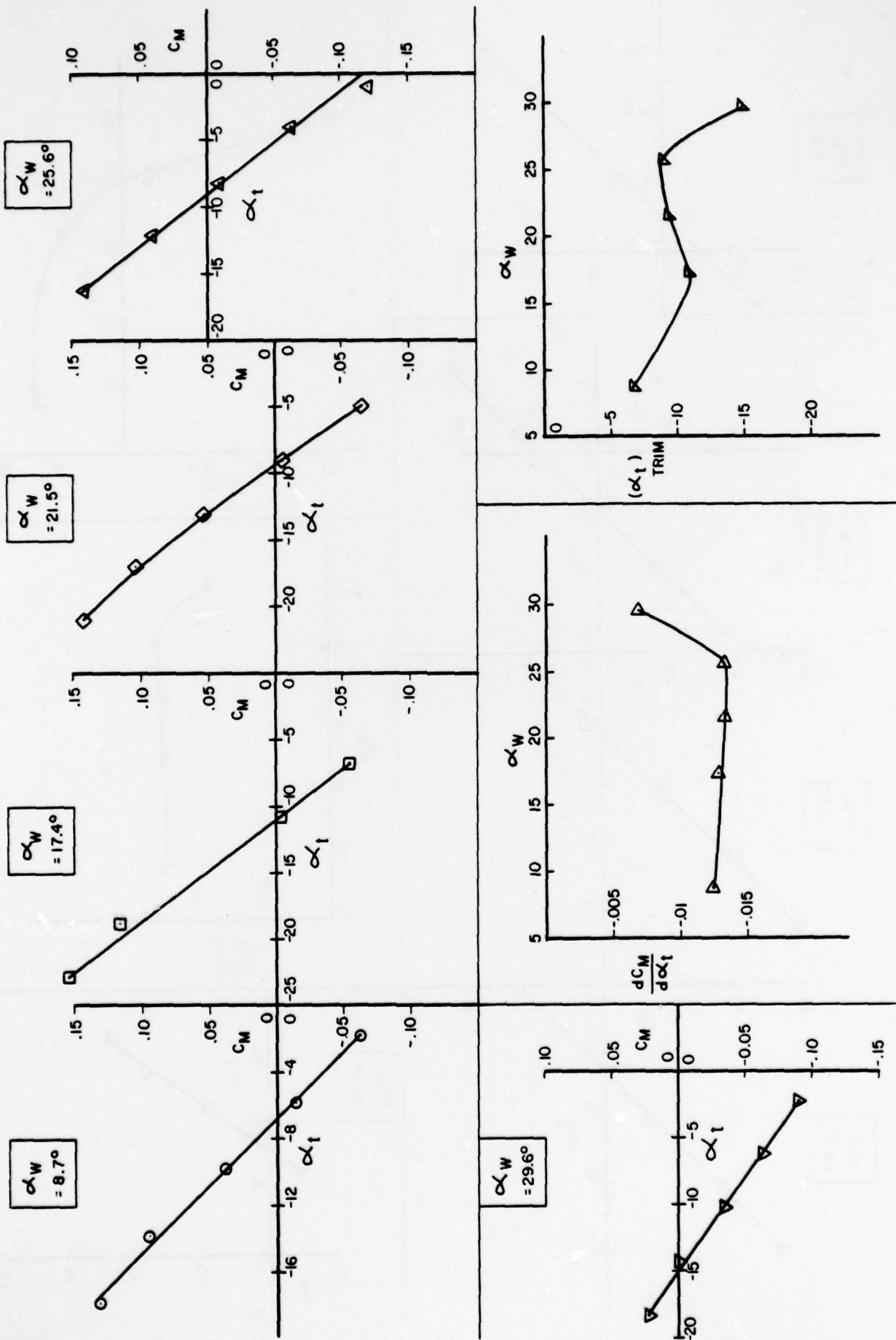
101

FIG. 35. Tail Effectiveness of Configuration 1-75-12B.

102
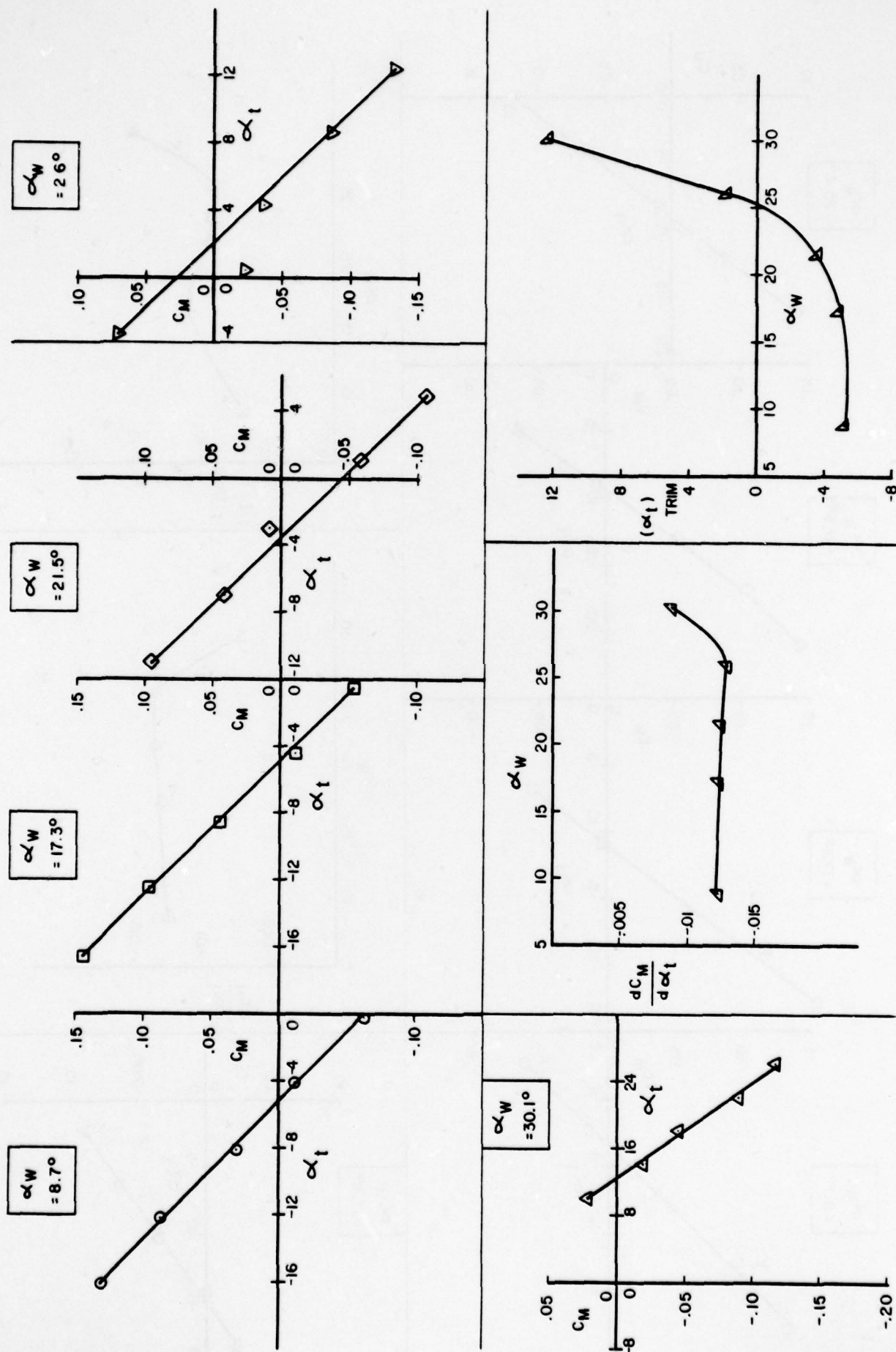
FIG. 36. Tail Effectiveness of Configuration 2-75-12B.
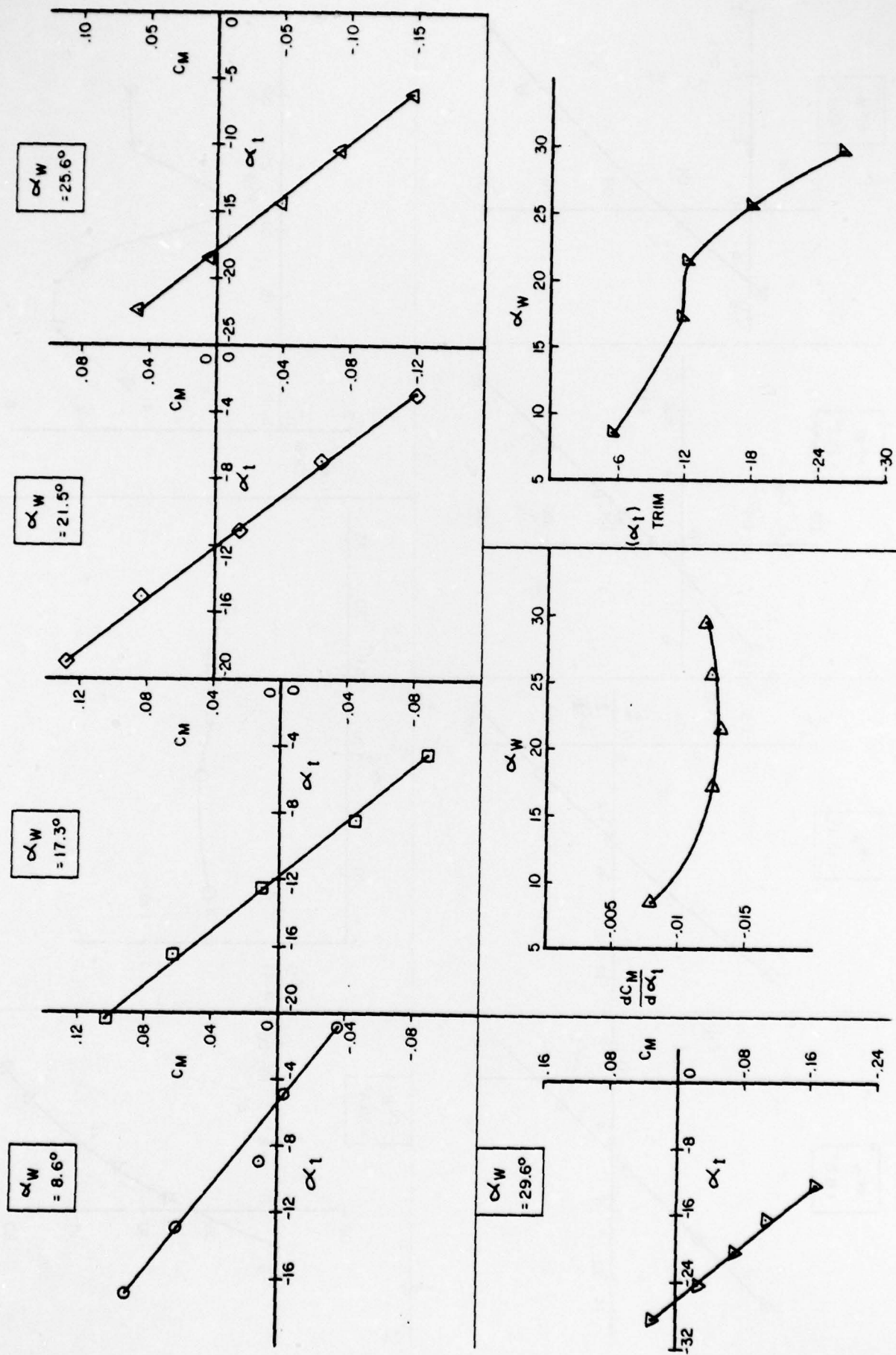
FIG. 37. Tail Effectiveness of Configuration 1-60-03B.

104
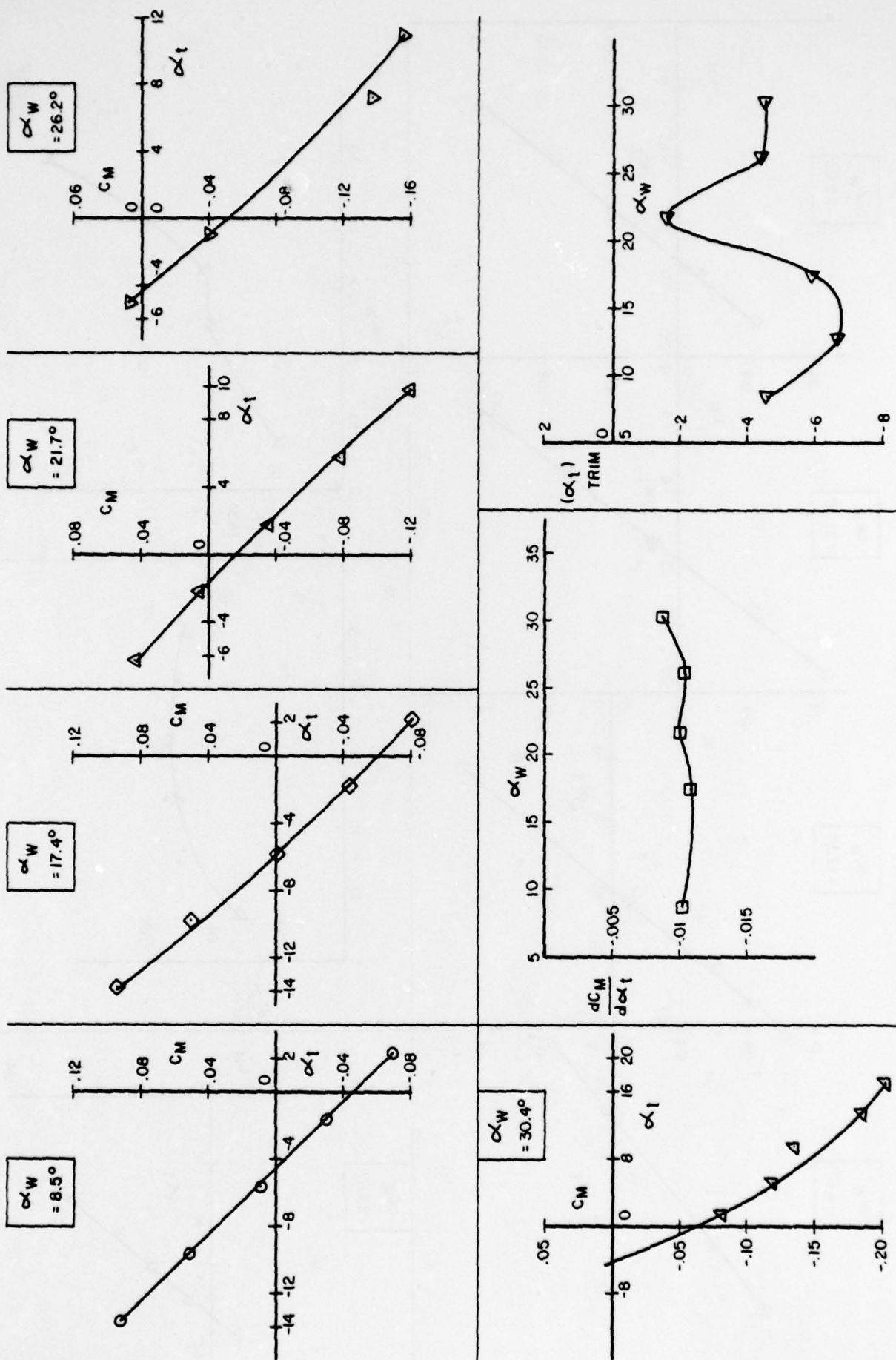
FIG. 38. Tail Effectiveness of Configuration 2-60-03B.

105
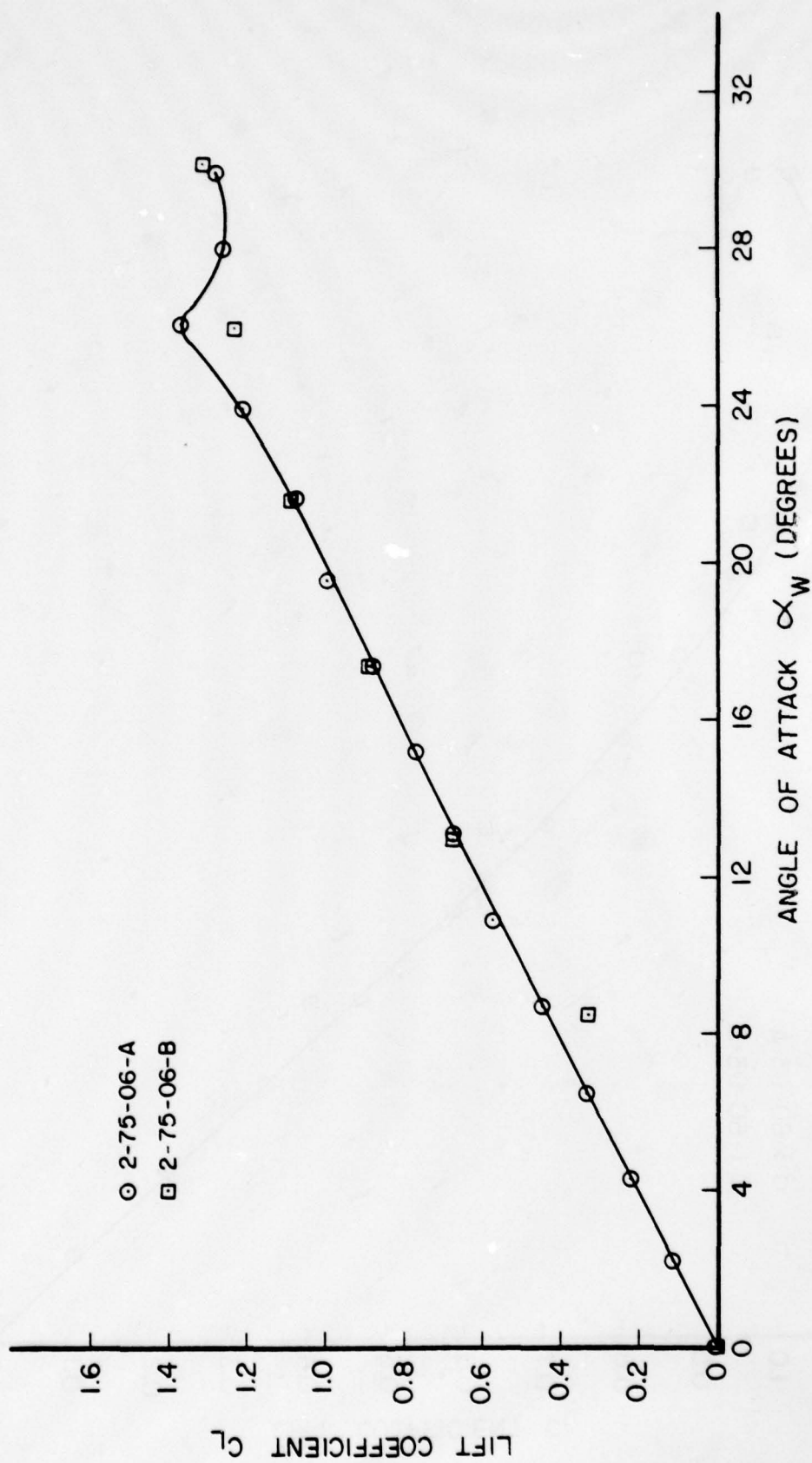
FIG. 39. C_L vs. Angle of Attack of Wing-Strake Configuration at Trim.
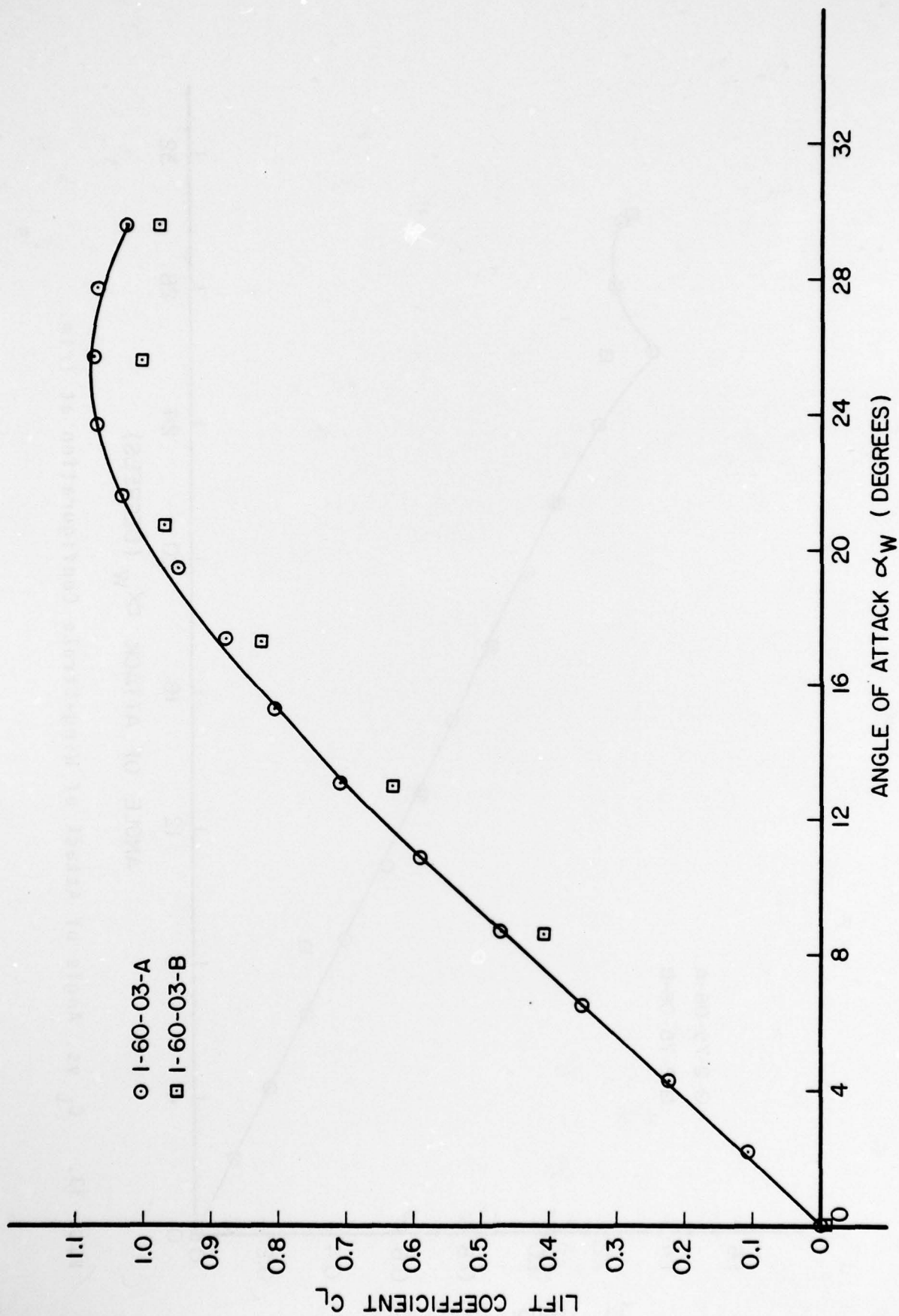
FIG. 40. C_L vs. Angle of Attack of Wing Configurations at Trim.

107
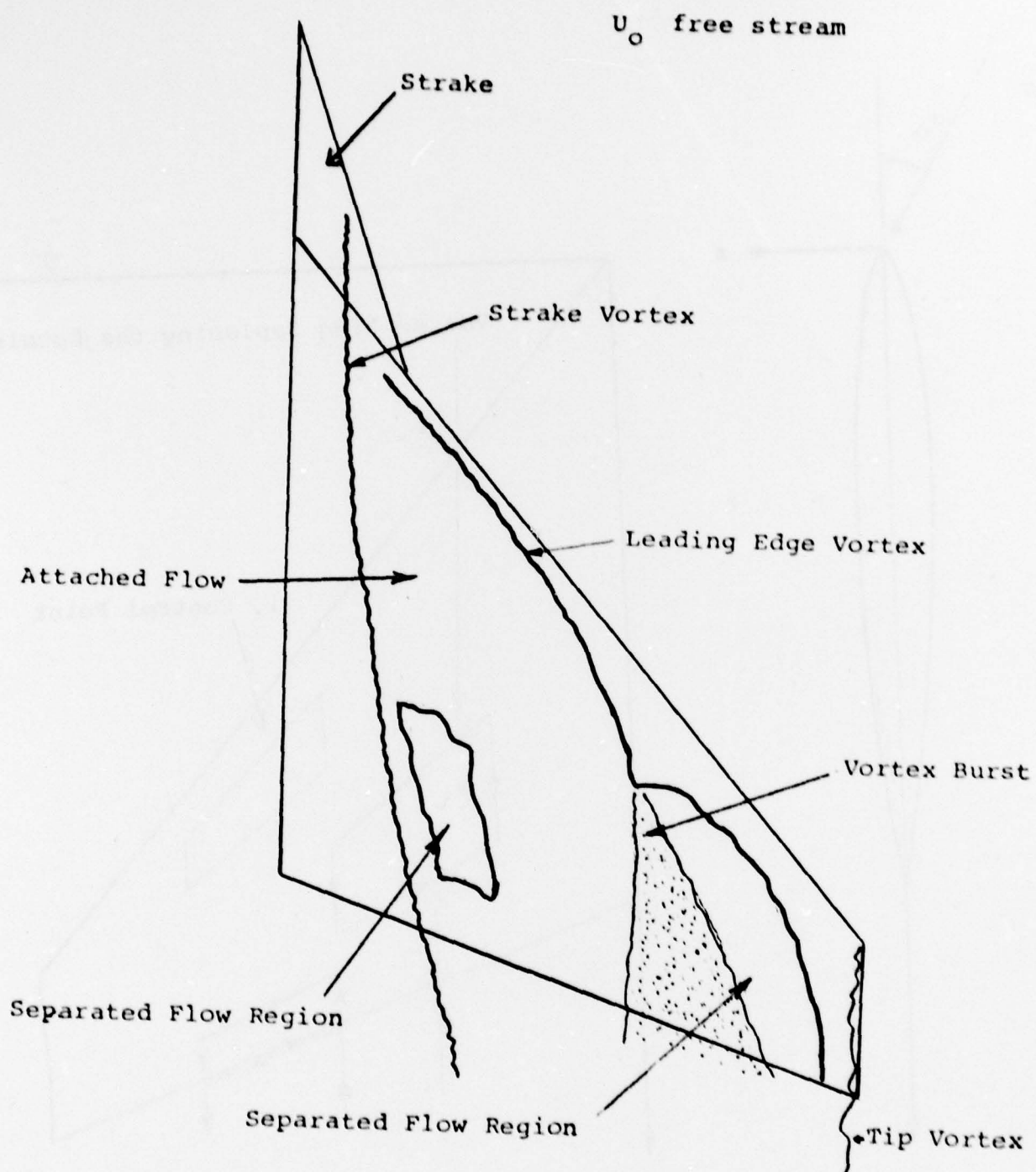
FIG. 41. Schematic Illustration of Flow Features Over a Highly
          Swept Low Aspect Ratio Wing at High Angles of Attack.
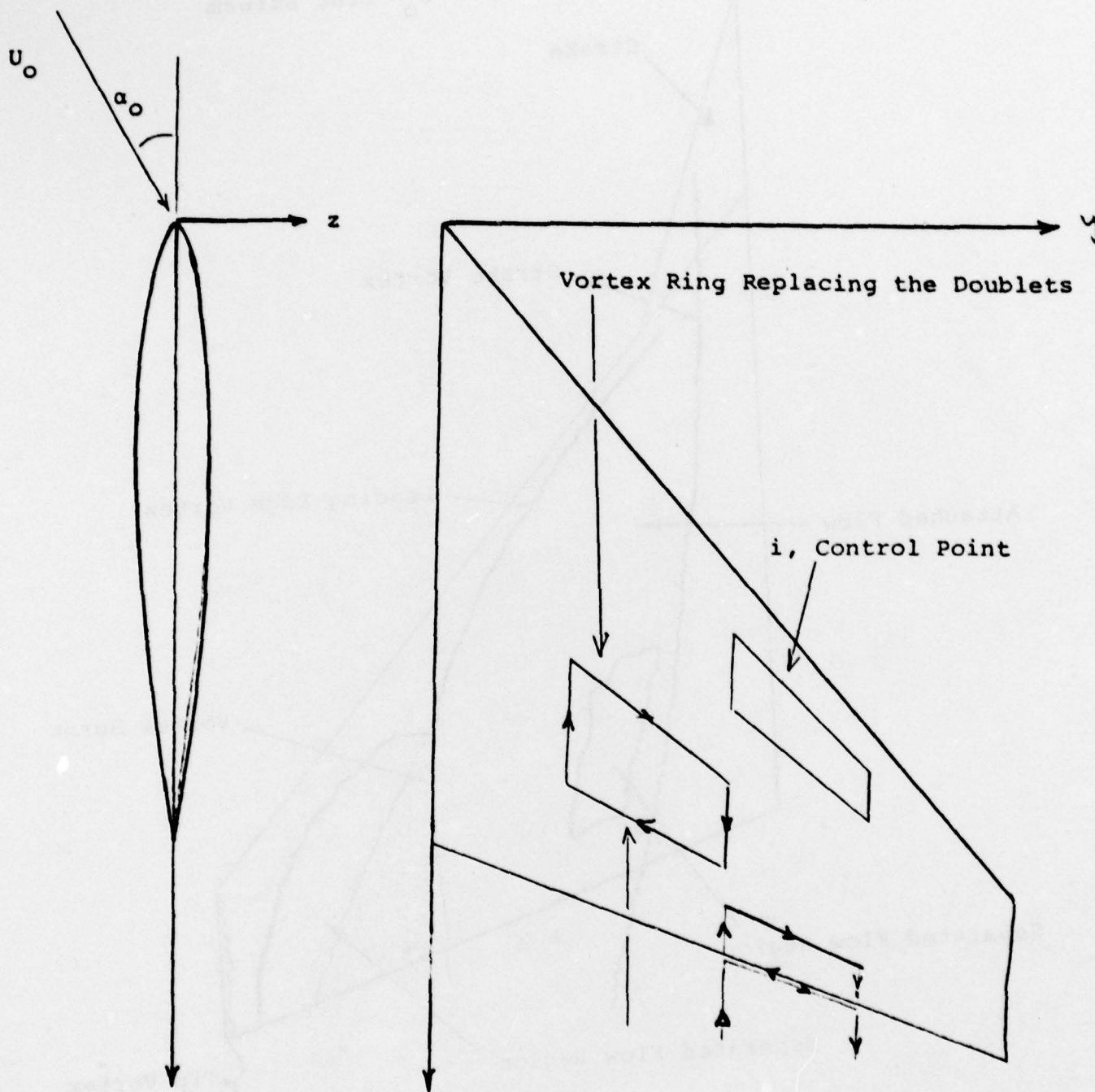
FIG. 42. A Typical Doublet Panel Arrangement.

109
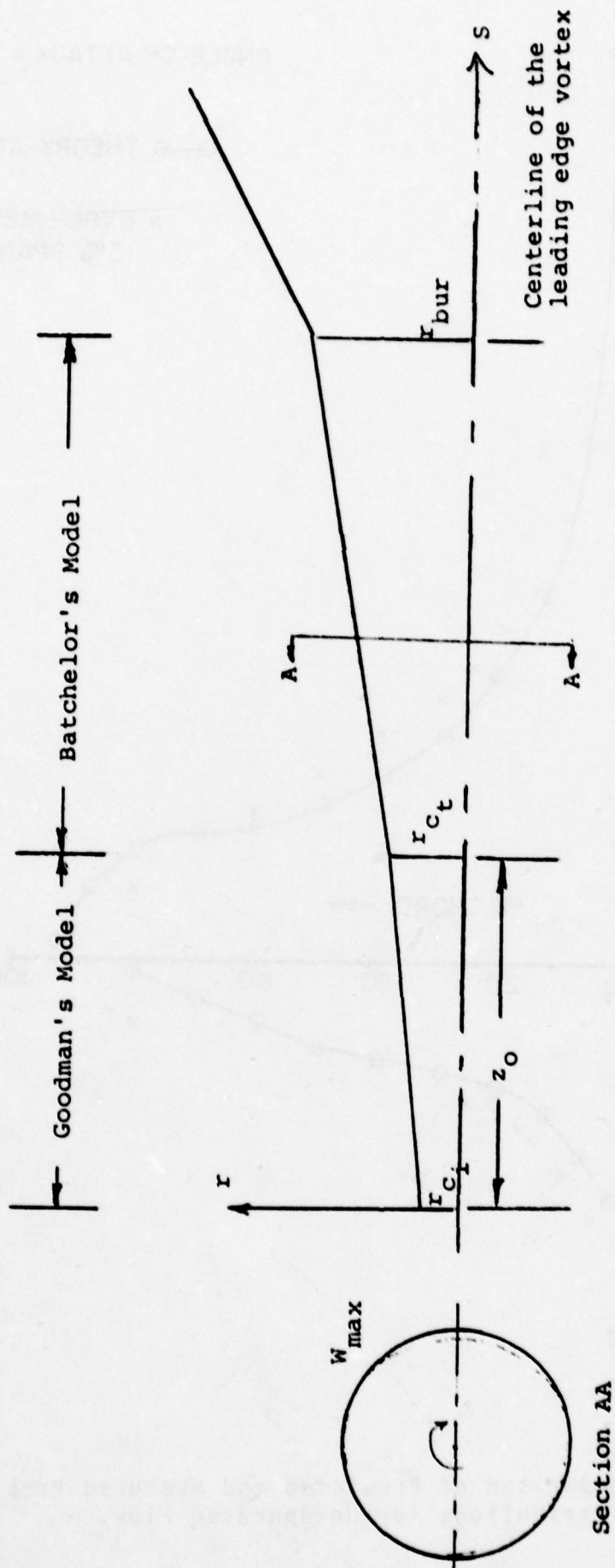
FIG. 43. The Vortex Core Geometry and Models.
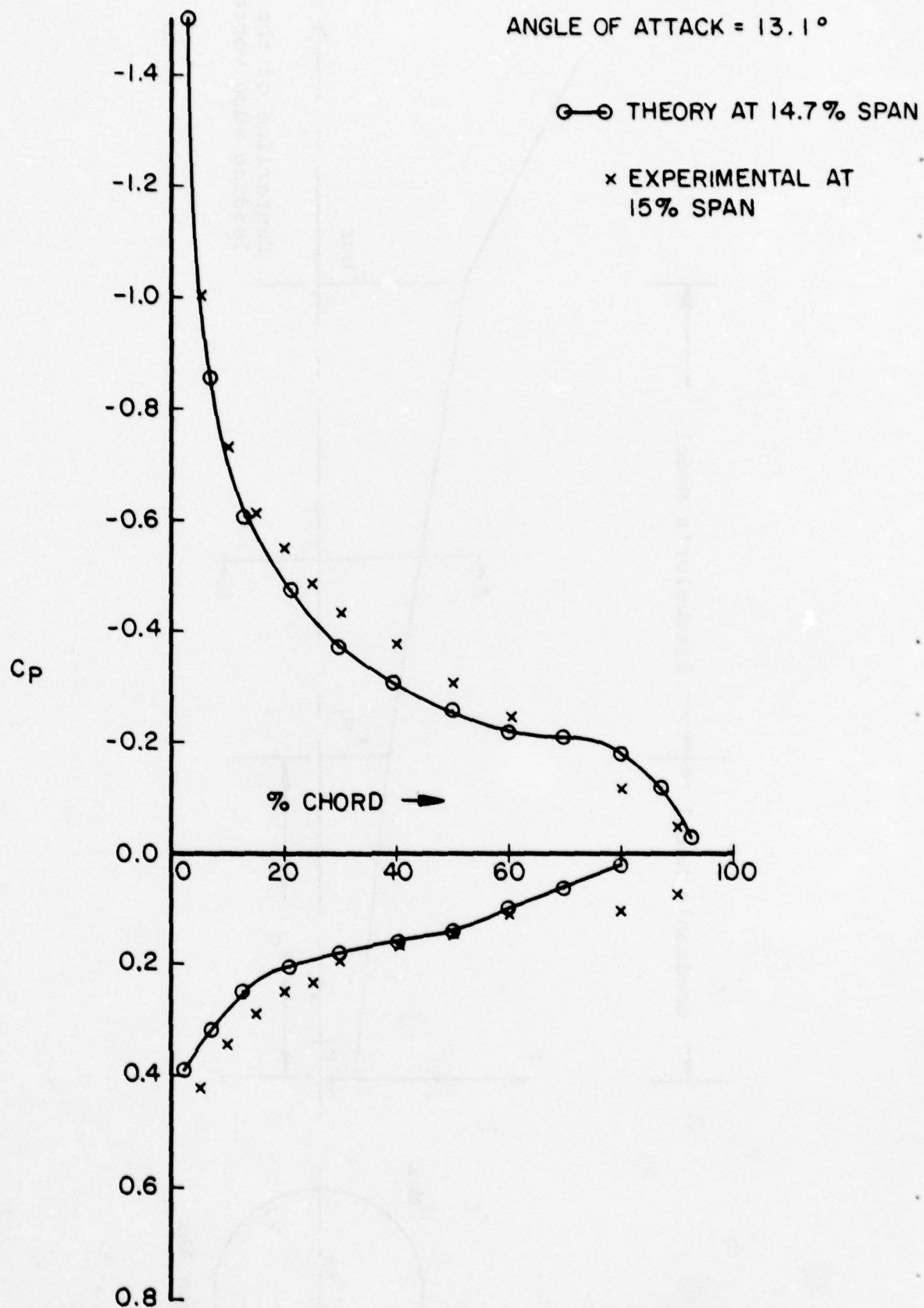
FIG. 44. Comparison of Predicted and Measured Pressure
Distributions for Unseparated Flow.

111
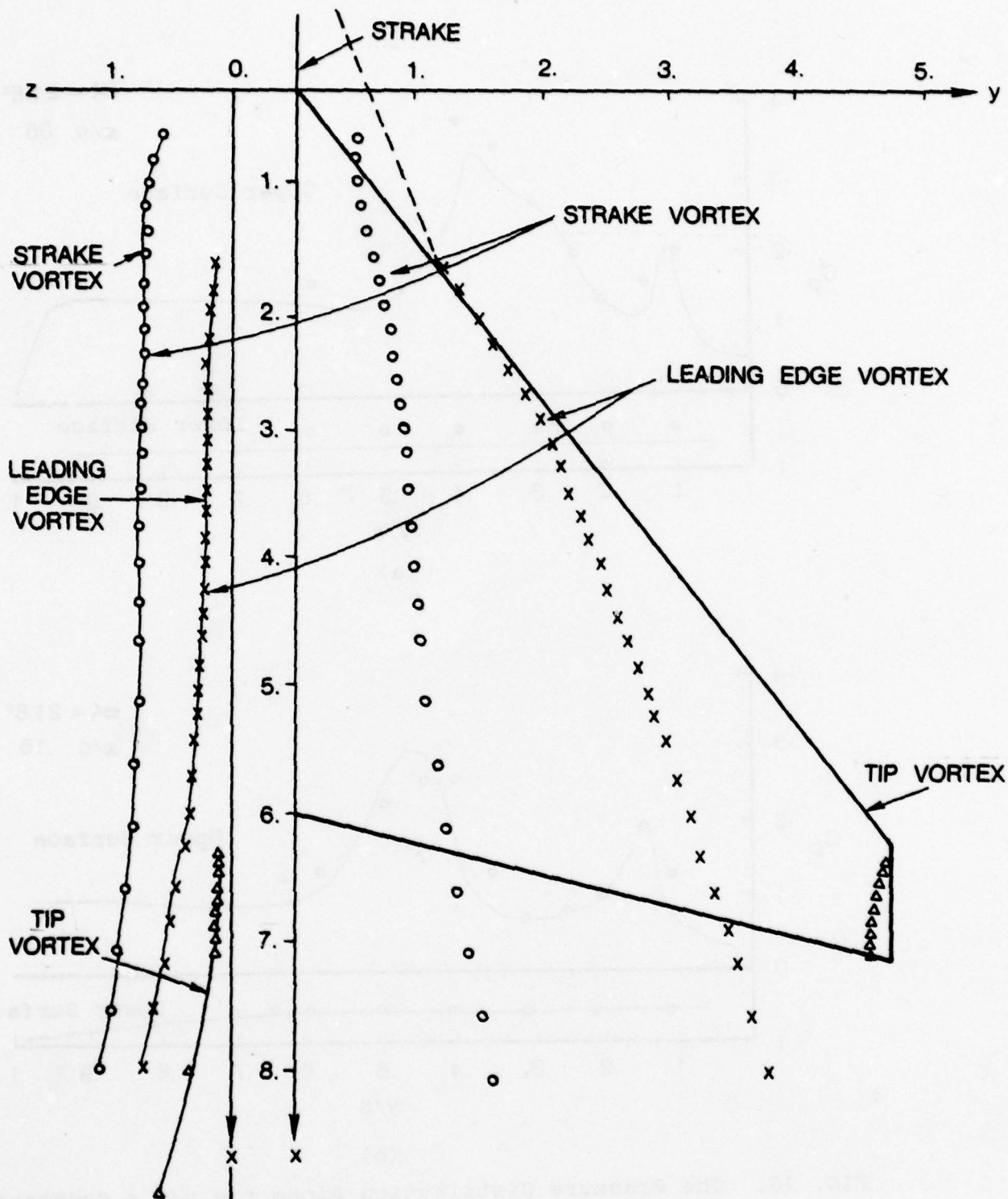
FIG. 45. The Wing and Vortex Geometry Configuration for α = 21.6 Degrees.

112
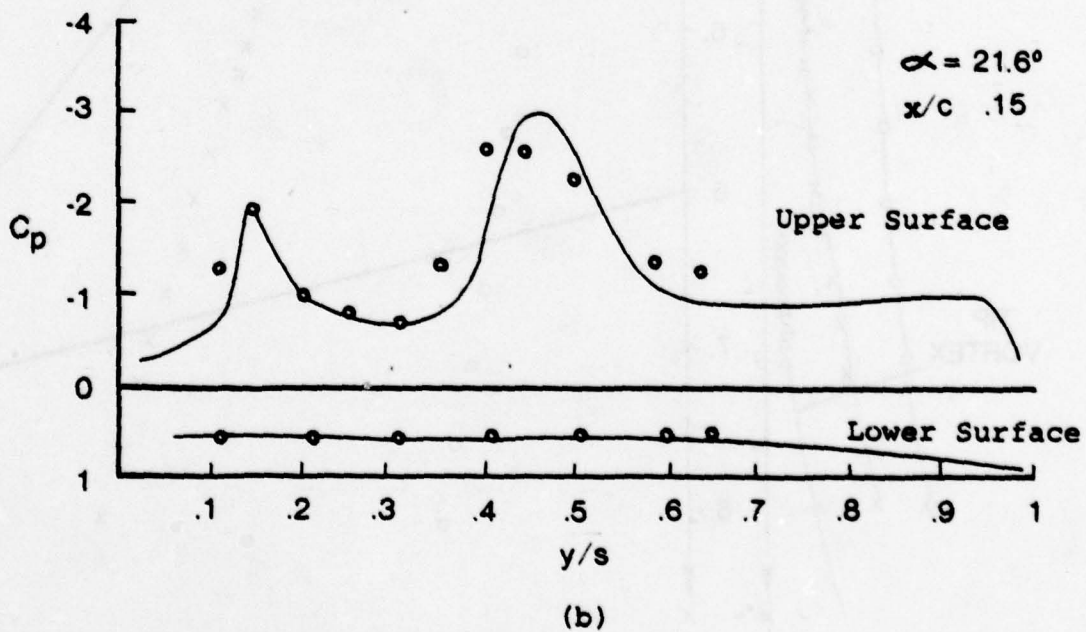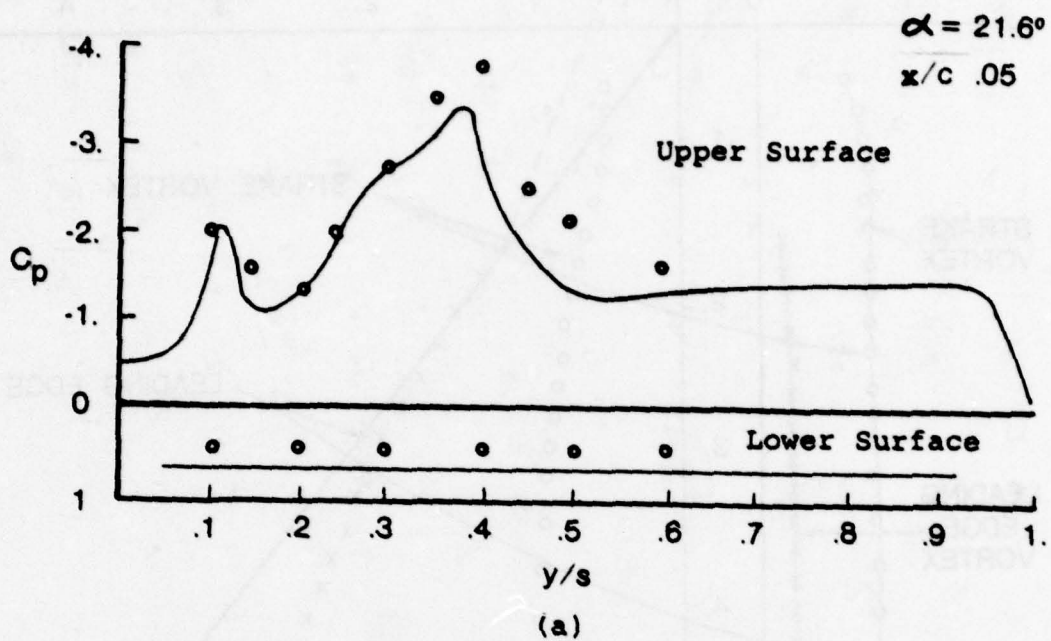
FIG. 46. The Pressure Distribution Along the n/c = constant
          (spanwise) lines.

113

FIG. 46. (Continued)

114
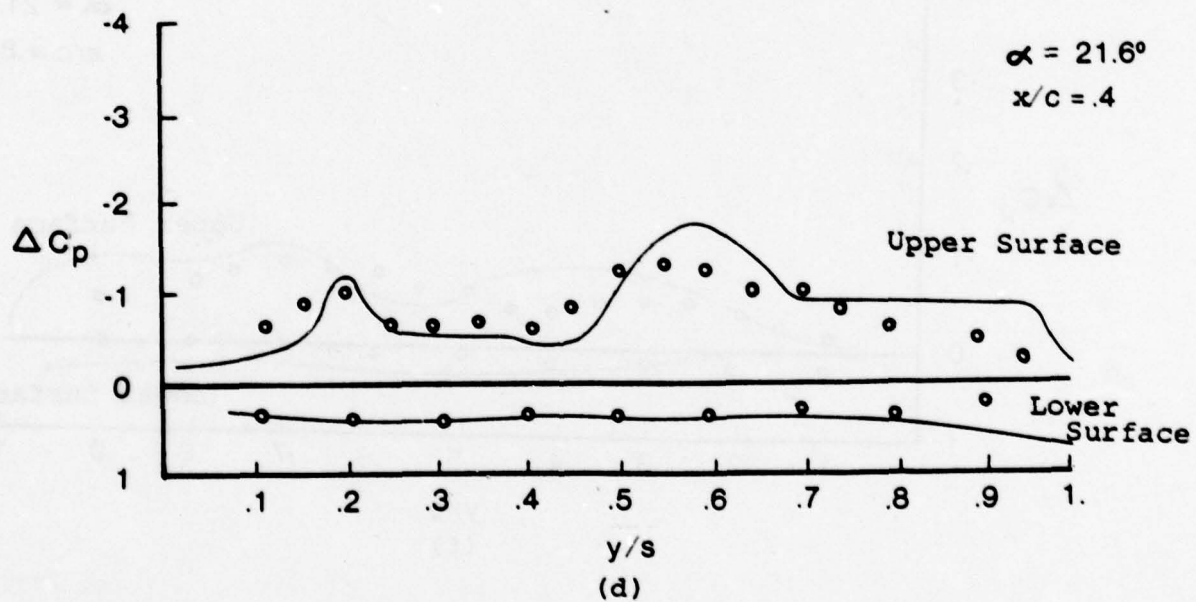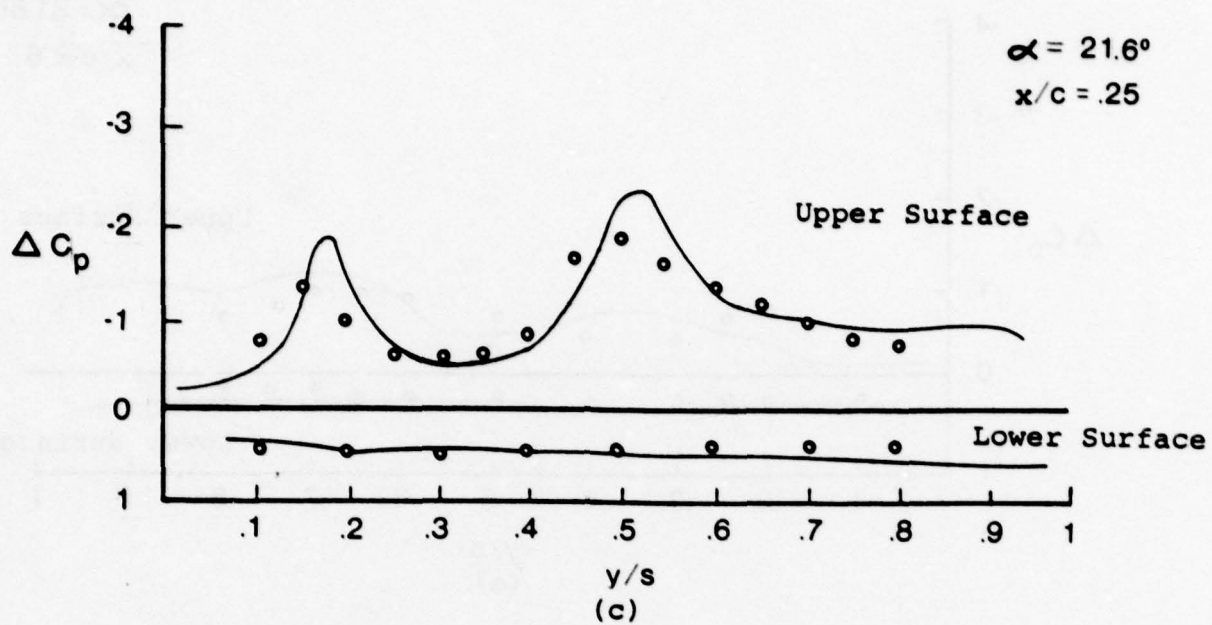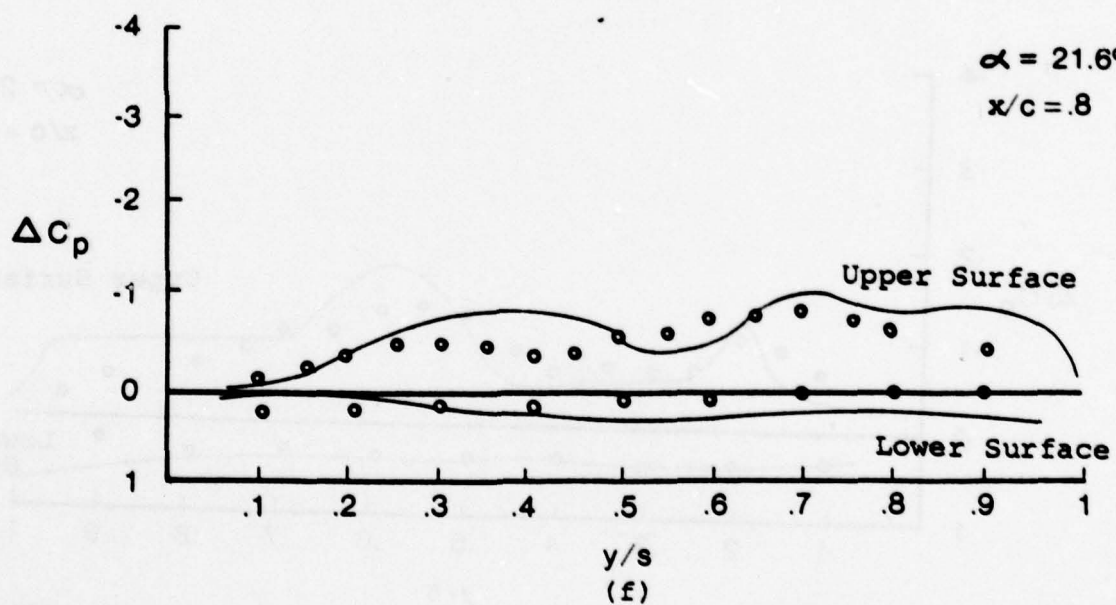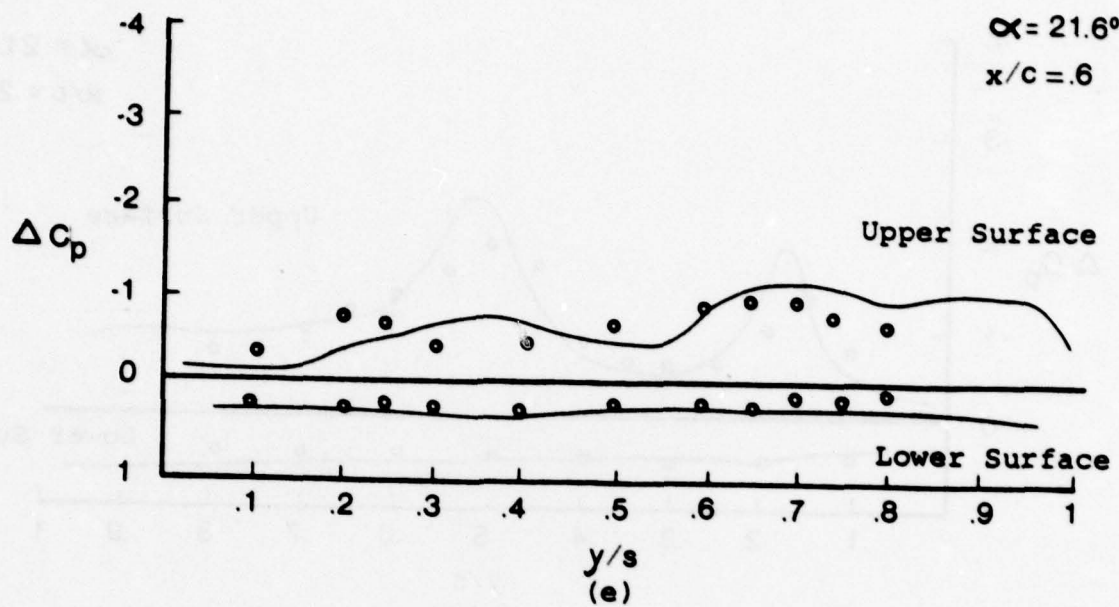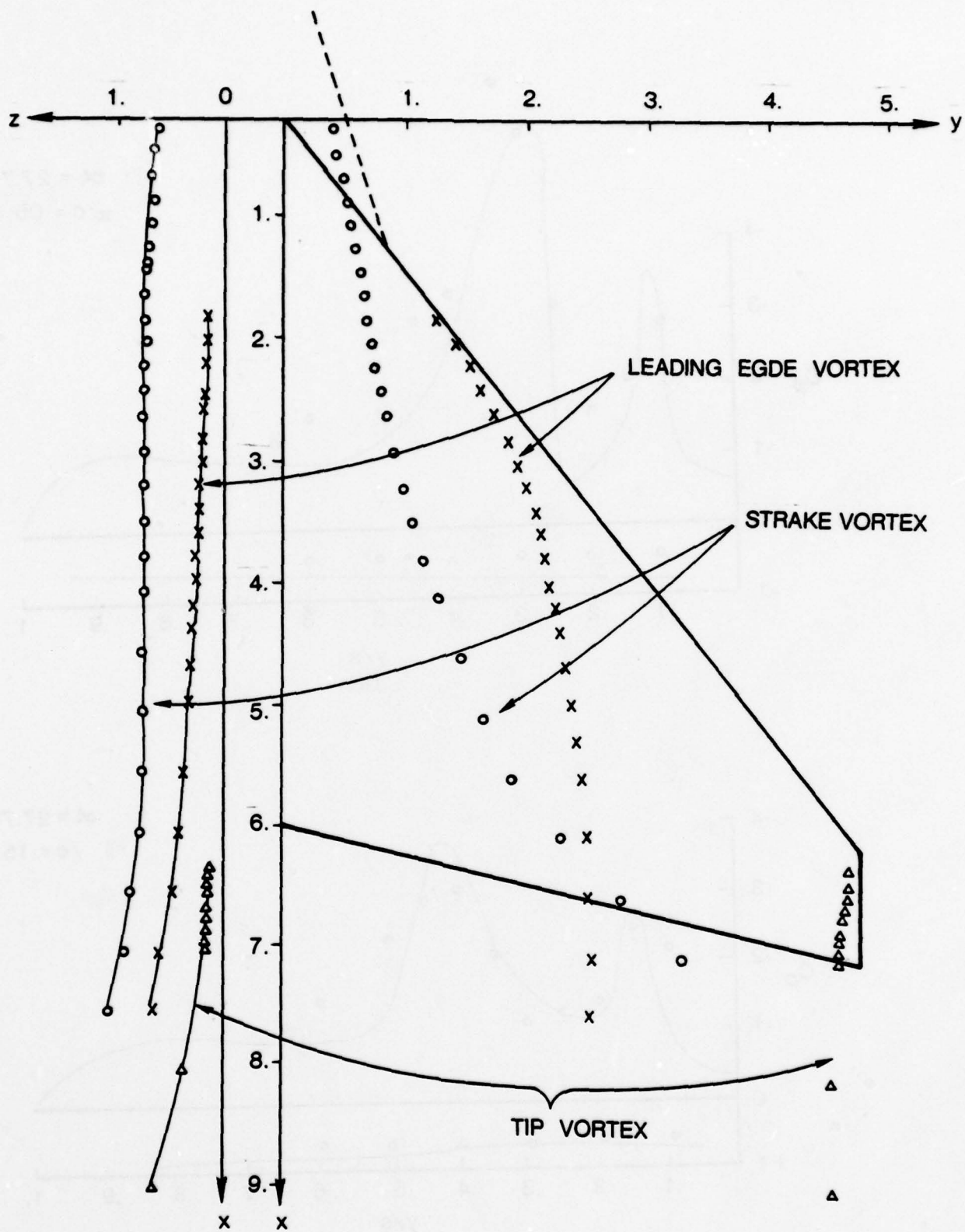
FIG. 46. (Completed)

FIG. 47. The Wing and Vortex Geometry Configuration for
α = 27.7 Degrees.

116
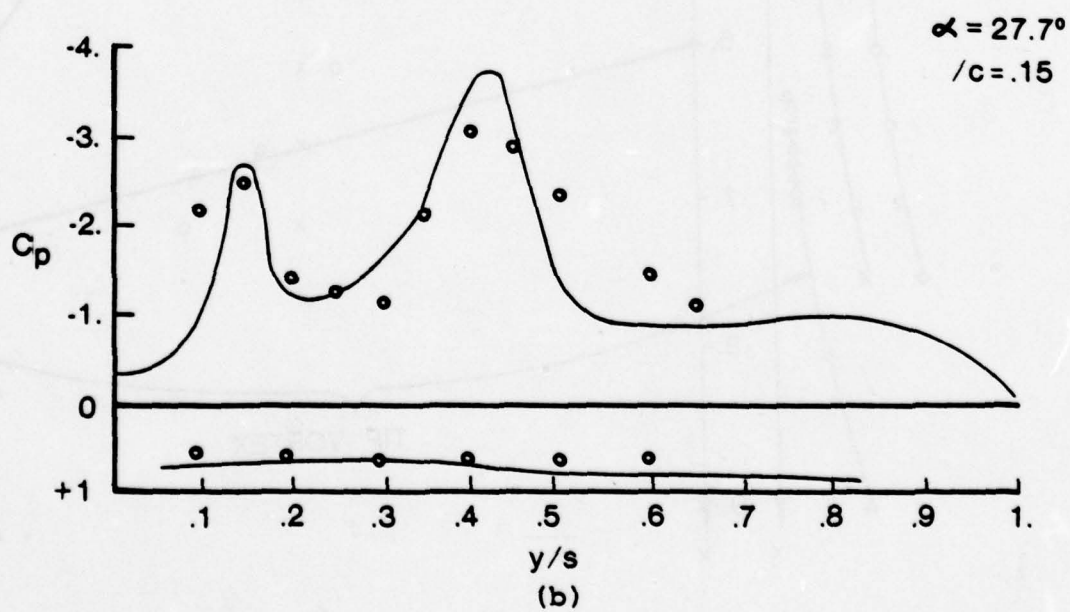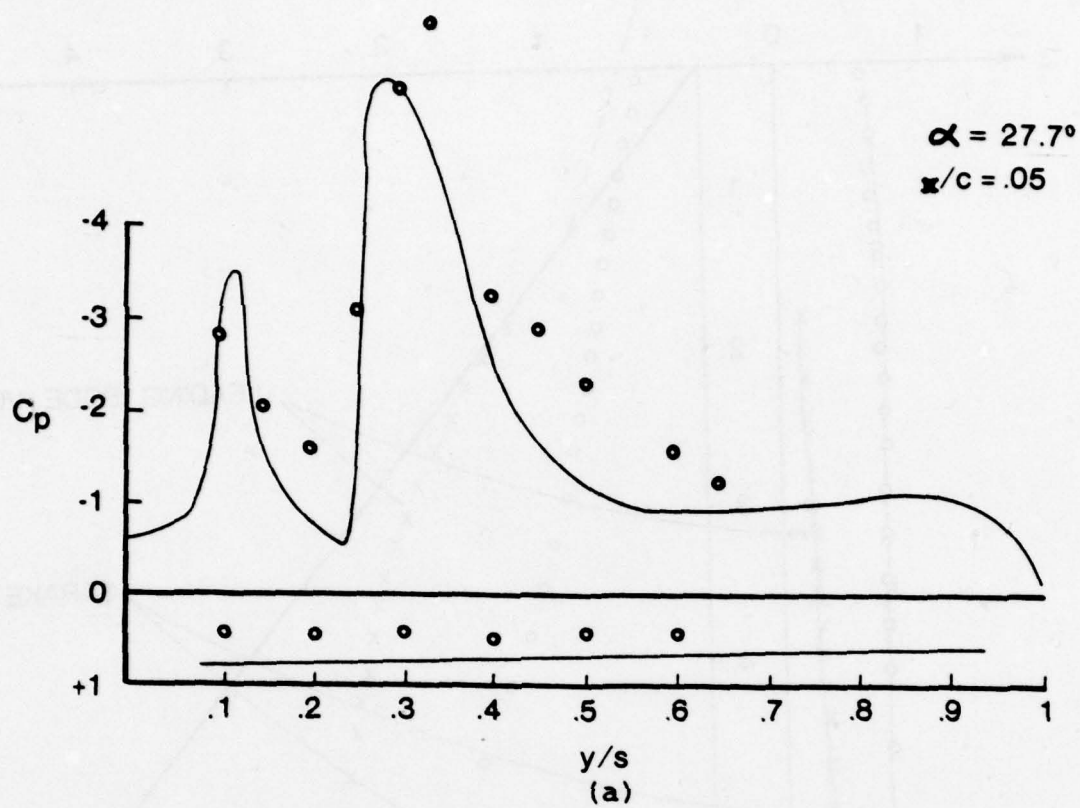
FIG. 48. The Pressure Distribution Along the Constant x/c
Lines.

117

α = 27.7°
x/c = .4

(c)

α = 27.7°
x/c = .6

(d)
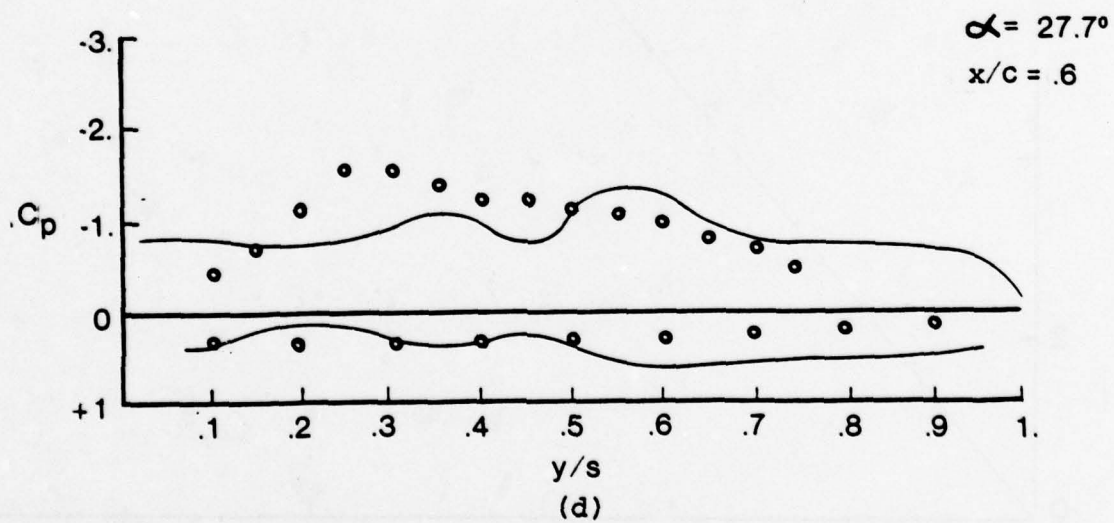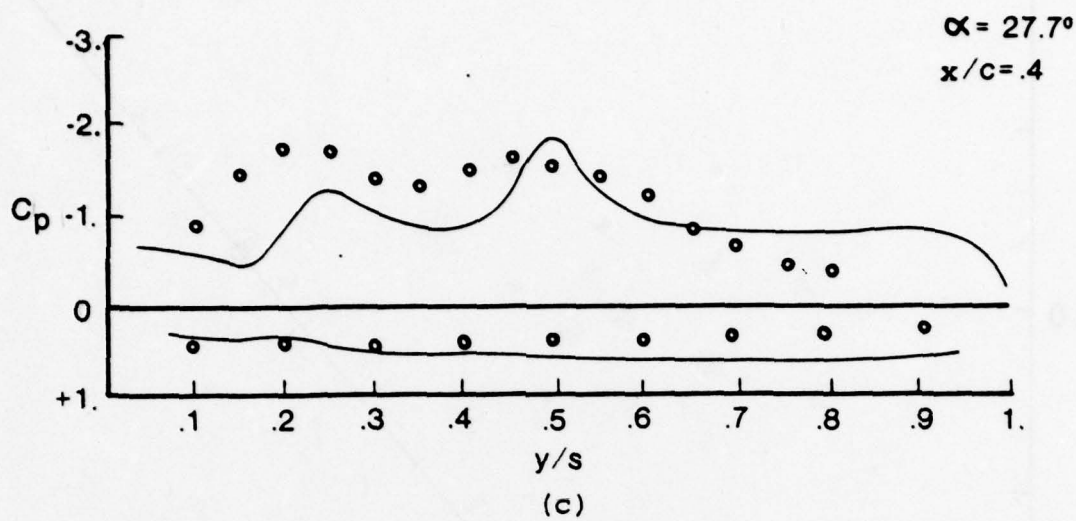
FIG. 48. (Completed)
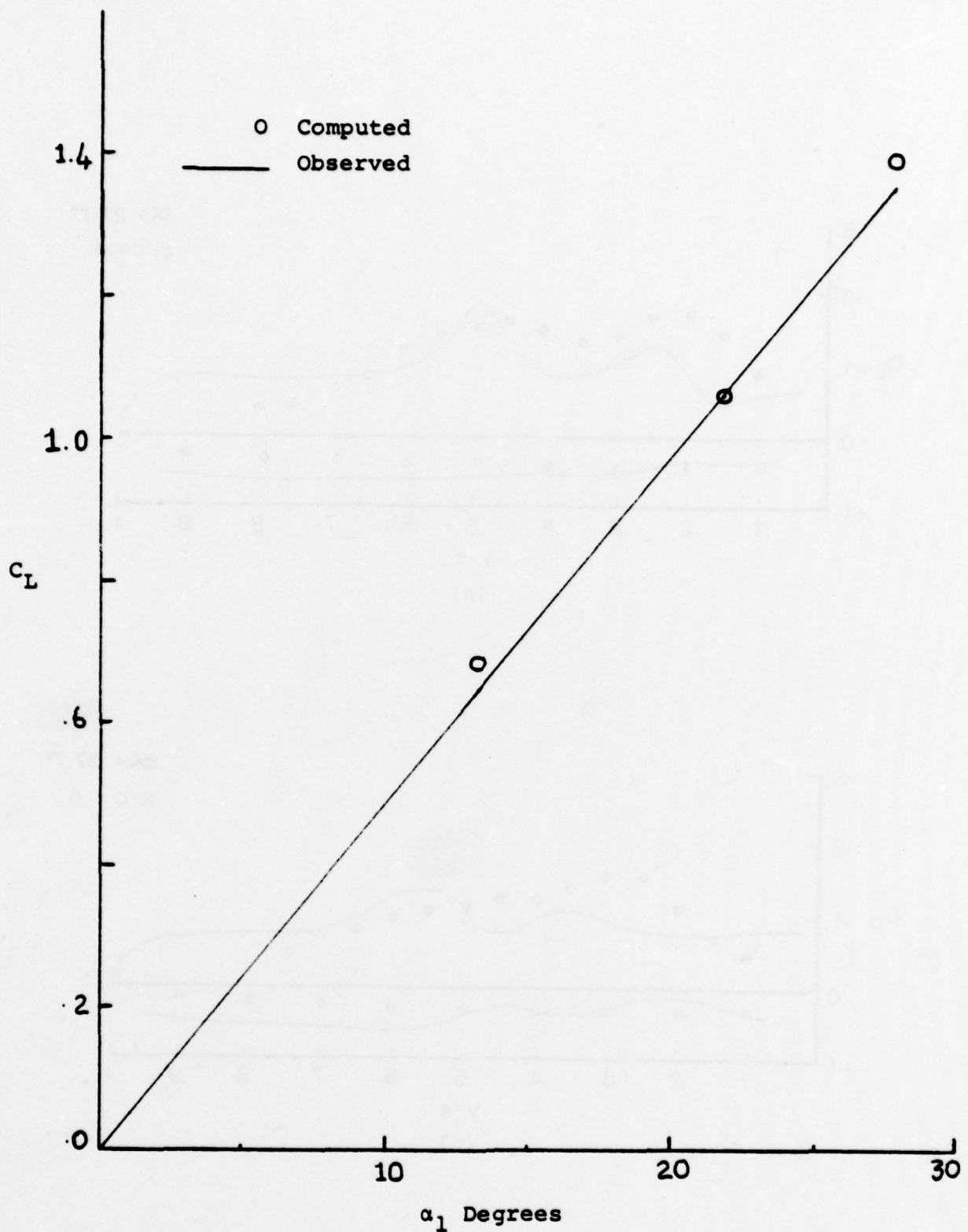
FIG. 49. Comparison of Calculated Total Lift Coefficients with Observed Values.

119

GEOMETRY OF THE VORTEX AT ∝=10°
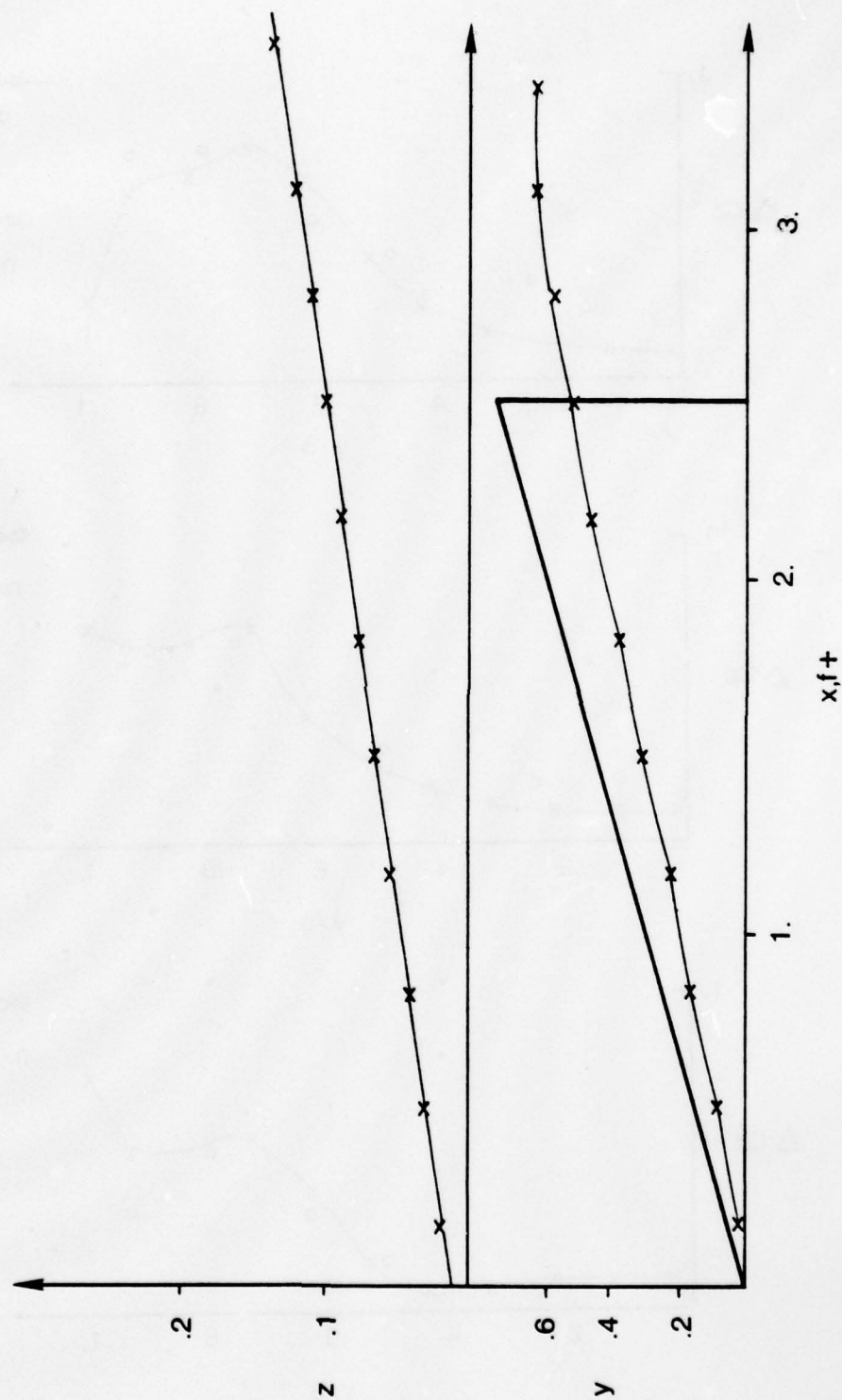
FIG. 50. The Wing and Vortex Geometry Configuration for a Delta Wing of
Aspect Ratio 1.147 at 10 Degrees α.

PRESSURE DISTRIBUTION
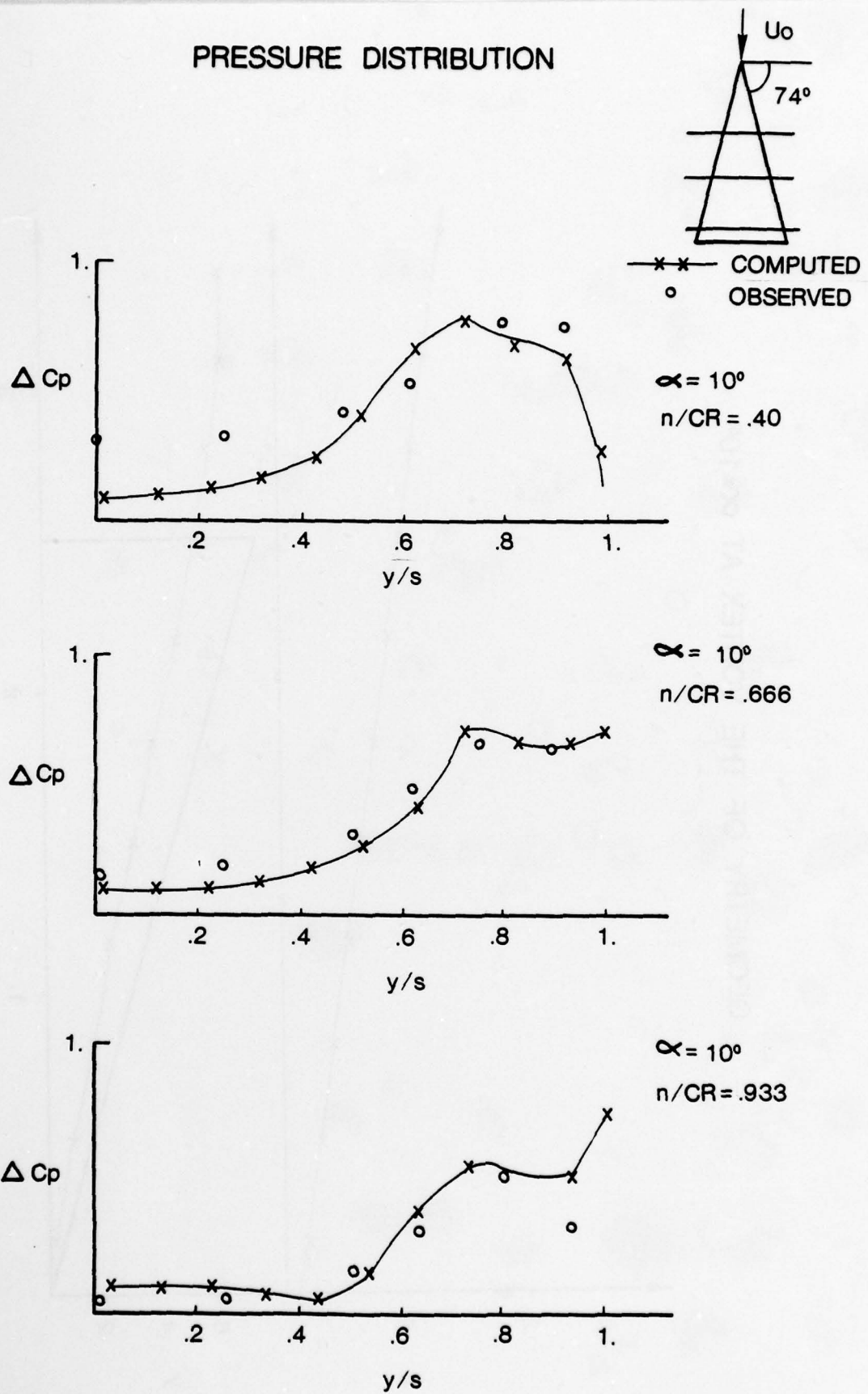
FIG. 51. The Pressure Distribution Along n = constant lines
for a Delta Wing.

121

APPENDIX A

DESCRIPTION OF THE COMPUTER PROGRAM

The flow chart for the program segments is provided in Figure A-1. These segments are briefly described to relate them to the appropriate subroutines in the program. A symbol directory is then provided for the computer variables relating them, wherever possible, to the corresponding algebraic variables.

The input to the program is read from cards in Program VOWHA.

The calculation of the wing box arrangement and control points is done in subroutines BOXES and CONTROL.

The calculations involved in the attached flow doublet distribution solution are performed in subroutines AICWING, VELIND and SOLVE.

The pressures in the attached and separated regions are computed in subroutine POTENL.

The displacement of the free vortices is calculated in subroutine FREEP.

The incremental suction pressures due to the free vortices are calculated in subroutine VTXPRS. The pressure components are added according to Eq. 2.

Each of these subroutines calls certain other secondary routines. All the subroutines are described in a chronological order in which they are accessed in the program.
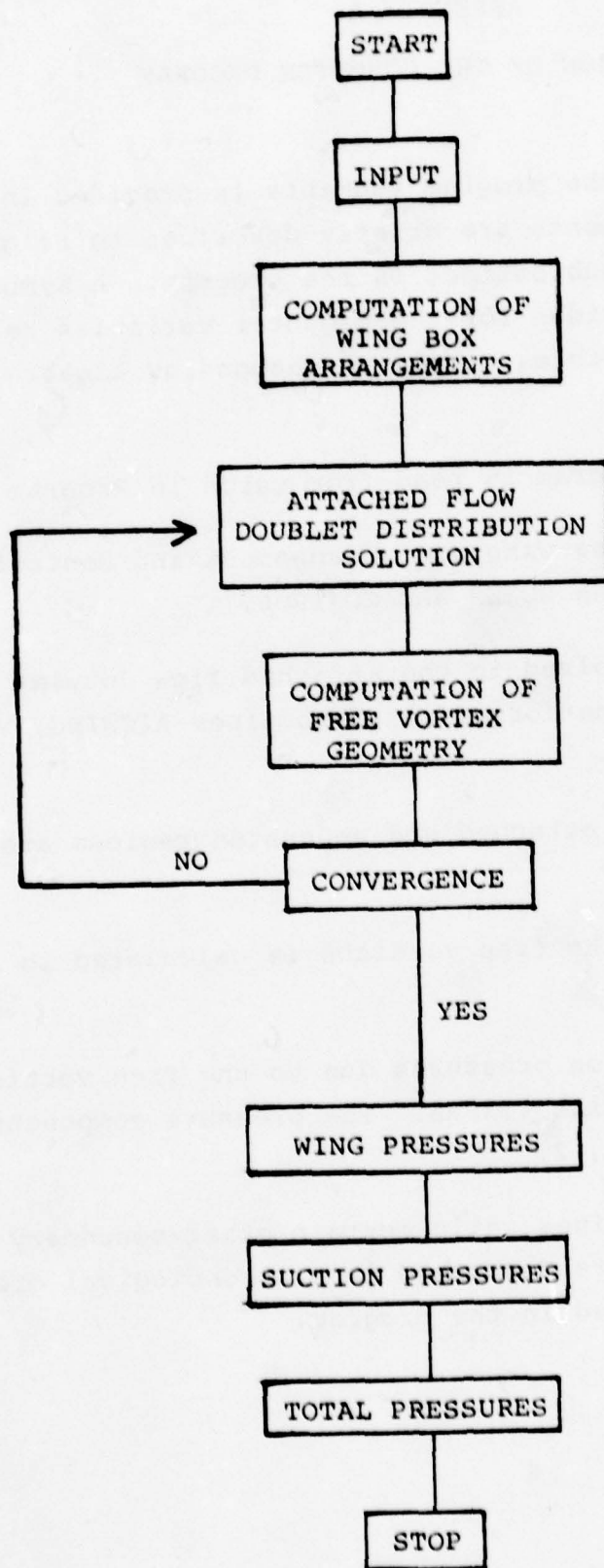
FIGURE A-1: Flow Chart

SYMBOL DIRECTORY

Computer Symbol	Algebraic Symbol	Description
AA	α_o	Geometric angle of attack
ABEVL		Bevel angle for delta wing (used only if NDELTA$\neq$0)
ADELTA		$\pi/2$ - semiapex angle of the delta wing (used only if NDELTA$\neq$0)
AS	α_s	Empirical angle used in the determination of the separated region
B	b	Semispan of the wing
BSML	$v_{t_{s_i}}/U_o$	Nondimensional tangential velocity in the spanwise direction
CBAR		Mean aerodynamic chord.
CHD	C	Chord, local
CLSAVE	C_{L_w}, C_{L_v}	Lift coefficient due to wing and suction resp.
CLTOT	C_L	Total lift coefficient
CMXT	$C_{m_x}, C_{m_{x_w}}, C_{m_{x_v}}$	Moment coefficients around x axis due to forces on the semi-wing
CMYT	$C_{m_y}, C_{m_{y_w}}, C_{m_{y_v}}$	Moment coefficients around y axis due to forces on the semi-wing
CPK	$C_{p_{att_i}}$	Pressure coefficient at a control point on a box in the attached flow region
CPS	$C_{p_{sep_i}}$	Pressure coefficient at a control point on a box in the separated flow region
CPSL	$(dz/dx)_i$	Chordwise slope of the surface at a control point
CPTS	$\Delta C_{p_{v_i}}$	Suction pressure coefficient due to free vortices at a point on the wing

Computer Symbol	Algebraic Symbol	Description
CPXW	x_{c_i}	x coordinate of a control point on a box on the wing (ft)
CPYW	y_{c_i}	y coordinate of a control point on a box on the wing (ft)
CPZW	z_{c_i}	z coordinate of a control point on a box on the wing (ft)
CORER	r_{c_i}	core radius at a control point on the free vortex
DELL	Δs	The length of an element of a free vortex (ft)
DL1,DL3	ℓ_1, ℓ_3	
DM1,DM3	m_1, m_3	Direction cosines used in calculation of the induced velocity due to a vortex element
DN1,DN3	n_1, n_3	
DTIME	Δt	Time interval used in the displacement of the control points on a free vortex (sec)
ERR	ε	Sum of squares of the errors in the coordinates in the vortex displacement calculations
ERRP	ε_p	Input parameter used in the comparison for convergence of vortex geometry
FPI	4π	
FST	$U_o \sin \alpha_s$	Maximum allowable outward normal velocity at a control point on the wing before the flow on the box containing the control point is considered separated (ft/sec)
GAMC	Γ_c	Circulation of the free vortex elements in the constant strength region (ft^2/sec)

Computer Symbol	Algebraic Symbol	Description
GAMK	d_j	Doublet density on a box in the attached flow region of the wing (calculated by satisfying the normal flow boundary condition) (ft^2/sec)
GAMV	Γ_v	Circulation of the free vortex elements in the variable strength (formation) region (ft^2/sec)
GRC	$\nabla D, \nabla d_i$	Gradient of the doublet distribution in the chordwise tangential direction (ft/sec)
GRS		Gradient of the doublet distribution in the spanwise tangential direction (ft/sec)
ISUM		Parameter used to compute the pressure difference between the upper and lower surface
IT		Iteration parameter in the iteration for the doublet strength solution
ITRY		Iteration parameter in the vortex geometry iterations
IW,IWRITE		Output control parameters
KINF	$\Gamma/2\pi$	Circulation of a vortex element divided by 2π, (ft^2/sec)
NACA		Control parameter that effects the computation of z, dz/dx according to NACA 4 digit airfoil geometry equation
NBL	N_l	Number of boxes on the lower surface
NBU	N_u	Number of boxes on the upper surface
NCL	N_{c_l}	Number of chordwise strips of boxes on the lower surface
NCP	N_{c_p}	Number of chordwise lines over which the incremental suction pressure due to free vortices is computed
NCU	N_{c_u}	Number of chordwise strips of boxes on the upper surface of the wing

Computer Symbol	Algebraic Symbol	Description
NDELTA		Integer parameter to select the layout of points at which the incremental suction pressures are computed
NEGC	N_g	Number of elements on each free vortex in the formation region
NINIT		Number of iterations on vortex geometry for each iteration on doublet strength
NIT		Number of iterations on the doublet strength solution
NKVRT		The identification number of the vortex whose variable strength is derived from the doublet solution (subroutine VSTRNG)
NOVE	N_{el}	Number of elements on each free vortex (including the ones in the formation region)
NRL	N_{r_l}	Number of boxes in each chord wise strip of boxes on the lower surface of the wing
NRP	N_{r_p}	Number of spanwise lines (defined by $\bar{x}$ = constant or x = constant) over which $\Delta C_{p_{v_i}}$ is computed
NRU		Number of boxes in each chord-wise strip of boxes on the upper surface of the wing
NSEP	N_{t_e}	Number of boxes on the trailing edge of the wing
NSOLVE	N_a	Number of boxes in the attached region of the wing
NTOT	N	Total number of boxes on the wing surface
NVARV		Number of variable strength elements <10
NVORT	N_v	Number of free vortices
NWBOX	NTE(i)	Identification numbers of boxes on the trailing edge
QNET	$|\bar{q}_i|$	The magnitude of the total velocity at a control point on the free vortex (ft/sec)

Computer Symbol	Algebraic Symbol	Description
	q_{s_i}	Self-induced velocity (in the direction perpendicular to the plane containing two adjacent elements) due to an adjacent element of a control point on the vortex (ft/sec)
	R	Radius of curvature of the vortex at a control point (ft)
RBUR	r_{bur}	Radius of the core just before the vortex core bursts (ft)
SIG	σ_{ij}	Aerodynamic influence coefficients at control points i due to unit density doublet panel on boxes j and j' (ft/sec)
SLLE	$(dx/dy)_{le}$	Slope of the leading edge (assumed straight)
SLTE	$(dy/dy)_{te}$	Slope of the straight trailing edge
SMLA	α_i	Turbulent eddy viscosity parameter at a point on the free vortex
SMLD	d	The distance of a point on the wing from a vortex in the radial direction
SMLH	d'	(d/r_c)
SMLVT	$v_{t_{c_i}}/U_o$	Chordwise tangential velocity at a control point on the wing (nondimensional)
TAU,TAUP	τ	Thickness ratio
TEDGE		The thickness of the edge of the delta wing in inches
THC	θ_i	The angle between the local tangent in the chordwise direction and the horizontal plane (radians)
THICK		The thickness of the flat section of the Δ wing in inches

Computer Symbol	Algebraic Symbol	Description
UZERO	U_o	Free stream velocity (ft/sec)
VAX	v_{a_i}	Axial velocity at the core center at a point on the vortex (ft/sec)
VEDX	$\left(x_{v_i}\right)_{new}$	(x, y, z) coordinates of a control point after displacement of old point (i-1), ft
VEDY	$\left(y_{v_i}\right)_{new}$	
VEDZ	$\left(z_{v_i}\right)_{new}$	
VISAIR	ν	Kinematic viscosity of air (ft^2/sec)
VPHIND	v_{ϕ_i}	Swirl velocity at a point on the wing to a free vortex (ft/sec)
VEX	$\left(x_{v_i}\right)_{old}$	(x, y, z) coordinates of control points on the free vortex, ft
VEY	$\left(y_{v_i}\right)_{old}$	
VEZ	$\left(z_{v_i}\right)_{old}$	
VSTRFAC		A factor used in the computation of the strength of the vortex in subroutine VSTRNG
WI	$w_{n_{v_i}}$	Component of normal velocity at a control point on the wing due to the free vortices (ft/sec)
WNET	w_{n_i}	External normal velocity at control points on the wing (ft/sec)
XB	x_b	x coordinate of the corners of the boxes (ft)

Computer Symbol	Algebraic Symbol	Description
XCAP	s_i	The distance along the vortex centerline at control points (ft)
XER	E_{r_x}	The error in the x coordinate of a displaced control point on the free vortex
XLE	x_{le}	x coordinate of the leading edge of a given chord
XLEAD		The parameter used in subroutine VTXPRS to decide which x=constant lines are used to compute suction pressure at (used only if NDELTA≠0)
XMAC		The x coordinate of the quarter chord point of the mean aerodynamic chord
XPER	$\bar{x}$	Nondimensional coordinates, (given by $(x-x_{le})/(x_{te}-x_{le})$, giving the corners of the boxes
XTE	x_{te}	x coordinate of the trailing edge of a given chord (ft)
XWP	x_{w_i}	x coordinates of the corners of the semi-wing (ft)
YB	y_b	y coordinates of corners of boxes (ft)
YER	E_{r_y}	Error in the y coordinate of a displaced control point on a free vortex
YMAC		The y coordinate of the quarter chord point of the mean aerodynamic chord
YPER	$\bar{y}$	Nondimensional y coordinates of the corners of boxes; $\bar{y} = y/semispan$
YWP	y_{w_i}	y coordinates of corner of the semi-wing (ft)
ZB	z_b	z coordinates of corners of the boxes (ft)

Computer Symbol	Algebraic Symbol	Description
ZER	E_r	Error in the z coordinate of a displaced control point on a free vortex
ZZERO	z_o	The transition distance for the vortex where Batchelor's model becomes applicable (ft)

DESCRIPTION OF ROUTINES

PROGRAM VOWHA (INPUT, OUTPUT, TAPE1, TAPE5 = INPUT, TAPE6 = OUTPUT)

This is the controlling segment of the program. It performs the following functions by calling the appropriate subroutines:

  I. Defines the following files on the scope operating
      system.
      A.   INPUT - the standard system input.
      B.   OUTPUT - the standard system output.
      C.   TAPE1 - unformatted file which stores the influence
                   coefficients σ_{ij} of the doublet panels on
                   the wing

 II. Reads input in the following manner:
           UZERO, AA, AS, TAU, VISAIR, VLIMIT
           XWP, YWP
           CBAR, SMAC, YMAC
           MARB, IWRITE, IW, NDELTA, NGRAD, NSIG
           (If NDELTA $\neq$ 0) THICK, TEDGE, ADELTA, ABEVEL
           (If MARB $\neq$ 0) NRU, NCU, NRL, NCL, NTOT, NBU, NBL,
       NSEP, XB, YB, NWBOX
           (If MARB = 0) NRU, NCU, XPER, YPER

           NVORT, NIT, NINIT, NRP, NCP, ISUM

           (If NVORT $\neq$ 0) NOVE, NEGC, VEX, VEY, VEZ,
       CORER, (If NEGC $\neq$ 0) GAMV, GAMC, ZZERO

           ERRP, VILMT, XLEAD
           VSTRFAC
           NSTR, NKVRT, NVARV
           NACA
III. Writes out input parameters.

A-11

IV. The following subroutines are called in the sequential
order given below.

A. If MARB = 0, calls BOXES to compute the wing box
arrangement.

B. Calls CONTROL to compute the control points and
the z coordinates of box corners.

C. Calls AICWING to compute the aerodynamic influence
coefficients.

D. Calls VELIND to compute the normal velocity in-
duced by the free vortices.

E. Calls SOLVE to determine the attached flow region,
set up the boundary conditions in the attached
region, and solve for wing doublet strengths d_j.

F. Calls POTENL to compute the pressure coefficients
due to doublet panels in the attached and separated
regions of the wing.

G. Calls VSTRNG to derive the vortex strength from the
doublet solution.

H. If NVORT $\neq$ 0 calls FREEP to compute the displaced
vortex geometry which satisfies the force free
condition.

I. If NIT > 0 and IT < NIT, reruns to step C.

J. If IT > NIT and NVORT $\neq$ 0, calls VTXPRS to com-
pute the incremental suction pressures and result-
ing lift.

K. Adds the force and moment coefficients due to
suction and wing.

$$C_L = C_{L_w} + C_{L_v}$$

$$C_{M_x} = C_{M_{x_w}} + C_{M_{x_v}}$$

$$C_{M_y} = C_{M_{y_w}} + C_{M_{y_v}}$$

Subroutine BOXES

I. Computes the (x,y) coordinates of the corners of each box for a given set of constant percentage chord $(\bar{x})$ lines and constant percentage semispan $(\bar{y})$ lines into which the semiwing planform is divided.

These are given by:

$$x_b = x_{le} + \bar{x}(x_{le} - x_{te})$$

$$y_b = \bar{y}b$$

where, x_{le} and x_{te} are obtained for a given y via calls to subroutine EDGES.

II. Computes the total number of boxes on the upper surface (N_u), the total number of boxes on the lower surface (N_1) and the total number of boxes on the semiwing planform (N). These are given by:

$$N_u = N_r \, N_c$$

$$N_1 = N_u$$

and

$$N = N_u + N_1$$

III. Computes the total number of boxes at the trailing
      edge (N_{te}) and identifies the number associated with
      each trailing edge box (NTE(i)).

    N_{te} is given by:

    $$N_{te} = 2 \, N_{c_u}$$

Subroutine EDGES

I. Computes the leading edge and trailing edge x coordinates,
x_{le} and x_{te} respectively, for a given value of y.   These
are given by:

$$x_{le} = x_{w_1} + (dx/dy)_{le} \, (y - y_{w_1})$$

and

$$x_{te} = x_{w_4} + (dx/dy)_{te} \, (y - y_{w_4}).$$

Subroutine CONTROL

  I. Calls subroutine CNTRD to compute the coordinates
      (x_c, y_c) of the control point of each box.

 II. Calls subroutine EDGES to compute the leading and
      trailing edge x coordinates (x_{le} and x_{te} respectively)
      for a given value of y_c.

III. Calls subroutine ZCOR and ZSLP to compute the z_c
      coordinate and the chordwise slope (dz/dx) at each
      control point (x_c, y_c).

 IV. Calls subroutines EDGES and ZCOR to determine the
      z_b coordinates of the corners of all the boxes.

Subroutine CNTRD

I. Computes the x_c and y_c coordinates of the centroid of a given box on the wing. They are given by:

$$x_c = (x_a \cdot A_{124} + x_b \cdot A_{234}) / (A_{124} + A_{234})$$

$$y_c = (y_a \cdot A_{124} + y_b \cdot A_{234}) / (A_{124} + A_{234})$$

where, A_{124} and A_{234} are areas of triangles (124) and (234) respectively, and

$$x_a = (x_1+x_2+x_4)/3. \quad y_a = (y_1+y_2+y_3)/3. \quad z_a = (z_1+z_2+z_3)/3.$$

$$x_b = (x_2+x_4+x_3)/3. \quad y_b = (y_2+y_3+y_4)/3. \quad z_b = (z_2+z_3+z_4)/3.$$
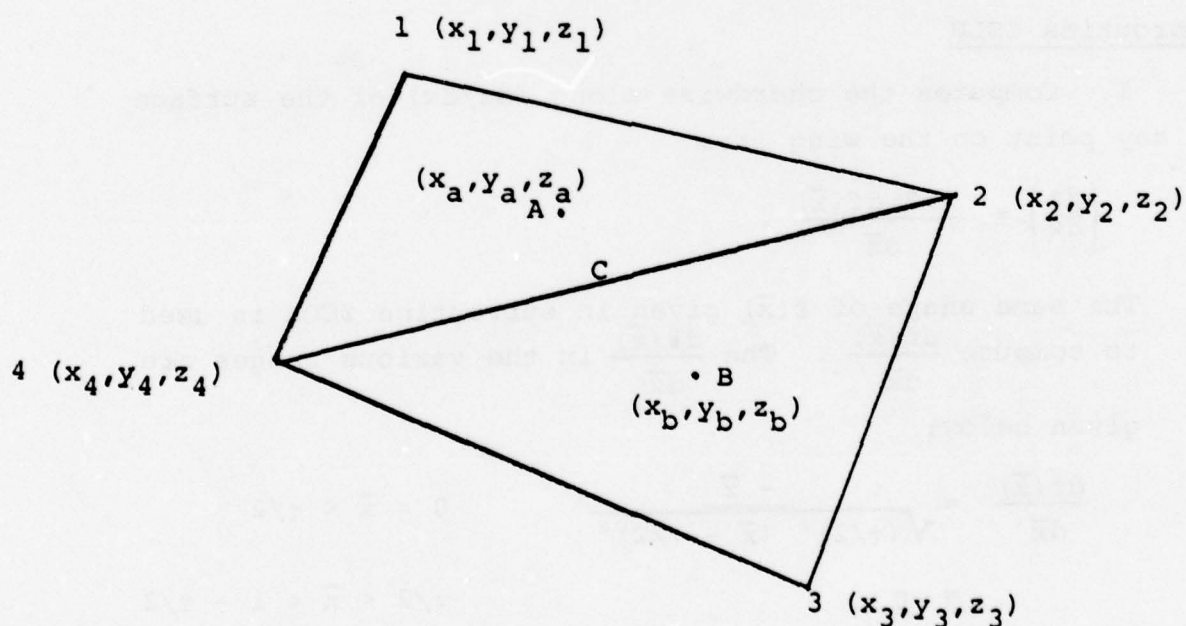
Subroutine ZCOR

I. For a given airfoil shape given by $z = \tau/2 \, f(\bar{x})$, computes the z coordinate at any given point on the surface of the wing. It is assumed that the airfoil shape doesn't change along the span. For a flat plate airfoil of thickness τ with semicircular leading and trailing edges. The airfoil shape is described by

$$f(\bar{x}) = 0, \qquad\qquad\qquad\qquad\qquad \bar{x} < 0$$

$$f(\bar{x}) = \sqrt{(\tau/2)^2 - (\bar{x} - \tau/2)^2}, \qquad 0 < \bar{x} < \tau/2$$

$$f(\bar{x}) = \tau/2, \qquad\qquad\qquad\qquad\quad \tau/2 < \bar{x} < (1 - \tau/2)$$

$$f(\bar{x}) = \sqrt{(\tau/2)^2 - (\bar{x} - 1 + \tau/2)^2}, \quad (1 - \tau/2) < \bar{x} < 1$$

$$f(\bar{x}) = 0, \qquad\qquad\qquad\qquad\qquad \bar{x} > 1.$$

Subroutine ZSLP

I. Computes the chordwise slope (dz/dx) of the surface at any point on the wing from

$$\left(\frac{dz}{dx}\right) = \frac{\tau/2 \; df(\bar{x})}{d\bar{x}}.$$

The same shape of $f(\bar{x})$ given in subroutine ZCOR is used to compute $\dfrac{df(\bar{x})}{d\bar{x}}$. The $\dfrac{df(\bar{x})}{d\bar{x}}$ in the various ranges are given below:

$$\frac{df(\bar{x})}{d\bar{x}} = \frac{-\bar{x}}{\sqrt{(\tau/2)^2 \; (\bar{x} - \tau/2)^2}} \qquad 0 < \bar{x} < \tau/2$$

$$= 0 \qquad\qquad\qquad\qquad \tau/2 < \bar{x} < 1 - \tau/2$$

$$= \frac{-(\bar{x} - 1 + /2)}{\sqrt{(\tau/2)^2 - (\bar{x} - 1 + \tau/2^2}} \qquad (1 - \tau/2) < \bar{x} < 1$$

$$= 0 \qquad\qquad\qquad\qquad \bar{x} > 1.$$

Subroutine AICWING

I. Computes the aerodynamic influence coefficients, σ_{ij}, due to the box j and its image j' at the control point of box i (see the figure below).
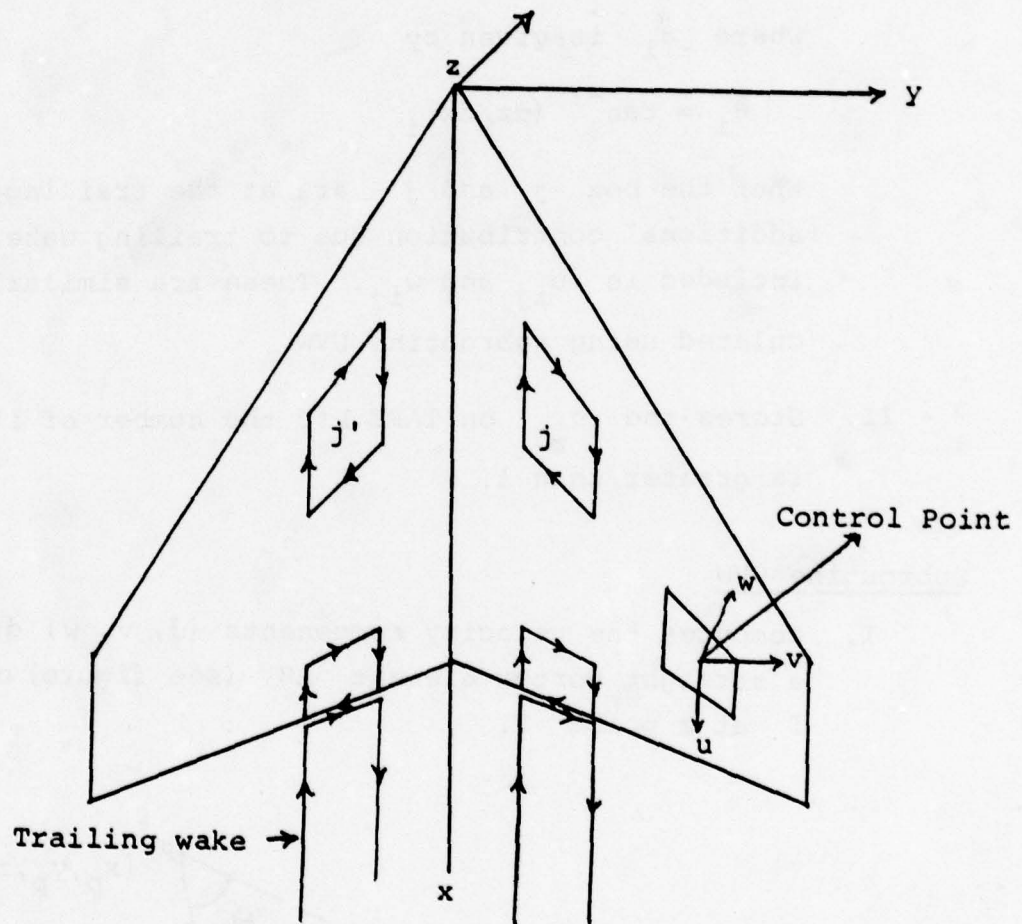
Calls subroutine UVW to compute, (u_{ij}, v_{ij}, w_{ij}), the cartesian velocity components at point i due to boxes j and j'. Computes σ_{ij} using the following formula

$$\sigma_{ij} = u_{ij} \operatorname{Sin} \theta_i - w_{ij} \operatorname{Cos} \theta_i$$

where θ_i is given by

$$\theta_i = \tan^{-1} (dz/dx)_i$$

When the box j and j' are at the trailing edge an additional contribution due to trailing wake is also included in u_{ij} and w_{ij}. These are similarly calculated using subroutine UVW.

II. Stores the σ_{ij} on TAPE 1 if the number of iterations is greater than 1.

Subroutine UVW

I. Computes the velocity components (u, v, w) due to a straight vortex element AB (see figure) of strength Γ at a point P.
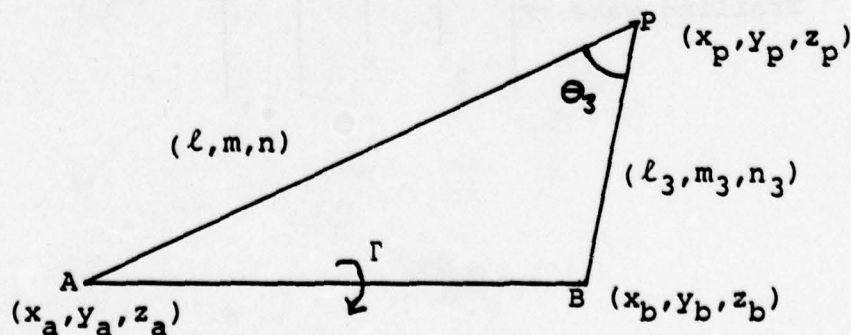
$$u = \left(\frac{\Gamma}{AP} + \frac{\Gamma}{PB}\right) \left(\frac{m_1 n_3 - m_3 n_1}{1 + \cos\theta_3}\right)$$

$$u = \left(\frac{\Gamma}{AP} + \frac{\Gamma}{BP}\right) \frac{n_1 \ell_3 - \ell_1 n_3}{1 + \cos\theta_3}$$

$$w = \left(\frac{\Gamma}{AP} + \frac{\Gamma}{BP}\right) \frac{\ell_1 m_3 - \ell_3 m_1}{1 + \cos\theta_3}$$

where

AP and BP are lengths of lines AP and BP, (ℓ_1, m_1, n_1) and (ℓ_3, m_3, n_3) are the direction cosines and θ_3 is included angle given by

$$1 + \cos\theta_3 = 1 + \frac{(X_P - X_A)(X_P - X_B) + (Y_P - Y_A)(Y_P - Y_B) + (Z_P - Z_A)(Z_P - Z_B)}{PA \cdot PB}$$

$$\ell_1 = \frac{X_P - X_A}{PA}, \quad m_1 = \frac{Y_P - Y_A}{PA}, \quad n_1 = \frac{Z_P - Z_A}{PA}$$

$$\ell_3 = \frac{X_P - X_B}{PB}, \quad m_3 = \frac{Y_P - Y_B}{PB}, \quad n_3 = \frac{Z_P - Z_B}{PB} .$$

Subroutine VELIND

I. Computes the Cartesian components (u_i, v_i, w_i) at control point i due to the free vortices whose geometry and strength is known by calling subroutine UVW.

II. Computes the normal component of velocity due to free vortices from

$$w_{n_{v_i}} = u_i \sin\theta_i - w_i \cos\theta_i$$

A-19

Subroutine SOLVE

    I.   Computes the net normal velocity component, w_{n_i}, at

        a control point i, due to free stream velocity and
free vortices. It is given by:

$$w_{n_i} = U_o \, Sin \, (\alpha_o - \theta_i) - w_{n_{v_i}}$$

    II.   Determines the attached flow region by comparing the
outward normal w_{n_i} with $U_o \, Sin \, \alpha_s$. The box i is

        considered attached when

$$w_{n_i} \Big|_{outward} < U_o \, Sin \, \alpha_s \, .$$

    III.   Sets up equations

$$\sum_{j=1}^{N_A} \sigma_{ij} \, d_j = w_{n_i} \qquad i = 1, \; --- \; N_A$$

        where N_A is the number of boxes where flow is attached.

    IV.   Solves the above equation by calling subroutine SLSESO
for values of d_j

Subroutine SLSESO

    I.   Solves the linear algebraic system of equation

$$\sigma_{ij} \, d_j = w_i, \qquad\qquad i = 1, \; \cdots \; N$$

        row by row.

        The σ_{ij} for (j = 1, N) are obtained from subroutine
READR.

Subroutine READR

    I.   Reads the influence coefficients σ_{ij} from TAPE 1.

    II.   If any separated boxes are present, automatically
eliminates the rows of σ_{ij} related to those boxes
from computation.

Subroutine VSTRNG

I. This subroutine interpolates between the values of difference of doublet strengths on the lower surface from that on the upper surface to obtain strength of the leading edge vortex. (This was used for NDELTA $\neq$ 0).

Subroutine FREEP

I. Computes the core radii at the end points of all free vortex elements using the following formulas.

$$r_{c_i} = .0264 \ \underline{(s_o + s_i)} \ \alpha_1 \quad 0 < s_i < z_o$$

$$r_{c_i} = .0264 \ \alpha_i \ (s_o + z_o) \sqrt{\frac{y_i + (s_i - z_o)}{y_o}} \quad s_i > z_o$$

where.

s_i is the distance along the leading edge vortex, at the free vortex element i,

z_o is the value of s_i at which the viscous vortex core model is changed,

$$s_o = r_{c_i} \Big/ (.0264) \ \alpha_1$$

$$y_o = \frac{(.02488) \ \alpha_i \ U_o \ (s_o + z_o)^2 \ 2\pi}{\Gamma_i} \quad ,$$

and Γ_i is the vortex strength of the free vortex element.

The eddy viscosity parameters α_1 and α_i are obtained via calls to subroutine EDDYV.

The axial velocity in the core of the free vortex element i is given by:

$$v_{a_i} = \frac{1.26 \, \Gamma_i}{2\pi \, r_{c_i}} \qquad\qquad o < s_i < z_o$$

$$v_{a_i} = \frac{0.02487 \, \Gamma_i}{2\pi} \, \alpha_i \left(\frac{s_o + z_o}{r_{c_i}^2} \right) \qquad s > z_o \; .$$

The point of bursting of free vortex is specified by the location along the vortex at which the core radius equals r_b and is given by

$$r_b = .04 \, (s_o + s_i) \, \alpha_i$$

For vortex elements beyond the point of bursting, the axial core velocity is given by

$$v_{a_i} = \frac{.002488 \, \Gamma_i \, \alpha_i}{2\pi} \left(\frac{s_o + z_o}{r_{c_i}^2} \right)$$

II. Calls subroutine VELBOX to compute the induced velocity components due to attached doublet distribution.

III. Computes the induced velocity due to all the elements of the free vortices at a control point i on the vortex except due to the adjacent elements.

IV. Calls subroutine SLFUVW to compute the effect of the adjacent elements a control point on the vortex.

V. Limits the induced contribution due to the doublets and the vortices to a given value VILMT provided as input.

VI. Computes the total velocity by adding all the velocity components (including the free stream component) to obtain

$$\bar{q} = u_i \, \hat{i} + v_i \, \hat{j} + w_i \, \hat{k} \; .$$

V. Computes the time interval, Δt, required for displacement of the point i which is given by

$$\Delta t_i = \frac{\Delta S_i}{|\bar{q}|}$$

where

$$\Delta S_i = \sqrt{(x_{v_{i+1}} - x_{v_i})^2 + (y_{v_{i+1}} - y_{v_i})^2 + (z_{v_{i+1}} - z_{v_i})^2}$$

and

$$|\bar{q}| = \sqrt{u_i^2 + v_i^2 + w_i^2}$$

VII. Computes the displacements of the point i and adds them to its old coordinates to get the new location of point i ($i+1$ in the next iteration)

$$\left(x_{v_{i+1}}\right)_{new} = \left(x_{v_i}\right)_{old} + u\Delta t$$

$$\left(y_{v_{i+1}}\right)_{new} = \left(y_{v_i}\right)_{old} + v\Delta t$$

$$\left(z_{v_{i+1}}\right)_{new} = \left(z_{v_i}\right)_{old} + w\Delta t$$

VIII. Computes the errors in the locations of the points on the vortex as given by

$$E_{r_x} = \left(x_{v_{i+1}}\right)_{new} - \left(x_{v_{i+1}}\right)_{old}$$

$$E_{r_y} = \left(y_{v_{i+1}}\right)_{new} - \left(y_{v_{i+1}}\right)_{old}$$

$$E_{r_z} = \left(z_{v_{i+1}}\right)_{new} - \left(z_{v_{i+1}}\right)_{old}$$

and sums the squares of those errors as follows:

$$\varepsilon = \sum_{i = 1}^{N_{el}} \left(E_{r_x}^2 + E_{r_y}^2 + E_{r_z}^2 \right)$$

where, N_{el} is the number of elements in each vortex.

IX. The quantity $\sqrt{\varepsilon/N_{el}}$ is compared with ε_p (an input) for convergence. The geometry is considered to have converged if

$$\sqrt{\varepsilon/N_{el}} < \varepsilon_p.$$

Subroutine EDDYV

I. Computes the turbulent eddy viscosity parameter α_i from the formula

$$\alpha_i = 197 \sqrt{Re} + .6$$

where

$$Re = \frac{\Gamma_i}{2 \pi \nu}$$

where

ν is kinematic viscosity and Γ_i is the vortex strength of the element i.

Subroutine VELBOX

I. Computes the velocity components (u, v, w) at a given point in space due to the doublet distribution on the attached region of the wing. The computation proceeds essentially in the same manner as in subroutine AICWING, except here the doublet strengths are known and the contribution due to all the boxes is added together. The image boxes and the trailing wake elements are considered in a similar manner as in subroutine AICWING.

A-24

Subroutine SLFUVW

I. Computes the velocity components at a point i on the free vortex due to the adjacent element (see figure below)
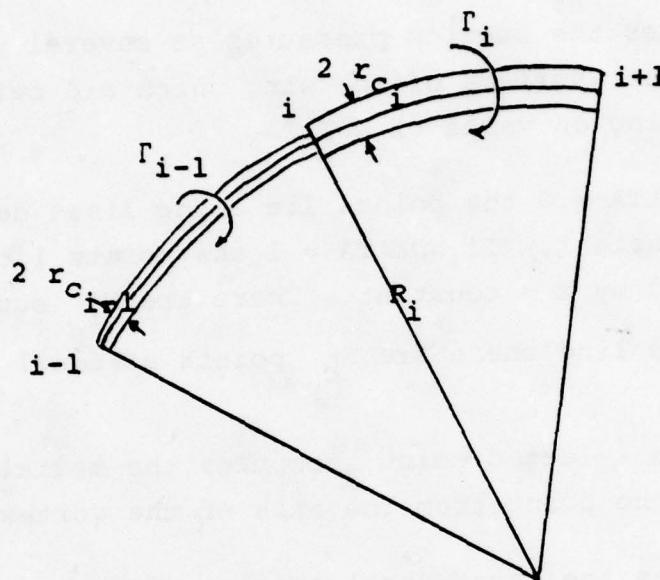
The velocity perpendicular to the plane containing the points (i-1, i, i+1) is given by

$$q_{s_i} = \frac{1}{8 \wedge R_i} \left\{ \Gamma_i \, \ell n \left(\frac{8R_i}{r_{c_i}} \tan \frac{\phi_i}{4} \right) + .25 \right\}$$

This is the contribution from element (i, i+1). The R_i is the radius of curvature, and ϕ_i is the included angle.

II. Computes the appropriate Cartesian components of q_{s_i}.

Subroutine VTXPRS

I. Computes the suction pressures at several points on the upper surface of the wing which are selected depending on value of NDELTA.

If NDELTA = 0 the points lie along lines defined by $\bar{x}$ = constant. If NDELTA = 1 the points lie on lines defined by x = constant. There are N_{r_p} such lines and on each line there are N_{c_p} points at equal intervals.

II. At each selected point, computes the radial distance, d, of the point from the axis of the vortex.

III. Computes the incremental suction pressures using the following formulas.

$$\Delta c_{p_{v_i}} = \frac{.672\Gamma_i}{2\pi\, r_{c_i}} \left\{ (13.14065)\,(.61)\, e^{-1.32\left(d_i/r_{c_i}\right)} \right.$$

$$+ \frac{2.08}{\left(d_i/r_{c_i}\right)^2} \left[1 - 1.482\, e^{-.882\left(d_i/r_{c_i}\right)^2} \right.$$

$$\left. \left. + .549 \left(1 - 1.482\, e^{-.882\left(d_i/r_{c_i}\right)^2} \right)^2 \right] \right\}$$

$$0 < s_i < z_o$$

or

$$\Delta C_{p_{v_i}} = -4 \frac{v_{\phi_i}^2 + v_{a_i}^2}{u_o^2} \qquad\qquad S_i > Z_o$$

where,

$$v_{\phi_i} = \frac{\Gamma_i}{2\pi r_{c_i}} \left[1 - e^{-1.11\left(d_i/r_{c_i}\right)^2} \right]$$

$$v_{a_i} = \frac{.02847\Gamma_i\alpha_i}{2\pi} \left[\frac{S_o + Z_o}{r_{c_i}^2} \right] (2.48) \left[.78\, e^{-.66\left(d_i/r_{c_i}\right)} \right]$$

V. Computes the total lift coefficient, $C_{L_{\bar{v}}}$, due to
    incremental suction pressures.

V. Computes the total moment coefficients, $C_{m_{x_v}}$ and $C_{m_{y_v}}$,
    about x and y axes respectively, due to forces on the
    semi-wing.

VII. Sets up the arrays for interpolation of potential pres-
     sure by calling subroutine INTARR.
     Interpolates between the potential pressure values on the
     upper surface and adds the potential and suction components
     of the pressure.

Subroutine INTARR
    I. Sets up the interpolating arrays of values associated
        with functions such as pressure and doublet strengths at
        control points on the wing. These arrays are used to
        interpolate for values of these functions at points on
        the wing other than the control points.

Subroutine POTENL

I. Calls subroutines VELBOX to compute the induced velocity components (u_i, v_i, w_i), due to the doublet panels on the attached flow region of the wing.

II. Computes the chordwise gradients, ∇d_i, of the doublet strength, by calling subroutine GRADNT.

III. Computes the chordwise and the spanwise tangential velocity components as given by

$$v_{t_{c_i}} = u_i \cos \theta_i + w_i \sin \theta_i + \nabla d_i/2.$$

$$v_{t_{s_i}} = v_i$$

IV. Computes the pressure coefficient at a control point on a box in the attached flow region by using the Bernoulli equation in the form

$$C_p = 1 - \cos^2 (\alpha_o - \theta_i) - \frac{2 \, v_{t_{c_i}}}{U_o} \cos (\alpha_o - \theta_i)$$
$$- \frac{v_{t_{c_i}}^2 + v_{t_{s_i}}^2}{U_o} \; .$$

V. Computes the pressure coefficients on the boxes where flow is separated using the following formula

$$C_{p_{sep_i}} = 1 - \frac{|\bar{q}_i|^2}{U_o^2}$$

where $|\bar{q}_i|$ is the total tangential velocity and does not include the local contribution $\nabla d_i/2$.

VI. Computes the total lift and moment coefficients C_{L_w}, $C_{m_{x_w}}$, $C_{m_{y_w}}$ due to forces on the semi-wing.

Subroutine OUTPUT

I. Divides the boxes in the chordwise and spanwise lines and prints out the array containing the values related to the control points of boxes on the wing in those chordwise and spanwise lines, both for upper and lower surfaces.

Subroutine GRADNT

I. Computes the value of the gradient of doublet strength at a point on the wing.

<u>First</u> <u>Card</u>: (16A5)

   a. 80 character title

<u>Next</u> <u>Card</u>: (8F10.6)

   a. UZERO,   the free stream velocity, ft/sec

   b. AA,   the angle of attack, radians

   c. AS,   the angle used in the determination of separated flow region, radians

   d. TAU,   the thickness ratio of the wing

   e. VISAIR,   the kinematic viscosity of air, ft^2/sec

<u>Next</u> <u>Card</u>: (8F10.5)

   a. XWP,   the x coordinates of the four corners of the semi-wing, ft

   b. YWP,   the y coordinates of the four corners of the semi-wing, ft

<u>Next</u> <u>Card</u>: (8F10.5)

   a. CBAR,   the mean aerodynamic chord

   b. XMAC,   the x coordinate of the quarter chord point of the mean aerodynamic chord

   c. YMAC,   the y coordinate of the quarter chord point of the mean aerodynamic chord

<u>Next</u> <u>Card</u>: (16I5)

   a. MARB,   the integer parameter controlling the calculation of the x and y coordinates of the corners of boxes and related input

                               = 1 if box coordinates are to be read in directly

                               = 0 if the box coordinates are to be computed in the program

   b. IWRITE,   the integer parameter controlling the print output of subroutines FREEP and INTERP

   c. IW,   the integer parameter controlling the print output of subroutines BOXES, CONTROL and VTXPRS

d. NDELTA,   the integer parameter controlling the grid
                        points at which the suction pressure is
                        calculated

                        = 1 if these points are to lie on constant
                        $\bar{x}$, $\bar{y}$ lines

                        =0 if these points are to lie on constant
                        x lines

e. NGRAD,   the integer parameter to control the
                        computation of the gradient of doublet
                        strength

                        $\neq$ 0 if the gradient is to be computed
                              in both spanwise and chordwise
                              direction

                        = 0 if the gradient is to be computed
                              in only the chordwise direction

f. NSIG,   the integer parameter to control the
                        computation of σ_{ij} in subroutine A1CWING

                        = 1 if the file TAPE 1 already has the
                              σ_{ij} stored

                        = 0 if the σ_{ij} are to be newly computed
                              in the present run

Next Card: (8F10.5)   To be read if NDELTA $\neq$ 0

a. THICK,   thickness of the flat plate delta wing,
                        inches

b. TEDGE,   thickness at the edge of the beveled
                        delta wing, inches

c. ADELTA,   the angle between the y axis and the
                        leading edge of the delta wing, degrees

d. ABEVEL,   the bevel angle, degrees

Next Card: (16I5)   To be read if MARB = 0

a. NRU,   the number of boxes in a chordwise strip
                        of boxes on the wing

b. NCU,   the number of chordwise strips of boxes
                        on one surface of the wing

Next Card: (16F5.3) To be read if MARB = 0

a. XPER,   the $\bar{x}$ values that form spanwise edges
                        of the boxes

A-31

<u>Next</u> <u>Card</u>:   (16F5.3)   To be read if MARB = 0

   a. YPER,   the $\bar{y}$ values that form the chordwise
                                  edges of the boxes

<u>Next</u> <u>Card</u>:   (16I5)   To be read if MARB $\neq$ 0

   a. NRU,   the number of boxes on each chordwise
                                  strip on the upper surface

   b. NCU,   the number of chordwise strips of boxes
                                  on the upper surface of the wing

   c. NRL,   the number of boxes on each chordwise
                                  strip on the lower surface of the wing

   d. NCL,   the number of chordwise strips of boxes
                                  on the lower surface of the wing

   e. NTOT,   the total number of boxes on the wing
                                  (must be less than 200)

   f. NBU,   the total number of boxes on the upper
                                  surface = NRU x NCU

   g. NBL,   the total number of boxes on the lower
                                  surface = NRL x NCL

   h. NSEP,   the total number of boxes at the trailing
                                    edge of the wing

<u>Next</u> <u>NTOT</u> <u>Cards</u>:   (8F10.5)   To be read if MARB $\neq$ 0

   a. XB,   the x coordinates of the 4 corners of
                                    each box, ft

   b. YB,   the y coordinates of the 4 corners of
                                    each box, ft

<u>Next</u> <u>Card</u>:   (20I4)   To be read if MARB $\neq$ 0

   a. NWBOX,   the identification numbers of the NSEP
                                    trailing edge boxes

<u>Next</u> <u>Card</u>: (16I5)

a. NVORT,   the number of vortices

b. NIT,   the number of iterations on the surface doublet distribution

c. NINIT,   the number of iterations on the vortex geometry for each solution of the doublet distribution

d. NRP,   the number of spanwise lines on which the incremental suction pressure is calculated

e. NCP,   the number of points on each spanwise line at which the incremental suction pressure is calculated

f. ISUM,   integer parameter that controls the calculation of the pressure (to be used only for very thin wings)

                                   = 1 if the pressure difference between the upper and lower surface is desired

                                   = 0 if the pressure on each surface is desired

The following NVORT sets of cards to be read if NVORT ≠ 0

<u>Next</u> <u>Card</u>: (16I5)

a. NV,   the number of points on the vortex, NOVE = NV - 1

b. NEGC,   the number of elements on the vortex with variable strength

<u>Next</u> <u>NV</u> <u>Cards</u>: 8F10.5)

a. VEX,   the x coordinates of the point on the vortex, ft

b. VEY,   the y coordinates of the point on the vortex, ft

c. VEZ,   the z coordinates of the point on the vortex, ft

d. CORER,   the core radius of the point on the vortex, ft. Only the first value needs to be given, the other values are computed within the program

<u>Next</u> <u>NEGC</u> <u>Cards</u> are present only if NEGC ≠ 0:   (8F10.6)

    a. GAMV,   the strength of the element of vortex,
                                      in the variable strength region, ft^2/sec

<u>Next</u> <u>Card</u>: (8F10.6)

    a. GAMC,   the strength of constant portion of the
                                      vortex, ft^2/sec

    b. ZZERO,   the transition distance, z_o, ft

<u>Next</u> <u>Card</u>: (8F10.6) To be read after NVORT sets of cards are
                          read in and if NVORT ≠ 0

    a. ERRP,   the error parameter for comparison in
                                      subroutine FREEP

    b. VILMT,   the limit on induced velocity

    c. XLEAD,   is the distance that controls the lines
                                      at which the computation of suction pres-
                                      sure is done, (takes effect only when
                                      delta wing is considered), inches

<u>Next</u> <u>Card</u>: (8F10.6)

    a. VSTRFAC,   the factor which is used to derive the
                                      strength of the vortex from the doublet
                                      solution (to be used only for delta wing)

<u>Next</u> <u>Card</u>: (16I5)

    a. NSTR,   the integer to control whether the strength
                                        derived from the doublet solution is used
                                      in the further calculations

                                      ≠ 0 if yes

                                      = 0 if no

    b. NKVRT,   the identifying number of the vortex for
                                      which the strength is derived from the
                                      doublet strength

                                      (has to be 1, 2, 3 or NVORT)

                                      usually the leading edge vortex

c. NVARV   the number of elements in the above
                            vortex whose strength is derived from
                            the doublet solution

<u>Next</u> <u>Card</u>:   (16I5)

a. NACA   integer to control the computation of z
                            coordinate and dz/dx

        = 1   if NACA 4 digit aircoil equations are
               to be used

        = 0   if the beveled delta equations are
               to be used

The format in which the card is read is placed in the parenthesis
next to the card identifier.

The following limitations are placed on certain variables.

    NTOT < 200
    NRUxNCU < 100
    NSEP < 30
    N_g < 10
    N_u < 29

due to the dimensioning in the program.

The following limitations are placed on the variables due to
output formatting

    NCU < 10.

The vortex geometry is supplied from the experimental investiga-
tions in the literature. The strengths GAMC and GAMV are pro-
vided based on the following. The program can be run with high

A-35

α_s ($\alpha_s = 1.5$) and no vortices to obtain a potential solution without separation. The difference of doublet strengths of the leading edge boxes on the upper and lower surface can be plotted against $\bar{y}$.
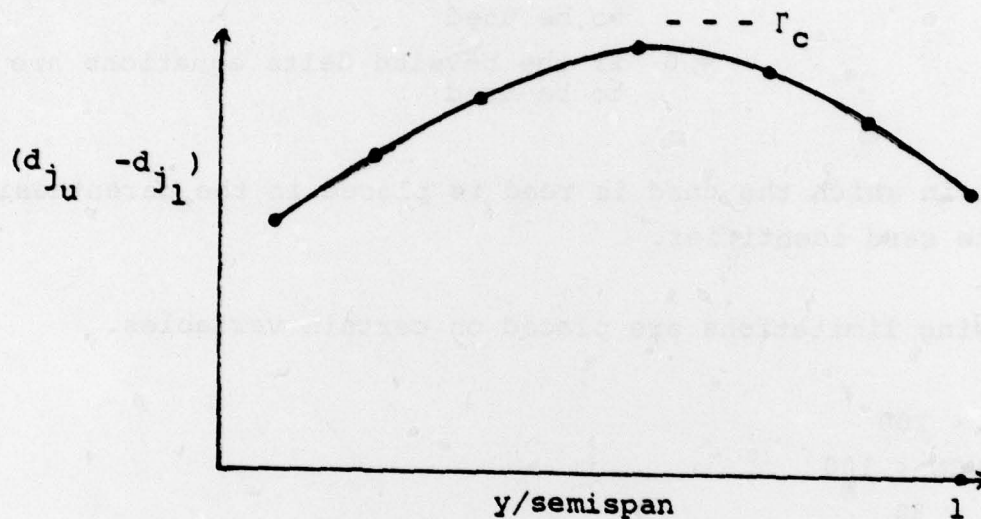
See the figure. The maximum of $(d_u - d_l)$ can be used as the initial guess for GAMC for the leading edge vortex. The values of GAMV (the variable strengths) can be derived from the same plot based on $\bar{y}$ coordinates of the leading edge vortex. The values of these strengths for strake and tip vortices are arrived at from experience.

OUTPUT OUTLINE

I. Input

Computer Name	Algebraic Name	Description
UZERO	U_o	free stream speed
AA	α_o	angle of attack
AS	α_s	angle used in the determination of the separated flow region
XWP,YWP	x_{w_i}, y_{w_i}	the x and y coordinates of the semi-wing corners
NVORT	N_v	number of vortices
NIT		number of iterations on the doublet distribution solution
NINIT		number of iteration on the vortex geometry

II. The wing box arrangement information (MARB = 0)

NTOT	N	number of boxes on the wing
NBU	N_u	number of boxes on the upper surface
NBL	N_l	number of boxes on the lower surface
NSEP	N_{te}	number of boxes at the trailing edge
NWBOX	NTE(i)	numbers identifying the boxes at the trailing edge
NRU		number of boxes on each chord wise strip of boxes on the upper surface
NCU		number of chordwise strips of boxes on the upper surface
NRL		number of boxes in each chord wise strip of boxes on the lower surface

Computer Name	Algebraic Name	Description
NCL		number of chordwise strips of boxes on the lower surface
XB,YB,ZB		the coordinates of corners of the boxes
CPZW,CPYW, CPZW,CPSL		the coordinates and slopes at the control points

III. Attached flow doublet distribution solution

IT		the iteration number
GAMK	d_j	the values of uniform density doublet panel strength on the boxes where flow is attached
	$(d_{ju}-d_{je})$	the difference of doublet strengths on upper and lower surface

IV. Pressure calculation in the attached and separated region

PX,PY,PZ		velocity components induced by the doublets on the attached flow region at control points
VVORT		the velocity components induced by the free vortices at control points
VNOR	$\Sigma\sigma_{ij}d_j$	the normal velocity induced at the control point due to doublets
WI	w_{n_i}	the normal velocity due to external source at control points

A-38

Computer Name	Algebraic Name	Description
VELL		tangential velocity at the control points in chordwise direction induced by the doublets
VVLL		tangential velocity at the control points in chordwise direction induced by the free vortices
UZC		component of the free stream in the chordwise tangential direction at the control points
GRC	∇D	local gradient of the doublet distribution
MP		number of the control point
XP,YP,ZP	$\bar{x},\bar{y},\bar{z}$	the nondimensional coordinates of the control point
VCHORD	v_{t_c}	induced component of velocity in the chordwise tangential direction
VSPAN	v_{t_s}	induced component of the velocity in the spanwise tangential direction
CPK	$C_{P_{att}}$	the pressure coefficient at the box where the flow is attached
CPS	$C_{P_{sep}}$	the pressure coefficient on the box where flow is separated
ABOX		representative area of the box
GAMK	d_j	the doublet panel strength
CLPU		the lift coefficient due to upper surface pressures on attached region
CLSU		the lift coefficient due to upper surface pressures on the separated region

Computer Name	Algebraic Name	Description
CMXU, CMYU		moment coefficients around x and y axes due to pressures on the upper surface of the semi-wing
CLSAVE		lift coefficient due to pressures on both surfaces of the wing in the attached region
CLSTAL		lift coefficients due to pressures on both surfaces of the wing in the separated region
CMX, CMY		moment coefficients due to pressures on both the surfaces of the wing
CLTOT		total lift coefficient
CMXT, CMYT		total moment coefficients around x and y axes
XCOP, YCOP		center of pressure coordinates for pressures acting on the semi-wing

Vortex displacement information

Computer Name	Algebraic Name	Description
UU, VV, WW		the components of the velocity at control points on the vortex due to wing doublets, free stream, vortices themselves, and axial velocity in the core
VEX, VEY, VEZ		(x, y, z) coordinates of the control points on the vortex (old position)
VEDX, VEDY, VEDZ		(x, y, z) coordinates of the control points on the vortex (new position)
XER, YER, ZER		errors in the coordinates of the position on the vortex
CORER	r_{c_i}	core radius of the vortex at the control point on the vortex
GAMC, GAMV	Γ_c, Γ_v	the strength of the elements of the vortex

A-40

Computer Name	Algebraic Name	Description
UNET,VNET, WNET		the total velocity components at the control points on the vortex due to all sources
XERL,YERL,ZERL		total cumulative error squared for the given vortex

V. Suction peaks information

Computer Name	Algebraic Name	Description
XP,YP,ZP		coordinates of the points at which the incremental suction pressures are calculated
XP1,YP1,ZP1		nondimensional $\bar{x}$, $\bar{y}$, $\bar{z}$ coordinates of the above points
CPTS	ΔC_{p_v}	incremental suction pressure coefficient
CPAT	$C_{p_{at}}, C_{p_{sep}}$	wing pressure coefficient (interpolated value)
CPTOT	$C_{p_{tot}}$	total C_p value

NOTE:

Appropriate $f(\bar{x})$ and $\dfrac{df(\bar{x})}{d\bar{x}}$ have to be substituted in subroutines ZCOR and ZSLP to match the airfoil of the wing for which the calculations are being made.

Presently the $f(\bar{x})$ and $\dfrac{df(\bar{x})}{d\bar{x}}$ correspond to symmetric four digit NACA airfoils.

$f(\bar{x})$ is given by

$$f(\bar{x}) = 10 \, (.2969\sqrt{\bar{x}} - .126\bar{x} - .3516\bar{x}^2 + .2843\bar{x}^3 - .1015\bar{x}^4)$$

$$\frac{df(\bar{x})}{d\bar{x}} = 10 \, (.14845/\sqrt{\bar{x}} - 126 - .7032\bar{x} + .8529\bar{x}^2 - .406\bar{x}^3)$$

DISTRIBUTION LIST

Office of Naval Research
800 N. Quincy St.
Arlington, VA   22217
  ONR 211   4
  ONR 438   1

Office of Naval Research Branch
  Office
1030 E. Green St.
Pasadena, CA   91106   1

Office of Naval Research Branch
  Office
Bldg. 114 Section D
866 Summer St.
Boston, MA   02210   1

Office of Naval Research Branch
  Office
536 South Clark St.
Chicago, IL   60605   1

Naval Research Laboratory
Washington, DC   20375
  Code 2627   1
  Code 2629   1

Defense Documentation Center
Bldg. 5 Cameron Station
Alexandria, VA   22314   12

David Taylor Naval Ship Research and
  Development Center
Bethesda, MD   20084
  Main Library, Code 522.1   1
  Code 522.3 (Aero Library) 1
  Code 16 (Dr. H. Chaplin)   1
  Code 1660 (Mr. J. Nichols) 1

Naval Air Systems Command
Washington, DC   20361
  AIR 320D (Mr. D. Kirkpatrick) 1
  AIR 5301 (Mr. L. Trobaugh)   1

Naval Air Development Center
Warminster, PA   18974
  Code 6053 (Mr. C. Mazza)   1

U. S. Naval Postgraduate School
Monterey, CA   93940
  Dept. of Aeronautics (Code 57) 1
  Library   1

Superintendent
U. S. Naval Academy
Annapolis, MD   21402   1

Air Force Office of Scientific Research
Bolling AFB, DC   20332
  Code NA (Dr. J. Wilson)   1

Air Force Flight Dynamics Laboratory
Wright Patterson AFB, OH   45433
  AFFDL/FXM (Mr. R. Jeffries) 1
  AFFDL/FGC (Mr. J. Olsen)   1

Defense Advanced Research Projects Agency
1400 Wilson Boulevard
Arlington, VA   22209
  Mr. R. Moore   1

NASA Langley Research Center
Hampton, VA   23365
  MS 286 (Mr. R. Margasson) 1
  MS 287 (Dr. J. F. Campbell) 1
  MS 413 (Mr. W. Sawyer)   1
  MS 406 (Mr. C. Jackson)   1

NASA Ames Research Center
Moffett Field, CA   94035
  MS 227-8 (Mr. G. Malcolm) 1
  MS 227-2 (Mr. D. Bencze)   1

Vought Corporation
Advanced Technology Center, Inc.
P. O. Box 6144
Dallas, TX   75222
  Dr. G. Hough   1

Lockheed Missiles & Space Co., Inc.
Huntsville Research & Engineering Center
P. O. Box 1103
Huntsville, AL   35807
  Mr. A. Zalay   1